UNIVERSITY OF CALIFORNIA
Los Angeles

Single-Shot Characterization of High Transformer Ratio Wakefields in Nonlinear Plasma Acceleration

A dissertation submitted in partial satisfaction
of the requirements for the degree
Doctor of Philosophy in Physics

by

Ryan Joshua Roussel

2019

ABSTRACT OF THE DISSERTATION

Single-Shot Characterization of High Transformer Ratio Wakefields in Nonlinear Plasma Acceleration

by

Ryan Joshua Roussel
Doctor of Philosophy in Physics
University of California, Los Angeles, 2019
Professor James Rosenzweig, Chair

We demonstrate the first single shot measurement of a multi-period, loaded PWFA wakefield, used to conduct measurements of the transformer ratio (TR), the ratio between the maximum accelerating and decelerating fields in a collinear wakefield accelerator, that far exceed previous measurements. The emittance exchange beamline at the Argonne Wakefield Accelerator was used to create a variable longitudinal drive profile with a long witness to sample multiple wakefield periods. A TR exceeding the limit of 2 for longitudinally asymmetric beams was observed for a linear ramp and wakefield flattening was observed for a beam with a parabolic head. These effects are important for efficient energy transfer from drive to witness beam, and for lengthening the interaction length of the process. Furthermore, by adjusting plasma density parameters, multi-period plasma wakefields were observed transitioning from linear to nonlinear regimes leading to experimental verification of theoretical wakefield properties. 3D Particle in cell simulations are used throughout to support the experimental findings.

The dissertation of Ryan Joshua Roussel is approved.

David Saltzberg

Seth Putterman

Pietro Musumeci

James Rosenzweig, Committee Chair

University of California, Los Angeles

2019

To my parents and to Paige

TABLE OF CONTENTS

LIST OF FIGURES

LIST OF TABLES

ACKNOWLEDGMENTS

During my time at PBPL my scientific work was aided by a number of people. I would like to thank the members of PBPL for providing a helpful and inspirational workplace. This includes my fellow PBPL graduate students David Cesar, Nathan Majernick, Nick Sudar, Emma Snively, and Claudio Emma who I look forward to working with throughout my career. I would also like to thank Yusuke Saki, Atsushi Fukasawa, and Oliver Williams as both direct mentors and good friends throughout.

Outside of UCLA I would like to thank a few individuals in particular. Ariel Nause was a postdoc at UCLA and supervised my first projects at UCLA. Under his leadership I learned how to become a better scientist and deal with the ups and downs of doing experimental work. I also would like to thank Gwanghui Ha, who supervised the planning and running of my experiment with Jimin Seok at Argonne. Eric Wisniewski, Scott Doran, Wanming Liu and Charles Whiteford were integral to construction of the plasma experimental beamline. Nicole Nevau, who helped me get started with simulations, was also one of my closest friends at Argonne. I also want to thank Manoel Conde and John Power for their leadership and supervision at Argonne and Jihang Shao, Stas Baturin for their friendship and support.

During the initial stages of recommissioning the UCLA plasma source, I had a number of UCLA students work with me. This includes Walter Lynn, Gerard Lawler, Kunal Sanwalka, Claire Hansel, and River Robles. They all were great students and I see that the skills they have gained are already being used in their work today.

In particular I would like to thank Gerard Andonian for his critical role in overseeing my thesis experiment and my time here at UCLA. He helped me at every turn and provided helpful advice and reassurance when I needed it most. His wisdom helped me navigate the analysis and presentation of my experiment results, as well as, trying to find my future path.

Finally, I of course would like to thank my advisor James Rosenzweig. During my time at UCLA he has been extremely helpful in understanding the topics of study we developed together and growing into a mature scientist. Also, prior to arriving at UCLA I had never traveled outside of the US East Coast, due to the opportunities afforded to me by Jamie, I was able to travel and work in a number of different places in the world which helped me grow into a better person. Furthermore, Jaime's experience of working in the accelerator

field was incredibly helpful in determining what I want to study now and in the future.

VITA

2014–2019	Graduate student researcher, Particle Beam Physics Laboratory, UCLA
2018–2019	DOE Office of Science graduate student researcher, Argonne National Laboratory, Illinois
2014	M. S. (Physics), UCLA, Los Angeles, California
2013–2014	Teaching Assistant, 4BL Electricity and Magnetisim Lab, UCLA
2013	SULI Student Researcher, SLAC National Laboratory
2013	B. S. (Physics) Rensselaer Polytechnic Institute, *Summa Cum Laude*, New York
2012	REU student researcher, Thomas Jefferson National Laboratory

PUBLICATIONS

R. Roussel, et. al., "Single-Shot Characterization of High Transformer Ratio Wakefields in Nonlinear Plasma Acceleration" Submitted to PRL

T. Paschen, R. Roussel, C. Heide, J. Rosenzweig, P. Hommelhoff, "Strong-field photoemission from a nanometric blade structure", Submitted to PRX

Roussel, Ryan, et al. "Externally Heated Hollow Cathode Arc Plasma Source for Experiments in Plasma Wakefield Acceleration." Instruments 3.3 (2019): 48.

Roussel, Ryan, et al. "Transformer Ratio Measurements from Ramped Beams in the Plasma Blowout Regime using Emittance Exchange." 10th Int. Particle Accelerator Conf.(IPAC'19), Melbourne, Australia, 19-24 May 2019. JACOW Publishing, Geneva, Switzerland, 2019.

Roussel, Ryan, et al. “Measurement of transformer ratio from ramped beams in the blowout regime.” Nuclear Instruments and Methods in Physics Research Section A: Accelerators, Spectrometers, Detectors and Associated Equipment 909 (2018): 130-133.

Roussel, R., and J. Rosenzweig. “Space radiation simulation using blowout plasma wakes at the SAMURAI Lab.” Nuclear Instruments and Methods in Physics Research Section A: Accelerators, Spectrometers, Detectors and Associated Equipment 865 (2017): 71-74.

CHAPTER 1

Introduction

Discovery in physics over the past century has gone hand in hand with the development of particle accelerators. From the first cyclotron accelerator in the 1930's [4] to current state of the art facilities [5], accelerating electrons and ions to relativistic energies have allowed the discovery of fundamental physics. The largest accelerator operating today, the Large Hadron Collider, and other similar machines have led to our understanding of the fundamental particles and forces in the universe [6]. This follows a historical trend of fundamental physics discoveries due to accelerators, including discovery of the electron [7], atomic nucleus [8] and high energy x-rays [9].

Today the use of accelerators exceeds the confines of physics research. Recently they have served as tools for studying biology, material science and chemistry. Radiation from accelerated electrons, either in a synchrotron or free electron laser is used to map out the structure of complex biological proteins [10]. High energy, coherent x-rays can also be used to conduct pump-probe experiments in order to measure quantum mechanical processes in materials [11]. Development of extremely short x-ray pulse lengths approaching 100s of attoseconds [12] allows time dependent imaging of atomic and chemical processes [13]. Furthermore, accelerators are starting to be widely used in industrial and medical applications [14].

Applications both inside and outside physics continuously push for improvement in particle accelerator technology. For high energy physics experiments, particle physicists are interested in center-of-mass electron energies approaching 500 GeV [15]. Producing beams with energies of this magnitude is not possible in circular machines due to energy losses via synchrotron radiation [16], so linear accelerators must be used, resulting in extremely long machines ~ 31 km [17]. This becomes a problem when we consider the costs associated with construction and operation of the equipment necessary. For example, the design report for the International Linear Collider cites an estimated cost of about $8 billion USD [17], a figure

which has up till now, has prevented any country from committing to hosting the facility [18]. On the other hand, small scale medical and industrial applications need beam energies in the 100 - 250 MeV range, but cannot afford to accommodate large $\sim$ 50 m conventional accelerators. Furthermore, widespread availability of modest energy electron machines at the university scale would allow small research groups to conduct experiments that are comparable to those done at national laboratory facilities today. Advanced accelerating techniques are needed to make accelerators at both these energy scales practical.

One strategy towards reducing cost is increasing the accelerating gradient of accelerators. This would reduce the overall length of the accelerator for a given final energy target, which in turn is expected to reduce construction and infrastructure costs. As of now, superconducting radio-frequency cavities constructed out of niobium represent state of the art accelerating structures. However, experimental demonstration of these cavities is limited to peak electric fields on the order of 31 MeV/m [19], thus requiring $\sim$32 km of accelerator to reach 1 TeV. The goal for developing the next generation of accelerator technology is reaching 10's of GeV/m in accelerating gradient, which represents several orders of magnitude in improvement.

Advanced accelerator concepts propose to meet this goal through the use of new material structures, often driven by collinear wakefield acceleration. In conventional structures, peak accelerating field scales inversely with the supported electromagnetic field wavelength. Attempts to shorten traveling wave structures has produced X-band accelerating cavities with an operating frequency of 9.3 GHz [20]. At these frequencies, the question of high power electromagnetic sources at these frequencies becomes an issue. Electron beam drivers were proposed as a method of exciting these devices using the beam's wakefield, as the beam decelerates in the structure [21]. An electron beam can potentially store a large amount of energy once accelerated, and this energy can be efficiently deposited into the structure as wakefields. In order to be used for acceleration, two bunches of electrons travel collinearly through a structure which extracts energy from the first bunch (known as the drive) to feed an electromagnetic wakefield that accelerates a second bunch (known as the witness[1]).

The next limitation for reaching higher accelerating fields is the breakdown rate, which refers to arcing behavior inside an accelerating cavity. As field amplitude increases, electrons

[1]Also known as the "main"beam in the case of multistage wakefield accelerator configurations

can jump from point to point on the inner cavity surface. This presents a hard limit for peak electric field in the cavity because it removes all the stored energy in the cavity, thus preventing particle acceleration. Superconducting (SRF) cavities attempt to surpass breakdown limits of copper structures at room temperature by using superconducting materials (niobium) at 4 Kelvin [22]. Regardless, the field amplitude is still limited by surface material properties [23].

Recent research has attempted to push material breakdown boundaries via the use of dielectrics as supposed to metals. Dielectrics can support much higher electric fields than metals due to their material properties [24]. Experimentally, dielectric-lined cylindrical tubes have been shown to withstand 10 GV/m electric fields [25]. Furthermore, these devices have already been shown to provide significant accelerating gradients in the context of a dielectric waveguide collinear wakefield experiment [26].

To reach even higher fields we can use gases that are already ionized, plasmas, which do not suffer from breakdown issues as they are already in an ionized state. The so called plasma wakefield accelerator (PWFA) uses a highly charged electron beam to repel plasma electrons in a localized area around the beam. Due to their relatively large mass, ($m_i/m_e \approx 2000$) ions are left behind, creating a region of excess positive charge which provides a restorative force for repelled electrons causing them to return on axis in an electron density "wave". This scheme has the potential of reaching TeV/m accelerating gradients with ultrashort beams which are currently produced today [27]. Experimental wakefields have been observed to reach upwards of 52 GV/m, effectively doubling the energy of electrons from 3-km of SLAC accelerator in just a meter [28].

Unfortunately, full scale realization of a PWFA beam-based accelerator is far from trivial. A number of problems unique to beam-plasma interactions, must be solved before beams from plasma wakefield accelerators can reach parameters necessary for relevant applications. We conduct a brief survey of them here. 1) Stable transverse beam transport through plasma: Due to focusing forces that we will discuss in Ch. 2 the beam undergoes stable betatron oscillations in a uniform focusing field if it is matched to the corresponding plasma density. Transverse emittance preservation of the drive beam relies on proper design of plasma density profiles leading into and out of the plasma region [29]. 2) Efficient beam capture and acceleration: Plasma accelerating "structure"geometries are poorly controlled when com-

pared to static metallic or dielectric structures. The plasma response constantly evolves as the beam travels through the plasma which makes efficient capture and subsequent acceleration of electrons in the wake only possible if all beam-plasma dynamics are understood and properly controlled. This severely limits the quality of transverse and longitudinal properties of the accelerated beam [30]. 3) Optimal parameters for multi-stage operation and the development of technology to meet those parameters [31]. 4) Limitations in total energy gain: If the wake is excited by draining drive beam energy, there will be a point at which the drive is completely depleted of energy and the wakefield collapses. This maximum energy is further limited by relativistic considerations. Once drive particles lose enough energy, they become sub-relativistic and will slip out of phase with the interaction which travels with a group velocity at nearly c.

To understand the relevance of these limitations, we can consider a simple back of the envelope calculation. Observing that PWFA schemes can easily reach GV/m gradients we can aim to create a 1 GeV electron accelerator in the soon to be built SAMURAI Lab at UCLA[2]. The bunker design for this lab has 18 m of space for a beamline and accounting for the fact that 1 GeV is 16x the design energy of 60 MeV lets say we have 15 m to work with due to the extra radiation shielding required. We want accelerated particles to reach 1 GeV in a 1 meter of plasma, resulting in a desired accelerating field of 1 GeV/m. To determine how this will decelerate our drive beam we use what is known as the transformer ratio (TR) which is defined as

$$\mathcal{R} = \left| \frac{W_+}{W_-} \right| \tag{1.1}$$

where W_+ is the maximum accelerating field experienced by the witness and W_- is the maximum decelerating field in the drive. We will see in subsequent chapters that $\mathcal{R}$ is limited to less than 2 for symmetric drive bunches. If we assume conditions for maximum TR are reached, the decelerating field in the drive will be 500 MV/m. Over one meter of plasma the drive will lose energy equal to 500 MeV.

This result is quite sobering, as it tells us that to sustain the wakefield interaction over the entire plasma column we need a drive bunch with energy of at least $\sim$ 525 MeV for it to remain relativistic. For a conventional accelerator to reach the required energy, 22 m of copper S-band cavity operating at 25 MV/m would be required, which is too long for our

[2] soon$^{\text{TM}}$

bunker. However, if we were able to increase the transformer ratio of our plasma accelerator, the required drive beam energy could be significantly reduced and would shrink the required conventional accelerator in kind.

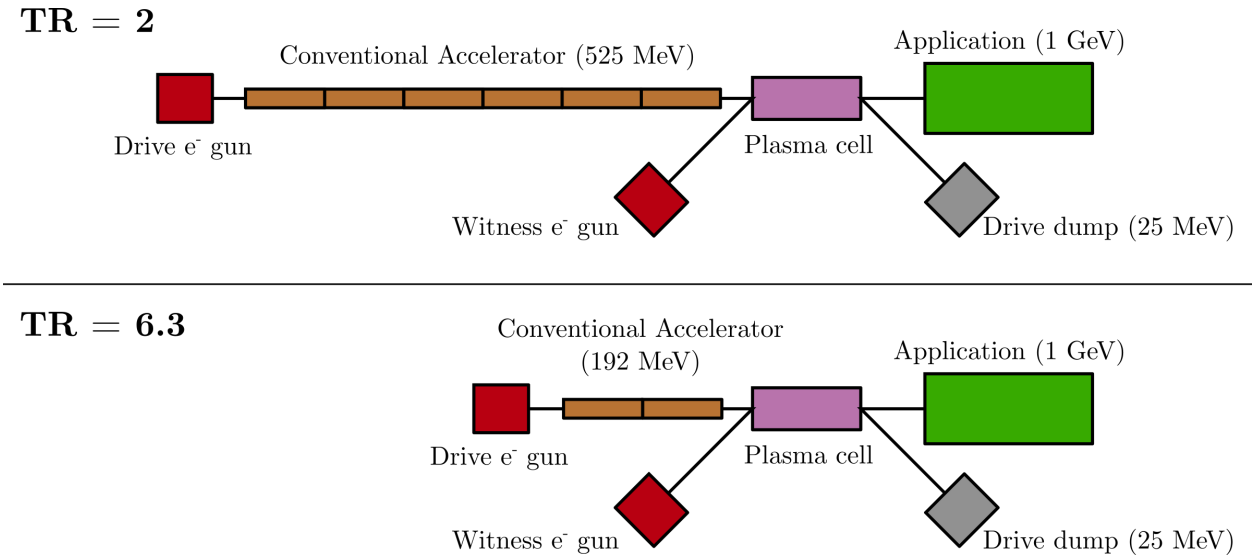

Figure 1.1: Cartoon energy comparison between PWFA accelerator designs where the drive beam excites a wakefield with TR is 2 (top) or 6.3 (bottom).

For example, it has been demonstrated that linearly ramped current distributions can excite wakefields that surpass a TR of 2. Analytical calculations of wakefields in the linear plasma regime has shown that linearly ramped bunches stretching over two plasma wavelengths produces a TR of $2\pi \approx 6.3$ [32]. If we were able to use ramped beams in our accelerator, the drive wakefield decreases to 167 MV/m which results in a total energy loss of 167 MeV. For the same copper RF structure as used before, and a drive energy of 192 MeV, our conventional accelerator shrinks to a reasonable 7.5 m, as seen in Figure 1.1.

Our calculation ignores a large number of physical and practical issues. Generation and transportation of beams with the correct brightness to the plasma source while properly shaping the beam is a major hurdle that needs to be overcome. The beams must be focused properly to successfully excite the plasma wake while remaining stable over one meter. Efficient bunch shaping techniques also serve as a limitation of our scheme. Regardless, this calculation reveals the benefits of increasing TR to the design and use of wakefield accelerators.

Based on this realization, significant work has been done towards engineering beams to

have tailored current profiles. Work done at UCLA's Neptune accelerator used a double bend dogleg beamline with higher order transverse corrections to demonstrate generation of linearly ramped current profiles [33]. Another method at BNL demonstrated shaping through the use of self-wakefields in a dielectric structure and a magnetic chicane [34].

More recently, a laser pulse shaping technique was used at PITZ in Germany to create a temporal ramp in the laser intensity profile [35]. This was done by separating a laser pulse into 12 smaller sub-pulses using a Solc fan filter. When recombined, these pulses are equally spaced in the temporal axis. Intensity of each pulse can be controlled independently, thus allowing the formation of nearly arbitrary temporal intensity distributions. In a photocathode electron gun this translates directly to a beam current distribution when the laser is incident on the cathode. Unfortunately, for high charge beams (> 1 nC) space charge forces at the gun where beam energy is low [36] smooths out any sharp features in our current profile, which we will show, leads to a reduction in TR.

Finally, longitudinal beam shaping can be done using an emittance exchange beamline (EEX). This beamline consists of two dogleg sections, connected by a transverse deflecting cavity [37]. The beamline exchanges the horizontal and longitudinal beam phase space, which in turn maps the horizontal projection of the beam distribution into the longitudinal current profile. The EEX method allows flexibility in generating variable beam profiles through the use of a transverse mask. Masks are relatively easy to fabricate into precise, arbitrary shapes and can be changed out *in situ*, allowing rapid testing of various profiles. Furthermore, EEX allows the creation of long, low charge witness bunches which can sample the wakefield over several periods in a single shot [38]. In previous measurements the witness was short relative to the wakefield wavelength and had to be temporally scanned to sample the entire wakefield [39], which introduces errors in the measurement due to beam jitter.

Thanks to the ramped beam generation techniques described above, measurement of the transformer ratio from shaped beams has been possible. The emittance exchange technique has been used to study ramped beams in planar dielectric structures [40]. Here Gao et. al. were able to measure a transformer ratio of ≈ 5 for a ramped beam over two wakefield periods, close to the theoretical limit of $\mathcal{R} = N\pi = 2\pi$. In the case of plasmas, laser shaping at the cathode was used to generate beams which were then injected into a plasma cell [41]. Here they were able to observe a maximum transformer ratio of 4.6, which is a reasonable

for a ramped beam over 1.5 plasma periods. However, their measurement was limited to a low charge drive beam (< 0.5 nC) and a low plasma density (2×10^{13} cm^{-3}). They were also limited to using a short witness beam which they could not scan to measure the entire wakefield.

In this experiment we aim to improve on their measurement by using the technique developed by Gao et. al. to sample the entire wakefield response, while increasing the drive charge and the plasma density to achieve a larger wakefield. Our goals for this experiment are as follows: (1) Measure the transformer ratio from a linearly ramped beam shaped via EEX, interacting with a matched plasma density such that the beam length is two wakefield periods long. (2) Characterize the a full, single shot, multi-period wakefield from a plasma wakefield accelerator. (3) Measure the effect of perturbations on the drive beam shape on the wakefield response. (4) Measure the effect of changing from a linear to non-linear regime by scanning the plasma density.

During our experiment we were able to use beams shaped via the EEX technique in a plasma source to demonstrate a maximum transformer ratio of 7.8, which is the highest transformer ratio ever measured for a wakefield structure. We found that a linearly ramped bunch experiences a linear, single mode, decelerating wakefield but excites a stronger non-linear accelerating field akin to the plasma blowout regime. We also introduce a novel beam current reconstruction technique based solely on the measured wakefield response. Analytically, the transformer ratio is maximized when the wakefield is uniformly decelerating in the drive. We demonstrate this effect through the creation of a quadratic beam head modification to the linear ramp profile. Finally, we measure the effect of plasma density on the multi-period wakefield structure.

1.1 Experiment Overview

The Argonne Wakefield Accelerator (AWA) facility at Argonne National Laboratory serves as an ideal place to study wakefield acceleration and more recently has become the perfect place to conduct transformer ratio studies. The main AWA beamline can produce extremely high charge bunches in excess of 100 nC, through the use of a cesium-telluride cathode and a 248 nm, 15 mJ, 6-10 ps laser pulse at energies up to 75 MeV [42]. The laser spot is homogenized

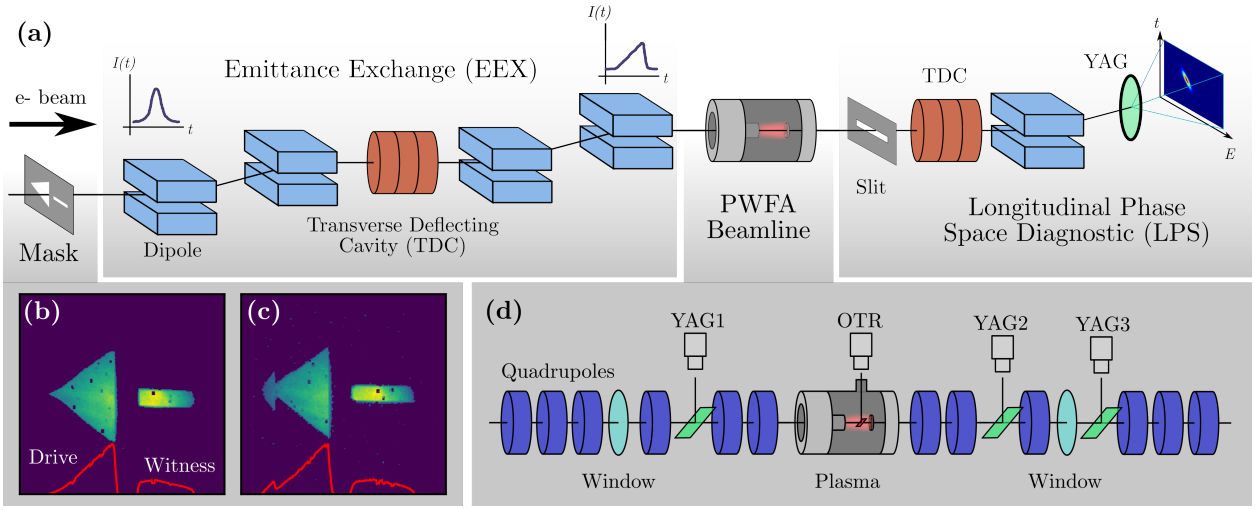

Figure 1.2: (a) Experimental beamline overview for the high TR PWFA experiment at AWA. (b) Transverse mask used to generate a ramped current profile and long witness after EEX. (c) Mask used to generate ramp with triangular head perturbation and long witness. (d) Detail view of plasma beamline.

using a micro-lens array which creates a near-uniform transverse beam distribution [43].

An overview of this experiment at the AWA facility is seen in Fig. 1.2. The AWA facility drive beamline (not shown) is used to generate a 12 nC, 40 MeV electron beam to the experimental beamline shown here which contains 4 parts. One of two transverse masks (Fig. 1.2(b,c)) shapes the horizontal beam projection. Second, the emittance exchange technique is applied to the beam to transform the horizontal profile into a longitudinal current distribution. Third (Fig. 1.2(d)), the beam is transported to the plasma cell. Finally, the beam is then transported to a longitudinal phase space diagnostic (LPS) which measures the longitudinal phase space of the beam with and without plasma interaction.

1.2 Dissertation Overview

This dissertation consists of chapters that explore each aspect of the experiment. We begin with a discussion of general wakefield theorems and their application to plasma based wakefields in Chapter 2. In Chapter 3 we discuss longitudinal beam shaping using emittance exchange. Next, in Chapter 4 we investigate the design and operation principals of the hollow cathode arc plasma source. Afterwards, we will look at the plasma beamline

design which transports beams into and out of the plasma in Chapter 5. In Chapter 6 we will discuss the analysis of wakefield measurements and the calculation of transformer ratio from the measurements. Finally we conclude with a discussion of the results and examine possible routes for future experimentation.

CHAPTER 2

High Transformer Ratio and Plasma Wakefields

Collinear wakefield acceleration refers to the exchange of beam energy between two charged particle bunches through the use of a wakefield-inducing structure or medium. This process of energy transfer from one electron bunch to another is not new, as this technique is used to power todays conventional accelerators. The goal of an accelerator is to produce a high quality electron beam with high center of mass energy and high brightness. A quality beam is produced using a photoinjector and is accelerated by radio-frequency waves supported by tuned accelerating structures. In conventional accelerators, electromagnetic power comes from klystrons, where low quality, high charge beams are accelerated via a kilovolt pulse and then their energy is extracted through deceleration which produces RF waves that are then transported to accelerating cavities [44]. A number of these accelerating stages are used to accelerate the main beam to much higher energies in the MeV-GeV range.

The use of collinear wakefield acceleration is similar in this regard. A beam called the drive is accelerated to a given energy and is then sent into, either a metallic, dielectric structure or a medium such as plasma, where it deposits its energy into a wakefield. A second beam, called the witness, is then injected collinearly behind the drive, to capture some of the available energy.

In this chapter, we conduct a discussion of the wakefields generated by electron beams in plasmas. We will begin with a study of fundamental wakefield concepts including the effect of linearly ramped beams (and perturbations to the linear profile) on transformer ratio. We will then discuss these ideas in the context of linear plasma electron response due to low charge beams. Afterwards we will expand our results from the linear case to the nonlinear/blowout regimes. Finally, we conclude with an examination of beam dynamics in simulations using the particle in cell (PIC) Warp.

2.1 Transformer Ratio Limits from Linear Wakefield Theory

2.1.1 Wakefield Acceleration for Delta Function Bunches

We begin by considering two relativistic delta function like bunches that enter an arbitrary structure which supports a wakefield $W(\xi) = eE_z(\xi)$ in a moving frame with the bunch. In this frame the longitudinal coordinate becomes $\xi = z - ct$. We assume that both bunches travel collinearity on the z axis and are separated by a distance d which does not change throughout the interaction. This condition is easy to satisfy, as both bunches are relativistic, they travel at the speed of light c regardless of small deviations in their central momentum. We also assume the quasi-static approximation, where the wakefield does not change throughout the interaction.

A cartoon of this scenario is seen in Figure 2.1.

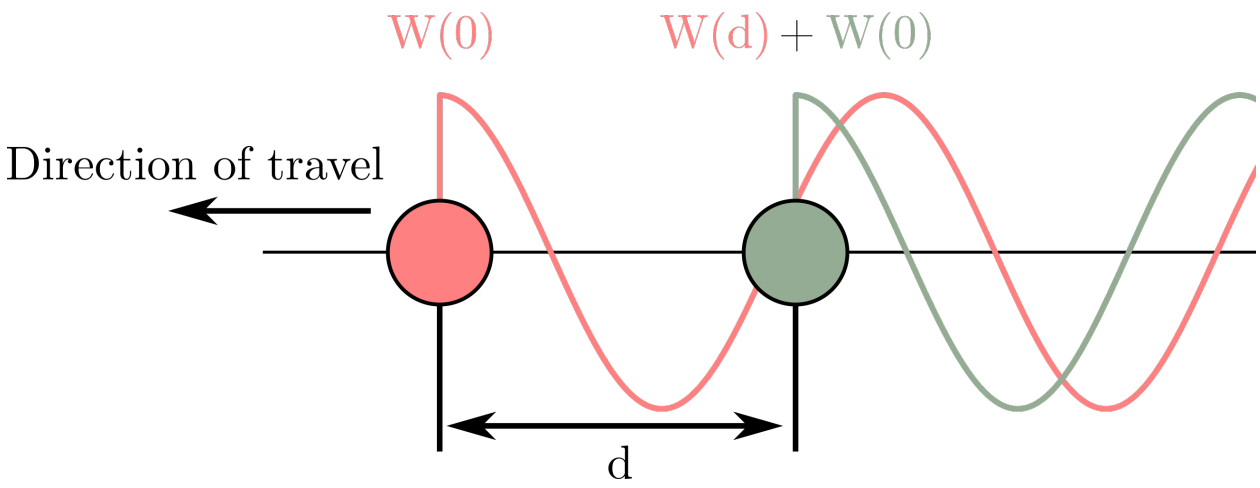

Figure 2.1: Cartoon of two delta function type beams separated by a fixed distance with their corresponding wakefields.

We can calculate the energy loss of the first bunch due to its self-created wakefield as

$$\frac{d(N_1 E_1)}{dz} = -N_1^2 e^2 W(0) \tag{2.1}$$

where N_1 is the number of particles in the first bunch, E_1 is the individual particle energy and e is the electron charge. Our witness bunch at a fixed distance behind the drive d it will be affected by both its own self-wake and the drive wakefield

$$\frac{d(N_2 E_2)}{dz} = -N_2^2 e^2 W(0) - N_1 N_2 e^2 W(d) \tag{2.2}$$

where N_2, E_2 are the number of particles and energy of the witness bunch.

Due to energy conservation, the total change in energy of the bunches added together must satisfy

$$\frac{dE}{dz} = \frac{d(N_1 E_1)}{dz} + \frac{d(N_2 E_2)}{dz} \leq 0. \tag{2.3}$$

It is instructive to consider a case where the witness bunch absorbs all of the energy lost by the drive. For this to be the case we assume that the bunches have equal charge $N_1 = N_2$ and we choose a witness delay of d^* such that there is no net field (and thus no stored energy) behind the witness. From this we get the relation

$$\frac{dE_1}{dz} = -\frac{dE_2}{dz}. \tag{2.4}$$

Plugging in our equations relating the wakefield to energy loss we get

$$W(0) = W(d^*) - W(0) \tag{2.5}$$

which gives the following relationship between the wakefields

$$W(0) = -\frac{1}{2} W(d^*). \tag{2.6}$$

We see that the witness bunch sees a decelerating wakefield that is half the accelerating field experienced by the drive. While this may seem counterintuitive, it is a direct result from conservation of energy and the fact that no electromagnetic fields exist behind the witness. In this case we consider the drive wake to be completely "loaded".

If the witness bunch is not located at a position d^* or has a different charge, such that the net wakefield after the witness has non-zero amplitude, some energy from the drive is not absorbed by the witness. This is where the inequality seen in Eqn. 2.3 comes into play. For an arbitrary case where the drive and witness have different charges $N_1 \neq N_2$ and the separation is not determined, energy conservation dictates that

$$-(N_1^2 + N_2^2) W(0) - N_1 N_2 W(d) \leq 0. \tag{2.7}$$

We can define a charge ratio between the drive and witness bunches $\alpha \equiv N_1/N_2$ where $\alpha > 0$ as $N_1, N_2 > 0$. Substituting this into the previous equation results in

$$-W(d) \leq \frac{\alpha^2 + 1}{\alpha} W(0). \tag{2.8}$$

The term $(\alpha^2+1)/\alpha$ has a global minimum of two when $N_1 = N_2$, resulting in

$$-W(d) \leq 2W(0) \tag{2.9}$$

which is consistent with our earlier result.

In this case the energy gain per unit length of the witness bunch is limited to

$$\frac{dE_2}{dz} \leq (2N_1 - N_2)e^2 W(0) \tag{2.10}$$

The drive beam will be decelerated by its wakefield resulting in an energy difference ΔE_1. This will occur over an interaction length L calculated to be

$$L = \frac{\Delta E_1}{N_1 e^2 W(0)}. \tag{2.11}$$

The energy gain of the witness is thus limited to

$$\Delta E_2 = \int_0^L \frac{dE_2}{dz} dz \leq \Delta E_1 \left(2 - \frac{N_2}{N_1}\right). \tag{2.12}$$

It is clear that maximizing the energy gain of the witness ΔE_2 is achieved by minimizing the ratio of witness to drive beam particles. If we follow this logic further by setting $N_2/N_1 \to 0$ we see that the maximum gain in per particle energy in the witness is limited to two times the drive particle energy. This ratio $\Delta E_2/\Delta E_1$ is often referred to as the wakefield transformer ratio. This does not bode well for the usefulness of collinear wakefield schemes if we consider the practical difficulties of preparing both a quality drive and witness bunch, only to get a factor of two in energy increase.

We can also consider the overall efficiency of the interaction η, or the total amount of drive energy that gets transferred to the witness given by

$$\eta \equiv \frac{N_2 \Delta E_2}{N_1 \Delta E_1} \leq \frac{N_2}{N_1}\left(2 - \frac{N_2}{N_1}\right). \tag{2.13}$$

From this we see that the maximum energy transfer efficiency is achieved when $N_2/N_1 = 1$.[1] This stands at odds with the optimization of our transformer ratio which requires $N_2/N_1 \to 0$. Conceptually, if we choose to maximize the transformer ratio by having a small number of witness particles relative to the drive then only a small portion of the energy lost by the

[1]Energy transfer efficiency is of course limited by energy losses to the wakefield structure and in the case of multiple wakefield modes.

drive will actually be translated into useful witness acceleration. When each bunch has the same charge, the witness completely absorbs energy lost by the drive and no wakefield is present after the witness. In between these two limits, the witness bunch receives a portion of the drive energy lost, which reduces the wakefield amplitude afterwards and is referred to as "loading" the wakefield.

2.1.2 Wakefield Acceleration for Finite Sized Bunches

Our results from the previous section assume that both the drive and witness bunches are essentially zero length, ie. delta functions $\delta(\xi)$. We will now consider bunches of finite, arbitrary shape and show that the inclusion of properly tailored drive profiles can exceed the aforementioned limit $\Delta E_2/\Delta E_1 < 2$. We write the wakefield response due to a delta function driver from Bane et. al. [21] $\delta(\xi')$ as

$$W(\xi) = \begin{cases} W_0 \cos(k(\xi' - \xi)) & \xi < \xi' \\ W_0/2 & \xi = \xi' \\ 0 & \xi > \xi' \end{cases} \tag{2.14}$$

where W_0, k are the drive particle charge, wakefield coupling coefficient, and characteristic wavenumber of the system respectively. We can generalize the wakefield response after the bunch for an arbitrary drive current profile $\lambda(\xi)$ with a convolution integral

$$W(\xi) = W_0 \int_{\xi}^{\infty} \lambda(\xi') \cos(k(\xi' - \xi)) d\xi'. \tag{2.15}$$

We need to describe a relationship similar to Eqn. 2.12 to account for nonuniform acceleration of the witness and deceleration of the drive. We define the transformer ratio as

$$\mathcal{R} = \frac{|W_m^+|}{|W_m^-|} \tag{2.16}$$

essentially saying that the transformer ratio (TR) is the ratio of the maximum accelerating field (W_m^+) to the maximum decelerating field experienced in the drive (W_m^-). If we have a short beam as before $\lambda(\xi) = \delta(\xi)$ the wakefield has the form of

$$W(\xi) = \begin{cases} W_0 \cos(k\xi) & \xi > 0 \\ W_0/2 & \xi = 0 \\ 0 & \xi < 0 \end{cases} \tag{2.17}$$

and we calculate the transformer ratio $\mathcal{R} = 2$ which matches our earlier analysis from Eqn. 2.12.

We now generalize the transformer ratio to any symmetric current profile, assuming that the profile is centered at zero such that $\lambda(-\xi) = \lambda(\xi)$ and whose full width extends in the range $[-Z, Z]$. We calculate wakefields inside the bunch ($\xi < Z$) to be

$$W^-(\xi) = W_0\Big[-\cos(k\xi)\int_\xi^Z \lambda(\xi')\cos(k\xi')d\xi' - \sin(k\xi)\int_\xi^Z \lambda(\xi')\sin(k\xi')d\xi'\Big] \tag{2.18}$$

and outside the bunch ($\xi > Z$) to be

$$W^+(\xi) = W_0\Big[-\cos(k\xi)\int_{-Z}^Z \lambda(\xi')\cos(k\xi')d\xi' - \sin(k\xi)\int_{-Z}^Z \lambda(\xi')\sin(k\xi')d\xi'\Big]. \tag{2.19}$$

If we take the bunch profile to be symmetric about zero then the second term in W^+ vanishes. This means that wakefield reaches a maximum value of

$$W_m^+ = W_0\int_{-Z}^Z \lambda(\xi')\cos(k\xi')d\xi'. \tag{2.20}$$

On the other hand if we calculate the wakefield at the center of the drive bunch $\xi = 0$ we get

$$W^-(0) = -W_0\int_0^Z \lambda(\xi')\cos(k\xi')d\xi' = -W_m^+/2. \tag{2.21}$$

If $W^-(0)$ happens to be the maximum decelerating field then $|W_m^2| = |W^-(0)|$ and the transformer ratio is 2. If it is not the maximum of the decelerating field then $|W_m^-| > |W^-(0)|$ and the transformer ratio is less than 2. This limit on the transformer ratio for symmetric beams is often referred to as the Fundamental Theory of Beam Loading [32].

This limit of $\mathcal{R} < 2$ can be surpassed by using a longitudinally asymmetric drive beam profile. A simple example would be a linear ramp profile where the beam current increases linearly from zero, $\lambda(\xi) = A\xi$ where A is a constant. We consider a ramp extends from $\xi = 0$ to a discrete number of wakefield wavelengths $\xi = 2\pi N/\lambda$ where N is an integer and is zero otherwise. The resulting wakefield inside the bunch and after the bunch is calculated via Eqn. 2.15 to be

$$W^-(\xi) = -W_0A(1 - \cos(k\xi)) \tag{2.22a}$$

$$W^+(\xi) = W_0A\pi N\sin(k\xi). \tag{2.22b}$$

The maximum transformer ratio is $\mathcal{R} = \pi N$ in this case can exceed 2 quite easily. Wakefields for the linearly ramped bunch geometry are plotted in Figure 2.2. We can see that

the transformer ratio of the linearly ramped bunch is proportional to the number of small wakefield undulations in the drive.

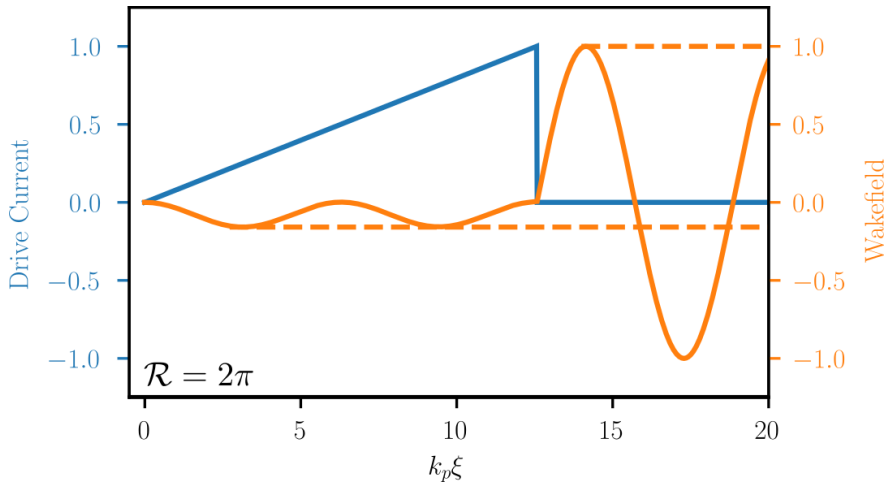

Figure 2.2: Plot showing simple triangle beam current distribution and resulting, single-mode wakefield.

It is also instructive to see how the peak accelerating field is dependent on the transformer ratio. If we assume a fixed amount of charge in our drive bunch $Q = eA(\pi N)^2/2$ then our accelerating wakefield has a peak value $W_m^+ \propto 1/\mathcal{R}$. This shows that when we shape the beam to get a higher transformer ratio, we do so by sacrificing peak accelerating field [45]. This becomes an important consideration during use of PWFA in applications.

2.2 Perturbations to the Linearly Ramped Profile

We started with a linearly ramped profile due to its simplicity. We will now investigate how perturbations to this profile affect the resulting transformer ratio.

2.2.1 Maximizing the Transformer Ratio in a Plasma

We have seen that the transformer ratio can be increased by using a ramped current profile, however we have yet to determine whether or not this shape gives us the maximum TR possible. To calculate what wakefield structure gives the best transformer ratio we use the energy conservation argument posed by T. Katsouleas [46].

A cartoon of this argument is seen in Figure 2.3. The drive wakefield causes the drive

beam (green) to lose kinetic energy at a rate proportional to the average wakefield inside the drive. Meanwhile, energy enters a box near the peak accelerating wakefield at a rate given by a time derivative of the total electric field energy stored in the box.

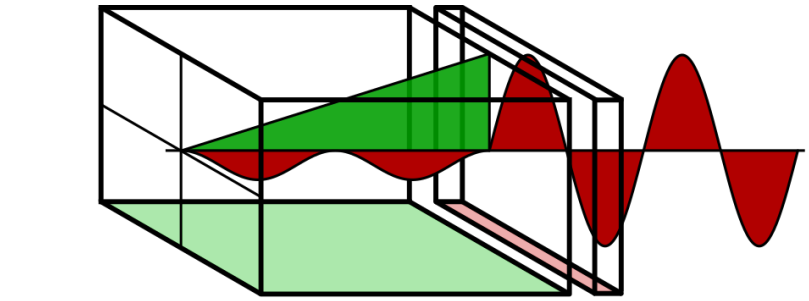

$$\frac{dE}{dt} = -\frac{d}{dt} N_b \gamma_b m c^2 = e N_b < W^- > = \frac{dE}{dt} = \frac{d}{dt} \frac{\epsilon_0 (W_m^+)^2}{2} Act$$

Figure 2.3: Conceptual energy conservation argument for derivation of maximum transformer ratio from wakefield flattening. Total kinetic energy loss of the drive beam (green) due to an average wakefield translates directly to energy flow into the wakefield box right behind the drive beam (red).

We calculate energy density of the wake directly behind the drive bunch to be $(\epsilon W_m^+)^2/2$ which is left in a volume $A \cdot ct$ where A is the cross-sectional area. Energy conservation yields

$$\frac{d}{dt} \frac{\epsilon (W_m^+)^2}{2} Act = N_b e < W^- > \tag{2.23}$$

where N_b is the number of particles in the drive and $< W_- >$ is the average decelerating field in the drive which will be some fraction α of the minimum wakefield $< W^- >= \alpha W_m^-$. Taking the time derivative and replacing our definition for transformer ratio we get

$$\mathcal{R} = \frac{8\pi N_b e \alpha}{W_m^+ c A} \tag{2.24}$$

Here we have recovered our earlier finding that the peak accelerating field is inversely proportional to the transformer ratio. We also see that $\mathcal{R}$ is proportional to α, which is maximized when $\alpha = 1$ or the minimum wakefield is equal to the average. For that to be the case, wakefield inside the drive must be a constant.

We can make the wakefield uniform for a majority of the drive beam with the correct choice of current profile. Bane et. al. calculated the distribution that maximized TR to be a linear ramp superimposed with a delta function head [32]. While this profile is practically

unrealizable, several shapes have been found to achieve a flattening of wakefields in the drive body [32, 47]. These shapes produce a near-uniform wakefield by modifying the head of a linear ramp as seen in Figure 2.4. We can see from Fig 2.4 that making modifications to

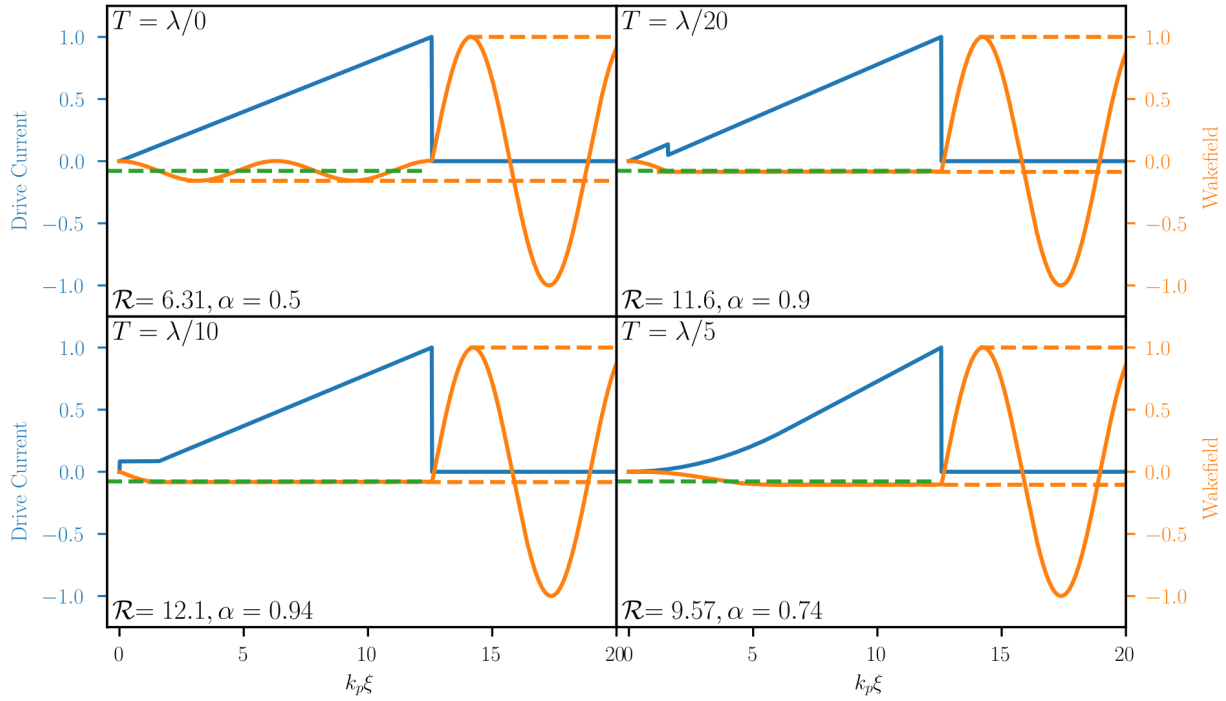

Figure 2.4: Uniform wakefields (orange) from variable head perturbations added to a ramped profile (blue). Orange dashed lines show maximum accelerating and decelerating fields. Green dashed shows $< W^- >$ inside the drive. (a) Ramped beam with no modifications. (b) Double-triangle profile perturbation with small triangle length $L = \lambda_p/4$. (c) Doorstep profile perturbation with doorstep length $L = \lambda_p/4$. (d) Parabolic head profile perturbation with a parabolic region length $L = \lambda_p$.

the head of the linearly ramped drive can increase the transformer ratio of the generated wakefield by up to a factor of two by making the decelerating field uniform. Depending on head modification, the average decelerating wake $< W^- >$ approaches W_m^- thus increasing the transformer ratio.

The profiles seen in Fig 2.4 b,c are historically derived profiles which gives the highest TR due to the fact that they produce a uniform field for a large majority of the drive bunch. The profile seen in Fig 2.4 d shows a more recently developed profile that produces a uniform wakefield while also being smoothly varying. This profile is relevant even without having

the highest TR achievable because of this smoothness, which makes it easier to accurately produce via previously discussed bunch shaping methods. We will find out why this is relevant in the next section.

Making a uniform decelerating wakefield also maintains the drive beam profile throughout the interaction. In a case where the beam particles uniformly lose energy, beam energy spread remains constant inside the plasma. This prevents particles in the beam from losing too much energy and becoming sub-relativistic, which will cause them to lag behind and slip out of phase with the interaction. Beam particles that have the same energy also oscillate transversely at the same frequency, which reduces emittance growth in a uniform focusing channel (see Section 2.4.2).

2.2.2 Effects of Profile Sharpness on TR

One feature that all high transformer ratio profiles share is a sharp cutoff after the ramp area. We can view this requirement by considering a beam loading argument. We imagine that the stored energy in the wakefield adds up slowly over the beam current ramp. If we want to maximize the accelerating wakefield experienced by a witness beam, it is important that the wakefield energy is not absorbed by trailing particles in the drive. Any particles in a "tail" behind the ramp cutoff load the wakefield and reduce the peak accelerating gradient.

A demonstration of this effect is seen in Fig. 2.5. To simulate the development of a tail, we multiply the ideal linear ramped profile by the function

$$F(\xi) = \frac{1}{e^{(\xi - L)/T} + 1} \tag{2.25}$$

where L is the overall drive length and T is a parameter that controls the tail length. For $T \to 0$ we recover a discontinuity at the linear ramp end which matches the ideal profile. As T increases the tail lengthens and the transformer ratio suffers due to a reduction in the peak accelerating field. Unfortunately, some tail growth is unavoidable when transporting a beam through the accelerator [48]. We will see that higher order effects in the emittance exchange beamline and phase slippage in the plasma beamline both contribute to growth of tails behind the linear ramp section. This smoothing effect is generally true for all sharp features in a given distribution. This explains the particular significance of using smoothly varying profiles, which are less dependent on maintaining sharp features in the distribution

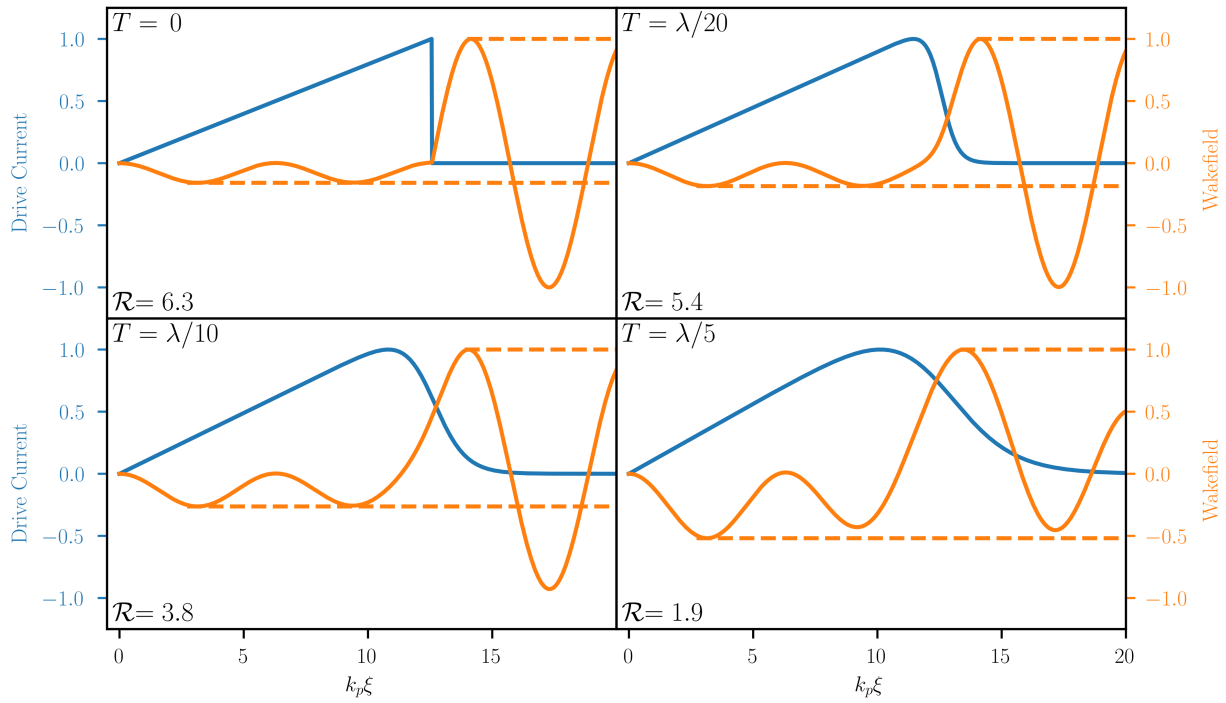

Figure 2.5: Plots showing effect of tail growth on the transformer ratio from a linearly ramped drive over two characteristic wavelengths.

head when compared to the doorstep and double-triangle profiles.

2.3 Plasma Wakefields

With our understanding of beam based wakefields in hand, we are equipped to analyze wakefields excited in plasmas. We start by examining wakes in a 1D and quasi-3D (cylindrically symmetric) linear plasma. We then expand our analysis to include a multi-dimensional, non-laminar response which gives rise to a blowout plasma response, where a rarefaction region with no plasma electrons develops behind the drive. Finally, we examine particle-in-cell simulation results to predict the actual wakefield response.

2.3.1 Plasma Wakefields in the Linear Regime

Our goal is to describe the plasma response to a drive beam and then determine wakefields from the plasma response self consistently using analysis pioneered by Ruth et. al.[49]. We

imagine a stationary, cold, quasi-neutral[2] plasma into which we inject our electron drive beam.

To solve for the plasma electron response we begin with Maxwell's equations [50]

$$\nabla \cdot \mathbf{E} = 4\pi\rho \tag{2.26a}$$

$$\nabla \cdot \mathbf{B} = 0 \tag{2.26b}$$

$$\nabla \times \mathbf{E} = -\frac{1}{c}\frac{\partial \mathbf{B}}{\partial t} \tag{2.26c}$$

$$\nabla \times \mathbf{B} = \frac{1}{c}\Big(\frac{\partial \mathbf{E}}{\partial t} + 4\pi\mathbf{J}\Big) \tag{2.26d}$$

where $\mathbf{J} = \rho\mathbf{v}$ is the current density. By taking the divergence of $\nabla \times \mathbf{B}$ and substituting the differential form of Gauss's law in for $\mathbf{E}$ we get the continuity equation

$$\frac{\partial \rho}{\partial t} + \rho\nabla \cdot \mathbf{v} = 0. \tag{2.27}$$

The charge particle density at any location in a beam-plasma interaction consists of plasma electrons, plasma ions and beam electrons such that $\rho = -e(n_e - n_i + n_b)$. Due to their relatively large mass, plasma ions move much slower than either electron species during the interaction so here we assume that they are static during the interaction and simply provide a neutralizing effect on plasma electrons. In a neutral plasma, $n_e = n_i = n_0$ is the unperturbed plasma density. We concern ourselves with small perturbations in the electron density $n_e(\mathbf{x}, t) = n_0 + \delta n_1(\mathbf{x}, t)$ where $\delta \ll 1$. We can also expand the plasma electron velocity to be $\mathbf{v}(\mathbf{x}, t) = \mathbf{v_0} + \delta\mathbf{v_1}(\mathbf{x}, t)$. Assuming that the plasma electrons are initially at rest ($\mathbf{v_0} = 0$) we can calculate a linearized version of the continuity equation for the plasma response

$$\frac{\partial n_1}{\partial t} = -n_0\nabla \cdot \mathbf{v_1} \tag{2.28}$$

where we have neglected terms $\mathcal{O}(\delta^2)$.

Evolution of the plasma electrons is determined by the Lorentz force equation for cold, collisionless fluid elements of the plasma,

$$m_e\frac{\partial \mathbf{v}}{\partial t} + m_e\mathbf{v} \cdot \nabla\mathbf{v} = -e(\mathbf{E} + \mathbf{v} \times \mathbf{B}/c) \tag{2.29}$$

[2]Term definitions are as follows. Stationary: electron and ion velocities average to zero. Cold: the rms kinetic energy of particles in the plasma is small compared to the ionization energy. Quasi-neutral: electron and ion densities are roughly equal over the entire plasma.

or in the linearized form

$$m_e \frac{\partial \mathbf{v_1}}{\partial t} = -e(\mathbf{E} + \mathbf{v_1} \times \mathbf{B}/c) \tag{2.30}$$

We restrict ourselves to considering electrostatic waves ($\mathbf{B} = 0$) which is implied when electromagnetic waves in the plasma are purely longitudinal [49]. When this is the case

$$\frac{\partial \mathbf{E}}{\partial t} = -4\pi \mathbf{J} \tag{2.31a}$$

$$m_e \frac{\partial \mathbf{v_1}}{\partial t} = -e\mathbf{E} \tag{2.31b}$$

If we take the time derivative of Eqn. 2.28 and substitute in our Lorentz force equation we get

$$\frac{\partial^2 n_1}{\partial t^2} = \frac{e n_0}{m_e} \nabla \cdot \mathbf{E} = -\omega_p^2 (n_1 + n_b) \tag{2.32}$$

where $\omega_p^2 = 4\pi e^2 n_0 / m_e$ is the characteristic plasma frequency. Rearrangement gives a forced wave equation for the perturbed plasma density

$$\frac{\partial^2 n_1}{\partial t^2} + \omega_p^2 n_1^2 = -\omega_p^2 n_b^2. \tag{2.33}$$

We can assume a quasi-static approximation, where the plasma perturbation is static in a frame traveling with the electron beam and thus is a function of the longitudinal variable $\xi = z - v_b t$. Through this change of variables our final linear wave equation is given by

$$\frac{\partial^2 n_1}{\partial \xi^2} + k_p^2 n_1 = -k_p^2 n_b \tag{2.34}$$

where $k_p = 2\pi/\lambda_p = \omega_p / v_b$.

So far we have not assumed anything about the overall beam geometry. We will now consider our beams to be rotationally symmetric and that their density profile has a separable form $n_b(r, \xi) = \sigma(r)\lambda(\xi)$. In this case, perturbations to the plasma should have a corresponding separable form $n_1(r, \xi) = \Sigma(r) Z(\xi)$. Inserting this into our wave equation, we get separable forms of the plasma response

$$\frac{\partial^2 Z(\xi)}{\partial \xi^2} + k_p^2 Z(\xi) = -k_p^2 \lambda(\xi) \tag{2.35a}$$

$$\Sigma(r) = \sigma(r). \tag{2.35b}$$

Looking at this set of equations we observe that the transverse plasma response is proportional to the transverse beam profile.

To calculate the longitudinal plasma response we first examine a delta-function like beam $\lambda(\xi) = \delta(\xi)$. If we integrate over $\xi = 0$ we find that

$$\frac{\partial Z}{\partial \xi}\Big|_{0-}^{0+} = -k_p^2. \tag{2.36}$$

Outside the region where beam is present, plasma perturbation follows the solutions to the homogeneous wave equation. Causality sets the perturbation ahead of the beam ($\xi < 0$) to zero and at the beam location ($\xi = 0$) to 1/2. Behind the beam ($\xi > 0$) the solution is a pure sinusoid, thus the longitudinal plasma response is

$$Z(\xi) = \begin{cases} 0 & \xi < 0 \\ -\frac{k_p}{2} & \xi = 0 \\ -k_p \sin(k_p \xi) & \xi > 0. \end{cases} \tag{2.37}$$

and the full plasma perturbation functional form is given by

$$n_1(r, \xi) = \begin{cases} 0 & \xi < 0 \\ -\frac{k_p \sigma(r)}{2} & \xi = 0 \\ -k_p \sigma(r) \sin(k_p \xi) & \xi > 0. \end{cases} \tag{2.38}$$

and the wakefield is simply calculated from Gauss's law

$$\nabla \cdot \mathbf{E} = 4\pi e(n_1 + n_b). \tag{2.39}$$

First we can consider a 1-dimensional response where the beam has no transverse density dependence $\sigma(r) = \sigma$. Here our field divergence simplifies to $\nabla \cdot \mathbf{E} = dE/d\xi$ and the resulting wakefield is calculated to be

$$W_\xi(\xi) = \begin{cases} 0 & \xi < 0 \\ 2\pi\sigma & \xi = 0 \\ 4\pi\sigma \cos(k_p \xi) & \xi > 0. \end{cases} \tag{2.40}$$

This matches the wakefield response for a delta function drive beam derived in the previous section, meaning that all our analysis about wakefields can be applied to wakes in the linear plasma regime, including those regarding limits on transformer ratio.

To solve for the plasma perturbation from an arbitrary current distribution, we convolve these solutions found for a delta function with the longitudinal profile to get

$$n_1(r,\xi) = \begin{cases} 0 & \xi < 0 \\ -\frac{k_p\sigma(r)}{2} & \xi = 0 \\ -k_p\sigma(r)\int_\xi^\infty \lambda(\xi)\sin(k_p(\xi'-\xi))d\xi' & \xi > 0. \end{cases} \tag{2.41}$$

The wakefield is calculated from this as before to retrieve the same functional form of Eqn. 2.15

$$W_\xi(\xi) = -W_0\int_\xi^\infty \lambda(\xi')\cos(k(\xi'-\xi))d\xi'. \tag{2.42}$$

Now we will take a look at the three dimensional linear wakefield response. We use our calculated plasma perturbation (Eq. 2.41) and the cylindrical coordinate system form for Gauss's law to calculate the electrostatic wakefields in both z and r directions. To simplify our analysis we introduce the electrostatic potential $\mathbf{E} = -\nabla\Phi$ for which we will solve for, and then calculate the wakefield. The potential equation in cylindrical coordinates is

$$\frac{1}{r}\frac{\partial}{\partial r}\Big(r\frac{\partial}{\partial r}\Phi\Big) + \frac{\partial^2\Phi}{\partial\xi^2} = -4\pi e(n_1 + n_b) \tag{2.43}$$

To analyze wakefield dependence on the transverse coordinate, we imagine a parabolic distribution [3] for the transverse beam density and a similar delta function beam in the longitudinal coordinate

$$\sigma(r) = \begin{cases} \frac{2N}{\pi a^2}(1 - r^2/a^2) & r < a \\ 0 & r > a. \end{cases} \tag{2.44}$$

Remembering that the plasma perturbation dependence on r is equal to $\sigma(r)$, the solution to Eqn. 2.12 behind the beam is

$$\Phi(r,\xi) = \frac{16eN}{k_p a^2}\sin(k_p\xi)\begin{cases} K_2(k_pa)I_0(k_pr) + \frac{1}{2} - \frac{2}{(k_pa)^2} - \frac{r^2}{2a^2} & r < a \\ I_2(k_pa)K_0(k_pr) & r > a \end{cases} \tag{2.45}$$

where I_n, K_n are modified Bessel functions of the first and second kind respectively. Taking the the cylindrical coordinate derivatives, we calculate the resulting wakefield inside the

[3] chosen due to solution simplicity

beam radius ($r < a$) to be

$$E_\xi = -\frac{16eN}{a^2}\cos(k_p\xi)\left[K_2(k_pa)I_0(k_pr) + \frac{1}{2} - \frac{2}{(k_pa)^2} - \frac{r^2}{2a^2}\right] \tag{2.46a}$$

$$E_r = -\frac{16eN}{a^2}\sin(k_p\xi)\left[K_2(k_pa)I_1(k_pr) - \frac{r}{k_pa^2}\right] \tag{2.46b}$$

If we consider a wide beam were $k_pa \ll 1$ and we look near the beam axis where $r \ll a$, the wakefields simplify to

$$E_\xi \approx \frac{-8eN}{a^2}\left(1 - \frac{r^2}{a^2}\right)\cos(\xi) \tag{2.47a}$$

$$E_r \approx \frac{16eN}{a^2}\left(\frac{r}{k_pa^2}\right)\sin(\xi). \tag{2.47b}$$

From this we can see that on-axis the wakefield has a sinusoidal longitudinal dependence that matches our 1D analysis. For the transverse fields is interesting to note that it has a linear radial dependence which provides a focusing or defocussing force on the beam depending on the sign of $\sin(k_p\xi)$ as seen in Figure 2.6. The focusing and longitudinal forces are offset by $\pi/2$ which means a region exists that is simultaneously accelerating and focusing.

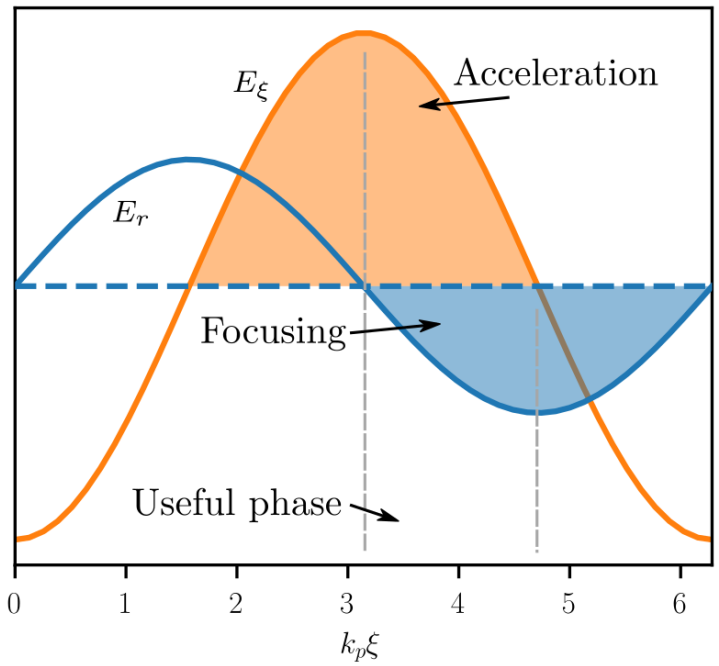

Figure 2.6: Plot showing the longitudinal and transverse wakefields on-axis from a parabolic transverse and a delta-like longitudinal distribution.

2.4 Plasma Wakefields in the Nonlinear Regime

If we increase the overall density of our beam relative to the unperturbed plasma to be on the same order of magnitude or greater, the electronic response will grow such that the perturbation to plasma density will no longer be small relative to the background plasma. This regime is especially interesting when the beam is dense enough that it creates a rarefied region behind the drive where no plasma electrons remain. In this region the electrostatic fields are particularly appealing for preserving beam quality as the accelerating field is independent of transverse position and radial fields confine beam particles similar to a linear focusing magnet [51] .

Initial investigation in one dimension was carried out by Dawson [52] and Ahkiezer and Polovin [53] in the 1950's. Dawson in particular examined 1D oscillations of uniform charge "sheets" in plasma. His analysis found that electron sheets will oscillate with a simple harmonic motion until the oscillation amplitude increases such that the sheets begin to intersect with one-another and linear oscillation analysis breaks down. This oscillation limit corresponds to an electric field known as the "wave-breaking" limit given by

$$E_{WB} = \frac{m_e c \omega_p}{e}. \tag{2.48}$$

Further analysis of nonlinear 1D oscillations note that the waveform of these wakefields are steepened due to higher harmonics and that when the particle velocities become relativistic periodicity of their oscillations increases [54].

However, before accessing nonlinearities described above, transverse motion of the plasma particles dominates [51]. Plasma electrons are expelled completely from the beam axis while ions are left behind (due to their relatively high mass) creating a region of uniform ion density with no plasma electrons behind the beam. This is often referred to as the plasma blowout. Eventually electrons expelled from the axis collapse back onto the axis, creating a significant spike in electron density that can be a few orders of magnitude higher than the unperturbed density.

Until recently, little analytical theory has been found that completely describes the three dimensional plasma response in the nonlinear regime. This is due to complexities created by the regime's electromagnetic nature, relativistic mass increases of plasma electrons and non-laminar flow. Thanks to work done by Lu et.al. [55] we can describe certain aspects of

the rarefaction response in the first accelerating "bucket" before phase mixing occurs.

2.4.1 Transitioning to the Blowout Regime

Establishment of a transverse region where no plasma electrons exist is the central aspect of nonlinear behavior in response to an electron beam. The so called "ion column" that remains in this region gives rise to characteristic uniform accelerating and focusing fields that we will examine later. We explore the formation of this regime using a simple sheet crossing[4] model discussed previously by Dawson [52]. In a similar way to Dawson's analysis we will consider a breakdown in laminar flow ie. sheet crossing as the metric for defining the beginning of a nonlinear response.

We start by considering a rotationally symmetric system as before, with an array of plasma electrons spaced equally apart from one another at different radii. We also imagine the same moving frame of reference for a relativistic beam as before, where the longitudinal coordinate becomes $\xi = z - ct$. A plasma particle starts at $\xi = 0$ with a radius of $r(0) = r_0$ and moves in the positive ξ direction due to being still in the stationary frame. If these particles evolve in such a way that their trajectories $r(\xi, r_0)$ do not cross, then the flow is to be considered laminar and a particle who starts at a radius $r_0 > 0$ will always see electrons on either side of it. If trajectories do cross, then there is going to be a particle that does not see any plasma electrons beneath it i.e. no particles in the region $< r^*(\xi, r_0)$ where r^* represents the trajectory that satisfies our condition for blowout.

We start with a restatement of Maxwell's equations in the same moving coordinate system as before, $\xi \equiv z - ct$ and in the Lorentz gauge,

$$-\nabla_\perp^2 \mathbf{A} = \mathbf{J} \tag{2.49a}$$

$$-\nabla_\perp^2 \phi = \rho \tag{2.49b}$$

$$\nabla_\perp \cdot \mathbf{A}_\perp = -\frac{\partial \psi}{\partial \xi} \tag{2.49c}$$

where we have separated the longitudinal and transverse components of the vector fields and introduced the pseudo-potential $\psi = \phi - A_z$, $\nabla_\perp \equiv \hat{x}\partial/\partial x + \hat{y}\partial/\partial y$.

The evolution of plasma electrons can be shown [56] to evolve simply due to the Lorentz

[4] in cylindrical coordinates this ends up being a ring

force equation

$$\frac{d}{d\xi}\mathbf{p}_\perp = -\frac{1}{1-v_z}[\mathbf{E}_\perp + (\mathbf{v}\times\mathbf{B})_\perp] \tag{2.50}$$

where the vector subscript $\perp$ denotes transverse components only. We have also normalized time to ω_p^{-1}, distances to c/ω_p, masses to m_e, charge to e, potentials to mc^2/e, fields to $mc\omega_p/e$, charge density to en_0 and current density to en_0c.

The pseudo-potential ψ obeys a modified Poisson-like equation

$$-\nabla_\perp^2\psi = \rho - J_z \tag{2.51}$$

where the continuity equation becomes

$$\frac{\partial}{\partial\xi}(\rho - J_z) + \nabla_\perp\cdot\mathbf{J}_\perp = 0. \tag{2.52}$$

From this is magnetic and electric fields can be calculated as

$$E_z = \frac{\partial\psi}{\partial\xi} \tag{2.53a}$$

$$B_z = (\nabla_\perp\times\mathbf{A}_\perp) \tag{2.53b}$$

$$\mathbf{E}_\perp = -\nabla_\perp\phi - \frac{\partial\mathbf{A}_\perp}{\partial\xi} \tag{2.53c}$$

$$\mathbf{B}_\perp = \nabla_\perp\times(A_z\hat{z}) + \nabla_z\times\mathbf{A}_\perp \tag{2.53d}$$

and we see that the longitudinal electric field $E_z(r,\xi)$ is simply equal to the longitudinal derivative of the pseudo-potential.

If we assume that the plasma particles are non relativistic $v_z << 1$ then induced magnetic fields due to plasma particle motion is negligible. We can also approximate the transverse velocity as $v_\perp \approx dr/d\xi$. These assumptions lead us with plasma electron trajectories dependent on electrostatic forces

$$\frac{d^2r}{d\xi^2} = -E \tag{2.54}$$

from plasma electrons, plasma ions and beam particles. We now follow cylindrical sheet analysis put forward by Dawson [52]. If we assume that the electric field is solely a function of the charge inside our sheet then the electric field is simply calculated using the integral form for Gauss' law, giving the equation of motion

$$\frac{d^2r}{d\xi^2} = -\Big[\frac{r}{2} - \frac{c(r_0,r,\xi)}{r}\Big] \tag{2.55}$$

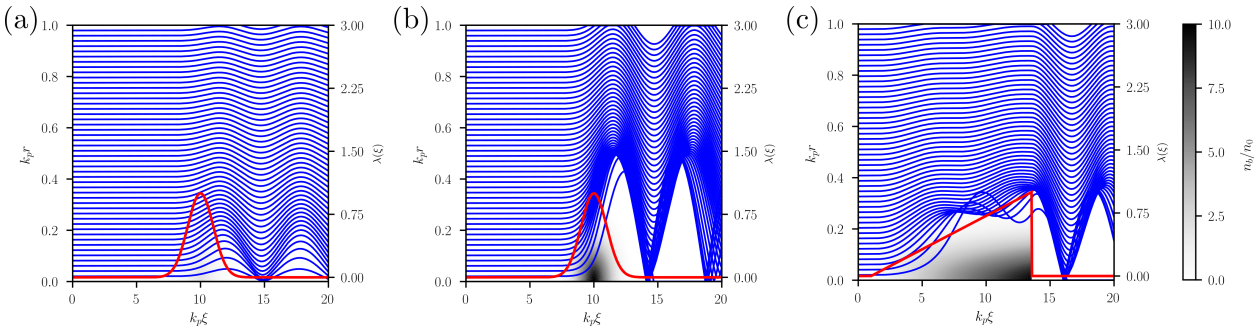

Figure 2.7: Plots of plasma electron trajectories with three different beam distributions (shown as background shading). (a) A bi-Gaussian distribution with $\sigma_z = 1$, $\sigma_r = 0.1$, and a peak density of $n_{b0} = 2$. (b) A bi-Gaussian distribution similar to (a) but with a peak density of $n_{b0} = 10$. (c) A transverse Gaussian with $\sigma_r = 0.1$ and a linear ramp for $\lambda(\xi)$ with a length of $L = 2\pi$ and a peak density of $n_{b0} = 10$.

where the first term is due to the uniform ion density, and the second is due to electron charge. Net electron charge per unit length inside the trajectory $r(\xi)$ from both the plasma and the beam is given by

$$c(r_0, r, \xi) = \frac{1}{2} r_0^2 + \int_0^r r' n_b(r', \xi) dr'. \tag{2.56}$$

where n_b is normalized to the unperturbed plasma density n_0. Substituting this into our equation of motion we get

$$\frac{d^2 r}{d\xi^2} = -\Big[\frac{r}{2} - \frac{\frac{1}{2} r_0^2 + \int_0^r r' n_b(r', \xi) dr'}{r}\Big]. \tag{2.57}$$

This differential equation can be solved numerically with the initial conditions $r(0) = r_0$ and $dr/d\xi = 0$ for a plasma electron. If we assume a beam distribution with the form

$$n_b(r, \xi) = n_{b0} \exp\Big[-\frac{r^2}{2\sigma_r^2}\Big] \lambda(\xi) \tag{2.58}$$

where n_{b0} is the peak beam density at $r = 0$ we can plot plasma electron trajectories for different longitudinal distributions as seen in Fig. 2.7.

The plots here show the transition from non-trajectory crossing (linear) regime to trajectory crossing (nonlinear) regime. When the peak bunch density is up to two times the background plasma density (Fig. 2.7a), the trajectories are perturbed, but no rarefaction occurs. When the peak beam density is $n_{b0} = 10 n_0$ (Fig. 2.7b) trajectory crossing occurs, resulting in a rarefaction region behind the bunch that lasts roughly half a plasma wavelength.

In the presence of a linearly ramped beam with a peak density of $n_{b0} = 10n_0$ (Fig. 2.7(c)) trajectory crossing does not occur during the first half of the ramp due to the low charge in the beam head. We will see later that this internal regime change in the beam will effect how different slices of beam get accelerated and focused differently, leading to asymmetries in the longitudinal wakefield and in transverse oscillations during propagation in a plasma. We also observe a second oscillation in the rarefaction boundary, due to the beam being longer than a single wavelength. It is instructive to note that for the examples here, particles far off-axis experience a linear perturbation that retains their laminar behavior. This is due to screening effects of the plasma electrons closer to the axis.

The next step in our analysis is to investigate the geometry of rarefaction boundary as a function of beam distribution. This is important because we expect the evolution of beam particles to differ significantly depending on their location, either inside or outside of the rarefaction region, due to the contribution (or lack thereof) of plasma electrons to the particle motion.

The bubble boundary dictates the on-axis longitudinal wakefield. Lu et. al.[55] employs a step model to fit the electron sheath boundary. From this, they are able to calculate the pseudo-potential for $r \leq r_b$ to be

$$\psi(r,\xi) = \frac{r_b^2(\xi)}{4}(1+\beta(\xi)) - \frac{r^2}{4} \tag{2.59}$$

where

$$\beta(\xi) = \frac{(1+\alpha^2)\ln(1+\alpha^2)}{(1+\alpha^2)-1} - 1 \tag{2.60a}$$

$$\alpha \equiv \frac{\Delta}{r_b} = \frac{\Delta_L}{r_b} + \frac{\Delta_s}{r_b}. \tag{2.60b}$$

The constants $\Delta \equiv \Delta_L + \Delta_s$ corresponds to the high density sheath thickness observed in PIC simulations at the bubble boundary plus a linear response region with a plasma wave number thickness. Generally $\Delta_s/r_b << 1$ except near the back of the bubble where this thickness starts to approach the blowout radius.

We calculate the rarefaction region boundary $r_b(\xi)$ using a differential equation found by

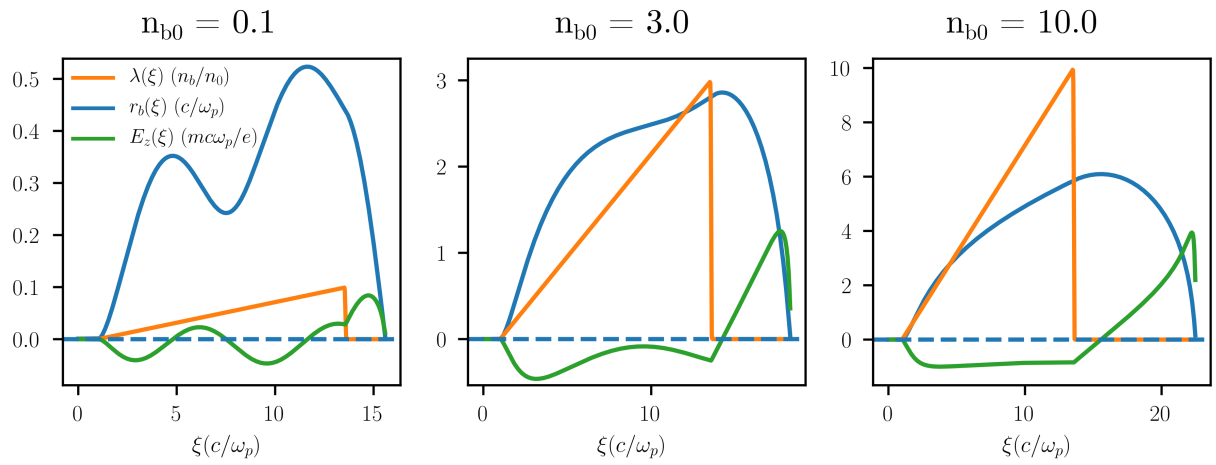

Figure 2.8: Numerical calculations of blowout radius and on-axis electric field due to linearly ramped beams of varying peak density.

Lu et. al.

$$A(r_b)\frac{d^2 r_b}{d\xi^2} + B(r_b) r_b \left[\frac{dr_b}{d\xi}\right]^2 + C(r_b) r_b = \frac{\lambda(\xi)}{r_b} \tag{2.61a}$$

$$A(r_b) = 1 + \left[\frac{1}{4} + \frac{\beta}{2} + \frac{1}{8} r_b \frac{d\beta}{dr_b}\right] r_b^2 \tag{2.61b}$$

$$B(r_b) = \frac{1}{2} + \frac{3}{4}\beta + \frac{3}{4} r_b \frac{d\beta}{dr_b} + \frac{1}{8} r_b^2 \frac{d^2\beta}{dr_b^2} \tag{2.61c}$$

$$C(r_b) = \frac{1}{4}\left[1 + \left(1 + \frac{\beta}{4} r_b^2\right)^{-2}\right] \tag{2.61d}$$

where $\lambda(\xi) = \int_0^{r>>\sigma_r} r' n_b(r', \xi) dr'$ is the beam longitudinal current density. We expect errors in the calculated blowout radius at the rear of the blowout as the blowout radius approaches Δ_s. The set of equations can be solved numerically, and once the profile $r_b(\xi)$ is known, the longitudinal wakefield inside the bubble region $r < r_b(\xi)$ can be calculated as

$$E_z(r, \xi) = \frac{\partial}{\partial \xi}\psi(r = 0, \xi) = \frac{d}{d\xi}\left[\frac{1}{4} r_b(\xi)^2 (1 + \beta(\xi))\right]. \tag{2.62}$$

Numerical solutions for the blowout radius and on-axis electric field are seen for varying current profiles in Fig. 2.8. We can see the dramatic scaling of the blowout bubble size as we increase the peak beam density. This in turn increases the peak electric field strength at the back edge of the bubble region, where a suitable witness bunch would be placed.

It is interesting to note that the longitudinal wakefield is $E_z \propto r_b(\xi)' r_b(\xi)$ where $'$ denotes $d/d\xi$. From this we can see that field has zero crossings at the longitudinal location of bubble maxima as $r_b' = 0$. This is particularly evident in the blowout calculation seen in Fig. 2.8 for

$n_{b0} = 0.1$ as the bubble has three local extrema and thus has an accelerating region midway through the beam profile. To prevent this from happening, we must excite the bubble such that it is monotonically increasing inside the drive region.

To understand why the bubble boundary partially collapses we consider how strongly the driver beam expels electrons from the axis. In the limit where maximum blowout radius is $r_m << 1$ we consider the plasma electrons expelled by the beam to be non-relativistic, conversely if $r_m >> 1$ the electrons are considered ultra-relativistic. To provide insight into these two limits we examine key features in what contributes to the wakefield inside the bubble. We consider three regions that contribute to the on-axis pseudo-potential: the ion channel inside the bubble, the high density electron boundary and a linear response region outside the bubble. By integrating Eqn. 2.51 we get

$$\psi(0,\xi) = \int_0^\infty \frac{dr}{r} \int_0^r (\rho - J_z/c) r' dr' \tag{2.63a}$$

$$= \left(\int_0^{r_b} + \int_{r_b}^{r_b+\Delta_s} + \int_{r_b+\Delta_s}^\infty \right) \left[\frac{dr}{r} \int_0^r (\rho - J_z/c) r' dr' \right] \tag{2.63b}$$

$$= \psi_{\text{ion}} + \psi_{\text{s}} + \psi_{\text{linear}} \tag{2.63c}$$

where ψ_{ion}, ψ_{s}, ψ_{linear} represents the contributions from each region respectively. As the only charge in the blowout region is the static uniform background ion charge $\psi_{\text{ion}} = r_b^2/4$. The charge contained in the sheath is generally small compared to the charge in the bubble for most ξ so the contribution ψ_{s} is equally small when compared to the ionic contribution. The linear term is due to the plasma response within roughly ($r < c/\omega_p$) as the perturbation is screened due to plasma electron motion. The relevance of the ψ_{linear} term is dependent on the relative size of the bubble region. In the non-relativistic limit, the bubble is small so this term dominates, otherwise in the relativistic limit the ionic term is much larger.

The interpretation of this analysis can be extended to explain the blowout geometry dependence on beam charge seen in Fig. 2.8. When $n_{b0} = 0.1$ the maximum blowout radius is $r_m < 1$ or in the non-relativistic limit. Here, the linear region outside the bubble dominates and plasma electrons return to the axis after roughly one half oscillation period. When the bubble is large $r_m > 1$ the plasma electrons are relativistic and the forces that cause the linear plasma response no longer dominates. Furthermore, we observe that the electric field oscillation period inside the drive increases with increased blowout. Since the electric field directly correlates to the periodicity of plasma electron motion, we can infer that the plasma

oscillation period increases as well. This matches with one of the main predictions from 1D nonlinear theory as it was found that the relativistic mass increase of plasma electrons contributes to a modification of oscillation frequency [54].

These observations present a good case for using ramped beams in the blowout regime to achieve high transformer ratios. In the non-relativistic limit, analysis discussed here and previous work using PIC simulations [57] have shown that the wakefield response in the drive can be approximated as a linear, single mode response. This approximation breaks down after the drive however, with a nonlinear response due to the final collapse of the bubble that results in a sawtooth-like wakefield in this region. In the ultra-relativistic case, we see that the drive wakefield has become roughly uniform due to the plasma electron's relativistic motion, which is also shown in PIC simulation results [58]. As we have seen previously, uniformization of the drive wakefield in the linear regime requires finely tuned changes to the linearly ramped profile of the drive beam. Here though, this effect is achieved just by increasing the response nonlinearity, either by increasing beam density or decreasing plasma density. This bodes well for real-world application, as complex beam current distributions are difficult to produce and this presents a viable alternative.

2.4.2 Transverse Forces

To calculate transverse forces inside the bubble we use Eqns. 2.51 and 2.53c. In the electrostatic approximation $\mathbf{A} = 0$ so that the equation for transverse electric field is

$$\mathbf{E}_\perp = -\nabla_\perp \psi = -\frac{\partial}{\partial r}\frac{r^2}{4} \tag{2.64a}$$

$$= -r/2 \tag{2.64b}$$

thus the electric field inside the ion region acts as a focusing force on the beam. In practical units the focusing strength is given by

$$K \equiv -\frac{eE_r}{\gamma r_e m_e c^2} = \frac{2\pi r_e n_0}{\gamma}. \tag{2.65}$$

This parameter dictates the transverse rms envelope of the beam σ_r as it travels through the plasma according to [59]

$$\sigma_r'' + K\sigma_r = \frac{\epsilon^2}{\sigma_r^3} \tag{2.66}$$

where $'$ denotes a derivative with respect to path coordinate s and $\epsilon = \sqrt{< r^2 >< r'^2 > - < rr' >^2}$ is the conserved transverse geometric emittance of the beam. The betatron function is defined as $\beta = \sigma_r^2/\epsilon$, once substituted into the above equations gives

$$\beta'' + 2K\beta = \frac{1}{\beta}\left[\frac{\beta'}{2} + 2\right]. \tag{2.67}$$

For stable (equilibrium) propagation through the plasma $\beta_{eq} = \text{const}, \beta'' = \beta' = 0$ resulting in $\beta_{eq} = K^{-1/2}$ as a solution. If a beam enters the plasma with a corresponding transverse size of

$$\sigma_{eq} = \sqrt{\beta_{eq}\epsilon} = \left[\frac{\epsilon}{\sqrt{2\pi r_e n_0 \gamma}}\right]^{1/2} \tag{2.68}$$

it will remain at that size throughout the interaction. If the beam is not at the correct size, we expect its betatron envelope to oscillate through the plasma interaction [60]. Significant work has been done exploring how to match beam size effectively into the plasma to prevent unwanted emittance growth [61, 62, 63]. It has been found that tuning the plasma density profile from zero to peak density adiabatically ie. the plasma density rises over several betatron oscillation periods, matches the beam to the final plasma density without growth in the emittance.

This is complicated by the long beam we use to create high transformer ratio due to its length relative to the plasma wavelength. We have discussed previously, that the blowout region does not start immediately due to the low charge at the head. This means that the beam head is focused differently compared to the main body of the beam and it develops into three distinct regions [64]: a freely expanding head, a pinch region where the plasma electrons have had time to respond to fields from the beam, and a body region which feels the full focusing forces in the ion column as discussed previously. These differences throughout the beam result in several transverse instabilities in a long beam [65]. Further complications evolve from the finite energy spread induced in the drive beam by the wakefield. During betatron oscillations, particles with different energies will oscillate with varying frequencies. The projected phase space envelope will eventually be filled by the different slices of the beam if it undergoes oscillations. This can be reduced by better beam matching that prevents betatron oscillations.

Parameter	Value	Unit
Beam Charge	1.8	nC
Drive Charge (Witness Charge)	1.78 (0.02)	nC
Beam Energy	40	MeV
σ_r	200	μm
$\epsilon_{r,n}$	100	mm.mrad
Drive Ramp Length	6	mm
Witness Delay	500	μm
Witness Length	4	mm
Plasma Density	1.3×10^{14}	cm^{-3}

Table 2.1: Ramped beam and plasma parameters for Warp simulations.

2.4.3 3D PIC Simulations

With our understanding of the central principals of wakefield acceleration and its relevance to plasma wakes, we can now employ simulation tools to examine the specific dynamics in our experiment. For this we employ the use of a 3D particle in cell (PIC) developed by Berkley called WARP [66]. This code simulates the time dependent beam-plasma response using a collection of macro-particles and calculates the self-consistent electromagnetic fields in a discretized cylindrical coordinate system. For accurate simulations, the cell size was scaled to the unperturbed plasma wavelength [5]. Simulations were run on an eight core parallel processor to reduce computation time.

To simulate the dynamics expected in our experiment beam and plasma parameters where chosen in accordance with prior measurements of the beam and plasma separately. These parameters are seen in Table 2.1. For simplicity, we assume that the beam is focused by a density ramp that the beam experiences as it enters the plasma region. This profile is poorly characterized (see Chapter 4) so we set up our simulation to be a uniform plasma density and account for the focusing by reducing the input beam size. The results of our simulation are seen in Fig. 2.9. We show three transverse profiles of the beam and plasma distribution at different locations along the interaction. Before entering the plasma, our beam has a gaussian transverse profile and a linearly ramped current distribution (as seen

[5] 20 cells per λ_p for low accuracy and up to 200 cells per λ_p for highest accuracy

by the green line in the figure) with a small tail, consistent with simulated beams going through our plasma beamline (see Chapter 5). A witness bunch with a low charge is placed behind the drive to sample the wakefield response [6].

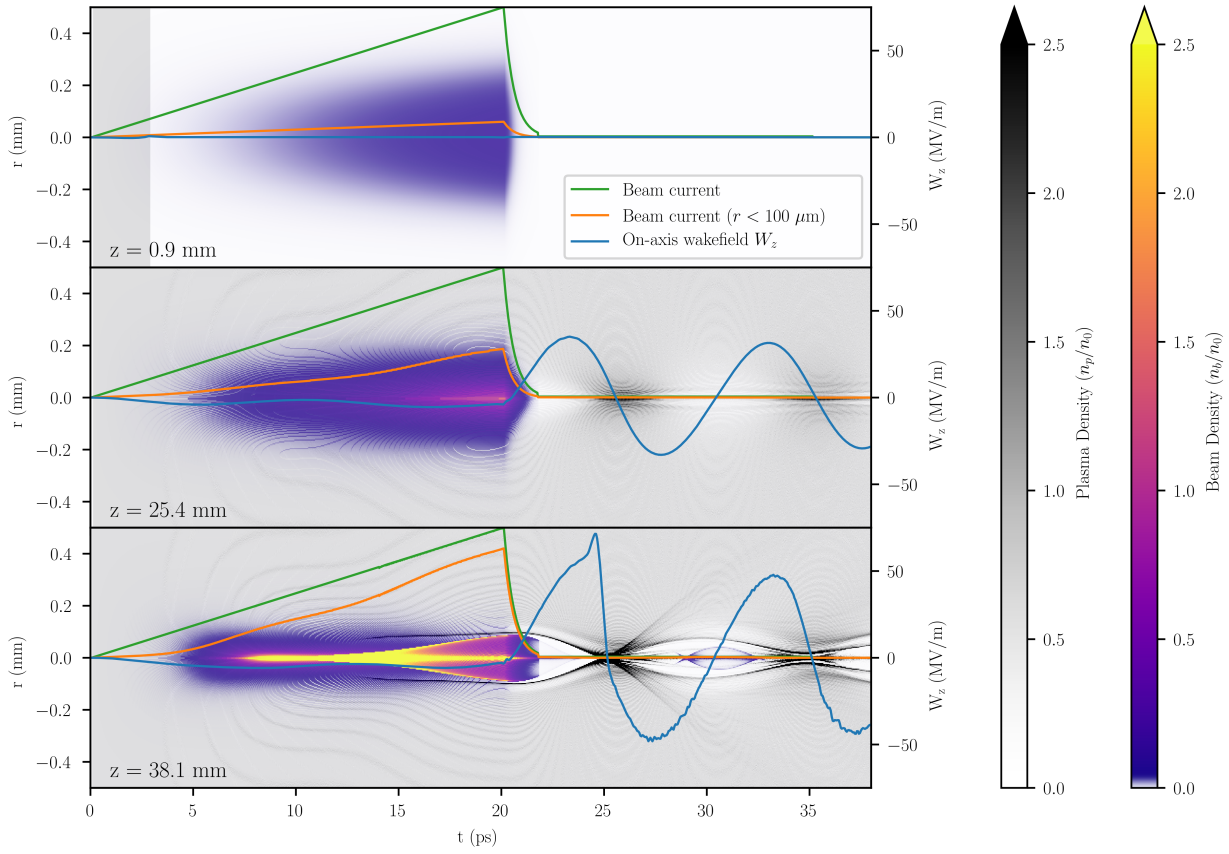

Figure 2.9: Transverse distribution of beam and plasma electrons calculate at several points throughout the interaction.

We observe a significant change in the beam distribution as it propagates further into the plasma. As discussed previously the beam experiences transverse focusing from the displacement of plasma electrons. The beam head is not focused significantly due to the low beam charge in this region. It also takes time for the plasma electrons to react the beam electrons, thus in this region the plasma remains mostly uniform in nature. This leads to a freely expanding beam head, which is indicated by the overall loss of near-axis particles (orange line).

The beam body on the other hand, does experience a strong focusing force until the

[6]It should be noted that the witness bunch here has significantly less charge than what we expect from experiment. Simulations shown here are solely used to explore unloaded wakefield effects.

beam density exceeds the plasma density, contributing to nonlinear effects in the on-axis wakefield. Further back from the head, the plasma electrons are off-axis resulting in a net focusing force which compresses the transverse size of the beam. We observe that initially, the on-axis longitudinal wakefield resembles a sinusoidal, linear response. However, once the beam is focused more downstream, the beam density on axis exceeds the plasma density, and starts to produce a rarefied plasma region. Resulting nonlinearities from the plasma electron collapse back on-axis creates a nonlinear wakefield and we observe the development of a sawtooth like structure evident from the addition of higher harmonics in the wakefield response.

We also observe that our plasma blowout is non-relativistic, as evidenced by the small blowout radius compared to k_p^{-1}. As we discussed previously, the on-axis wakefield inside the bubble is dependent on potentials from the bubble region, the sheath region, and the linear region outside the bubble. In our simulations we see that the bubble radius is roughly 100 μm, which is significantly less than the plasma wavelength at this density ($\sim$ 3 mm). Thus, the on-axis wakefield in the drive beam is dominated by the linear plasma response outside the bubble, not the rarefied region. This is consistent with the simulated wakefield inside the drive, as it resembles a linear,single-mode response. Conversely, wakefields behind the drive are strongly dominated by the high density sheath collapsing back onto the axis, giving rise to the nonlinear response after the drive. We term this beam-plasma interaction as quasi-nonlinear, because it shows characteristics of both linear and nonlinear plasma wakefields. This change in the nature of the plasma response is beneficial to maximizing transformer ratios, as we can see by the difference in wakefield amplitude between the drive and witness regions.

CHAPTER 3

Longitudinal Shaping Using Emittance Exchange

3.1 Methods for Longitudinal Bunch Shaping

Precise control of the longitudinal current distribution inside an electron bunch has been a re-occurring challenge in accelerator physics. This stems from the fact that electron beam bunch lengths are generally on the scale of picoseconds long, much faster than any type of controllable mechanical or electronic process. Control of the bunch length out of a photocathode electron source is determined by the laser pulse length used to stimulate the electron emission from the cathode. Temporal duration of the laser pulse is often either compressed or expanded based on dispersive path differences, due to an introduced energy chirp in the laser pulse. A similar technique can be used to scale the bunch length of an electron beam using an RF cavity to introduce a longitudinal energy chirp in the beam and a chicane to create an energy dependent path length difference to compress the bunch. These techniques only serve to scale the overall length of the bunch whose precise shape is often poorly controlled.

An ideal technique for beam shaping would be able to shape the electron bunch at the picosecond scale, be able to create sharp features necessary to excite a high transformer ratio wakefield and work at high bunch charge (> 1 nC), with minimal bunch loss. For this specific experiment it is also desirable that the method is flexible enough too quickly investigate multiple bunch profiles and be tunable in-situ, as a response to changes in machine performance.

Motivated by increasing the transformer ratio of wakefield drive bunches, several techniques have been identified to finely control the current distribution inside an electron bunch, with a linearly ramped drive bunch as a central goal. The use of a dogleg chicane with sextupoles to create a linear ramp was investigated by J. England [33] at the Neptune Accelerator at UCLA. The use of a corrugated, dielectric wakefield structure to induce an energy chirp

in the beam paired with a chicane was used at BNL to create a linear ramp [34]. While these schemes are able to generate the required distribution, they lack tunability and flexibility in quickly altering the tailored profile.

More recently, a laser based method using pulse stacking to shape the temporal laser pulse shape was used in a similar PWFA wakefield experiment. This method split a single pulse into 12 micro pulses spaced equally on the temporal axis. Micro-pulse intensity can be independently controlled to create a linear ramp drive and witness laser pulse [35]. Another laser pulse shaping method is the use of a transverse mask in a dispersive section [67]. This acts to shape the beam in Fourier space which is then translated back into the real time axis through an inverse dispersive process. For low charge electron beams laser shaping methods are ideal because the laser pulse directly corresponds to the temporal beam profile without the need for extra beamline elements. However this method does not work for high current drive bunches, whose space charge forces at low energies in the photo-injector dissolve any sharp profile features.

A flexible longitudinal bunch shaping method at relativistic beam energies, where space charge forces are not dominant, is transverse to longitudinal emittance exchange (EEX). First purposed as a way of improving control over beam quality for FEL applications [68], the emittance exchange beamline takes the horizontal and longitudinal phase spaces and exchanges them while leaving the vertical phase space to evolve as a drift. The application to longitudinal beam shaping was realized by placing a transverse mask in the beamline to shape the horizontal beam projection prior to EEX [37]. Through emittance exchange this projection is mapped onto the temporal profile of the beam.

In this chapter will discuss the first order process by which this exchange happens in detail. Then we discuss effects of higher order terms and collective forces on the final temporal beam shape. Finally, we will consider how this allows precise shaping of the longitudinal current profile and show optimization with simulations.

3.2 Emittance exchange

The EEX beamline (Fig. 3.1) consists of two dispersive doglegs separated by a transverse deflecting cavity. We consider a single particle with the initial coordinate x_i in transverse

and longitudinal phase space

$$x_i = \begin{pmatrix} x_i \\ x_i' \\ z_i \\ \delta_i \end{pmatrix} \tag{3.1}$$

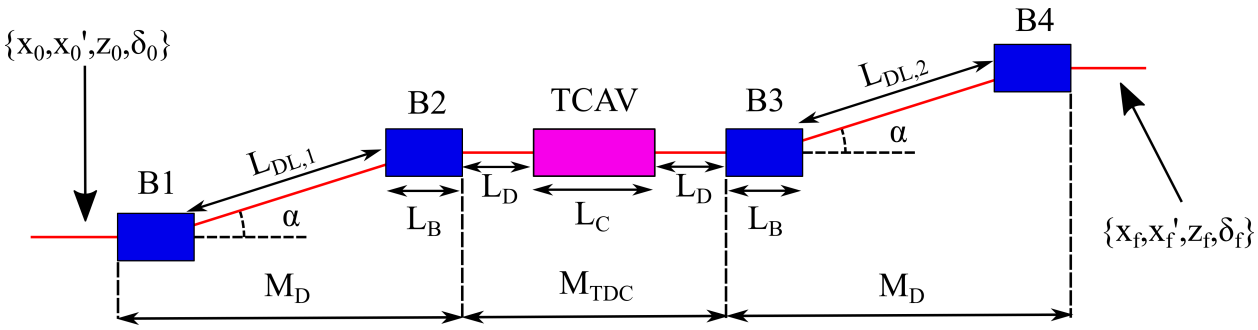

Figure 3.1: Emittance exchange layout.

We consider only the horizontal and longitudinal coordinates as the beam evolves in the vertical direction according to a simple drift and does not take part in the shaping process. This will become relevant later, as it becomes important for propagating the longitudinal profile after the EEX beamline.

The single particle evolution through the EEX beamline is given by the 4x4 transport matrix, given by

$$M_{EEX} = M_D M_{TDC} M_D \tag{3.2}$$

where M_D, M_{TDC} are the linear 4x4 transport matrices of the dogleg and transverse deflecting cavity respectively. Each dogleg consists of two rectangular bends with a length L_b and a bend angle of α, separated by a drift D. The transport matrix for a single dogleg is thus

given by

$$M_D = \begin{bmatrix} 1 & L & 0 & \eta \\ 0 & 1 & 0 & 0 \\ 0 & \eta & 1 & \xi \\ 0 & 0 & 0 & 1 \end{bmatrix} \tag{3.3a}$$

$$L = \frac{2\cos(\alpha)L_B + L_{DL}}{\cos^2(\alpha)} \tag{3.3b}$$

$$\eta = \frac{L_{DL} + 2\cos(\alpha)L_B - \cos^2\alpha(2L_B + L_{DL})}{\sin(\alpha)\cos^2(\alpha)} \tag{3.3c}$$

$$\xi = \frac{2\cos(\alpha)\sin(\alpha)L_B + \sin^3(\alpha)L_{DL} - 2L_B\alpha\cos^2(\alpha)}{\sin(\alpha)\cos^2(\alpha)} \tag{3.3d}$$

where L is seen as the drift length through the dogleg, η is the longitudinal dispersion in the dogleg and ξ is the momentum compaction factor.

The transverse deflecting cavity (TDC) that separates the two doglegs is a three cell pillbox style cavity that uses the TM_{110} mode to apply a longitudinally-dependent transverse kick to the beam. The E and B fields near the symmetry axis of the cavity are given by [69]

$$E_x = E_0\frac{k}{4}(a^2 + x^2 - y^2)\sin(kz)\cos(\omega t) \tag{3.4a}$$

$$E_y = E_0\frac{k}{2}xy\sin(kz)\cos(\omega t) \tag{3.4b}$$

$$E_z = E_0 x\cos(kz)\cos(\omega t) \tag{3.4c}$$

$$cB_x = E_0\frac{k}{2}x\cos(kz)\sin(\omega t) \tag{3.4d}$$

$$cB_y = E_0\frac{1}{k}\Big(\frac{(ka)^2}{4} - 1 + \frac{k^2(x^2 - y^2)}{4}\Big)\cos(kz)\sin(\omega t) \tag{3.4e}$$

$$cB_z = -E_0 y\sin(kz)\sin(\omega t) \tag{3.4f}$$

where a is the scale radius of the cavity E_0 is the peak electric field and ω,k are the angular frequency and wavenumber of the TM_{110} mode. For this we can clearly see that for particles completely on-axis (x=y=0) they will experience a deflection from the E_x and B_y fields which are completely out of phase from on another. If we assume that the bunch arrives at the cavity center z = 0 at t = 0 then the magnetic field component goes to zero. Furthermore, if we assume that the bunch is short relative to the cavity wavelength, ie. $k\sigma_z << 1$ then

the transverse kick from the cavity is given as

$$E_x(z) = E_0 \frac{(ka)^2}{4} z \tag{3.5}$$

This creates a correlation between the longitudinal position and transverse momentum of the beam. Further calculation of the fields' effect on the beam yields the 4x4 transport matrix for a single particle, given by

$$M_{TDC} = \begin{bmatrix} 1 & L_C & \kappa L_C/2 & 0 \\ 0 & 1 & \kappa & 0 \\ 0 & 0 & 1 & 0 \\ \kappa & \kappa L_C/2 & \kappa^2 L_C/4 & 1 \end{bmatrix} \tag{3.6}$$

where the geometric kick strength is $\kappa = (eV/pc)(2\pi/\lambda)$ (pc is the mean momentum, V is the deflecting voltage and λ is the wavelength of the cavity) and L_C is the cavity length. For our first order calculation we use the thin lens approximation of M_{TDC} by setting $L_C = 0$.

We can now calculate the full 4x4 matrix for the emittance exchange beamline. The full matrix is given by

$$M_{EEX} = \begin{bmatrix} 1+\kappa\eta & 2L(1+\kappa\eta) & \kappa(L+L_D) & \eta+\kappa\xi(L+L_D) \\ 0 & 1+\kappa\eta & \kappa & \kappa\xi \\ \kappa\xi & \eta+\kappa\xi(L+L_D) & 0 & 2\xi(1+\kappa\eta) \\ \kappa & \kappa(L+L_D) & 0 & (1+\kappa\eta) \end{bmatrix} \tag{3.7}$$

where L_D is the drift length between the dogleg and deflecting cavity. If we apply what is known as the "emittance condition" ie. $1 + \kappa\eta = 0$ then the matrix reduces to

$$M_{EEX} = \begin{bmatrix} 0 & 0 & \kappa(L+L_D) & \eta+\kappa\xi(L+L_D) \\ 0 & 0 & \kappa & \kappa\xi \\ \kappa\xi & \eta+\kappa\xi(L+L_D) & 0 & 0 \\ \kappa & \kappa(L+L_D) & 0 & 0 \end{bmatrix} \tag{3.8}$$

From this matrix we can see the process of emittance exchange. As the block matrix has no nonzero diagonal components, the final beam phase space in the z direction only depends on the initial phase space in the x direction and vice versa. If we apply this matrix to the initial particle position we get the final location in the z direction given by

$$z_f = \{\kappa\xi + S_i(\eta + \kappa\xi(L + L_D))\}x_i \tag{3.9}$$

where $S_i = x_i'/x_i$ is the position-momentum correlation in the transverse plane. Thus, the final z position has an explicit dependence on the initial horizontal coordinate of the particle. Given a perfectly collimated beam ($S_i = 0$), z_f is only dependent on x_i.

3.2.1 Conceptual Understanding of Emittance Exchange

It is worthwhile to understand what mechanisms take part in the emittance exchange process, specifically those that are not immediately evident from Eqn. 3.8. In order to do this we will examine the momentum and position separately, as the emittance exchange beamline can be split into separate parts respectively. We follow the conceptual explanation from Ha. et. al. [70].

We first examine the momentum exchange, which happens in the first half of the beamline. We consider the 4x4 single particle transport for the first dogleg to the end of the transverse deflecting cavity. Using equations for a single dogleg Eqn. 3.3 and transverse deflecting cavity Eqn. 3.6 with the thin lens approximation ($L_C = 0$) we see that the transport matrix for these elements are as follows:

$$M_{PEX} = \begin{bmatrix} 1 & L + L_D & 0 & \eta \\ 0 & 1 + \kappa\eta & \kappa & \kappa\xi \\ 0 & \eta & 1 & \xi \\ \kappa & \kappa(L + L_D) & 0 & 1 + \kappa\eta \end{bmatrix} \tag{3.10}$$

Assuming the same single particle coordinates as before, $x_i = (x_i, x_i', z_i, \delta_i)^T$ the momentum coordinates, x_2', δ_2 at the end of this EEX beamline section are

$$x_2' = (1 + \kappa\eta)x_i' + \kappa z_i + \kappa\xi\delta_i \tag{3.11a}$$

$$\delta_2 = \kappa x_i + \kappa(L + L_D)x_i' + (1 + \kappa\eta)z_i \tag{3.11b}$$

If we take a close look at the first two terms in the equation for x_2' we see $x'i$, which is simply the initial transverse momentum and $\kappa\eta x_i'$ which is a result of the dogleg and TDC. For particles with a nonzero initial transverse momentum, the dogleg creates a path length difference relative to the reference particle (see Eqn. 3.3) which causes it to arrive late in the TDC. This results in a transverse kick in the deflecting cavity giving rise to the term $\kappa\eta x_i'$. If we tune the deflecting cavity kick strength such that $\kappa = -1/\eta$ we can cause this kick to cancel out the initial transverse momentum. Thus, the final momentum is only a

function of (z_i, δ_i) and has been "exchanged". Similar logic is used to interpret the terms in the equation for δ_2. It should be noted that the particle still needs to traverse through the second dogleg but the remaining beamline elements have no first order effects on particle momentum x_2', δ_2.

We now examine the position exchange which is said to happen in the second half of the EEX beamline from the TDC to the second dogleg end. We again calculate the 4x4 transport matrix for this beamline

$$M_{EEX} = \begin{bmatrix} 1+\kappa\eta & L+L_D & \kappa(L+L_D) & \eta \\ 0 & 1 & \kappa & 0 \\ \kappa\xi & \eta & 1+\kappa\eta & \xi \\ \kappa & 0 & 0 & 1 \end{bmatrix} \tag{3.12}$$

And again assuming the same form for single particle coordinates at the beginning of this section (x_1) we get equations for the final position coordinates as

$$x_f = (1+\kappa\eta)x_1 + \kappa(L+L_D)z_1 + \eta\delta_1 + (L+L_D)x_1' \tag{3.13a}$$

$$z_f = \kappa\xi x_1 + \eta x_1' + (1+\kappa\eta)z_1 + \xi\delta_i \tag{3.13b}$$

If we tune the beamline to meet the same condition as before ($\kappa = -1/\eta$) we can see removal of the x_1, z_1 terms from the final coordinate equations. The TDC applies an x-dependent longitudinal kick, which then creates a change in the final transverse position due to dispersion in the dogleg, canceling any initial transverse offset in the TDC. Note that while the finial positions in x,z have a dependence on x', δ we can still claim that position exchange has happened, due to the removal of initial position dependent terms.

3.2.2 Suppressing Second Order and Collective Effects

The picture of emittance exchange beam shaping presented here is an optimistic one. For a perfect translation of horizontal beam projection to longitudinal current, the divergence of all beam particles must be exactly proportional to their horizontal offset such that S_i is a constant. This corresponds to a zero emittance beam, which is of course not practicably realizable. Since the beam particle divergence has some rms spread, the resulting beam current profile will be smoothed. However, at the Argonne Wakefield Accelerator the first

order emittance contribution to the profile was found to be negligible [70] due to the low emittance photoinjector.

We also considered the transverse deflecting cavity to be zero length (thin lens approximation). We also neglected collective beam effects, such as coherent synchrotron radiation (CSR), which is especially prevalent due to the number of bends in the EEX beamline. These realities in practice negatively affect the quality of our linear ramp, which results in a corresponding drop in transformer ratio. This can be corrected through the use of second order sextapole magnets, but these were not included in the current iteration of the EEX beamline at AWA. However, a procedure called the "slope-control" method was developed to correct for these second order terms [70]. This method involves changing the horizontal phase space "slope" or the central x-x' correlation such that it minimizes changes to the idealized profile. To mitigate collective effects, it was found that the use of an asymmetric EEX beamline such that each dogleg has a different momentum compaction factor was effective. Further experiments suppressing CSR is planned by installing variable gap metallic plates in the dipoles [71].

3.2.3 Applying EEX to Longitudinal Bunch Shaping

We can now apply this first order theory to creating longitudinally shaped bunches. As we have seen, particles after the EEX beamline have a longitudinal position dependent on the initial transverse location. This can be extended to a full bunch distribution as follows

$$\lambda_{zf}(z_f) = A\lambda_{xi}(x_i) \tag{3.14}$$

where $\lambda_{zf}, \lambda_{xi}$ are the linear beam densities in the longitudinal and transverse direction respectively and A is a scaling coefficient. From this our goal is clear, shape the transverse projection of the beam distribution into the desired form of the final current distribution.

The most straightforward method of doing this is by using a transverse mask to scatter undesired particles. We will calculate the mask profile by backtracking from a given longitudinal current distribution λ_{zf} and assume the transverse beam profile before the mask as a 2D Gaussian

$$\rho(x,y) = \frac{1}{2\pi\sigma_x\sigma_y}\exp\left(-\frac{x^2}{2\sigma_x^2}-\frac{y^2}{2\sigma_y^2}\right) \tag{3.15}$$

We will simply multiply this distribution to a masking function given by

$$f(x,y) = \begin{cases} 1 & -v(x) \leq y < v(x) \\ 0 & \text{otherwise} \end{cases} \tag{3.16}$$

where $v(x)$ is an equation that defines the mask profile across the entire mask. The final transverse projection then is given by

$$\lambda_{xi}(x) = \int_{-y_{max}}^{y_{max}} \rho(x,y) f(x,y) dy \tag{3.17}$$

Inserting the masking function into this yields

$$\lambda_{xi}(x) = \int_{-v(x)}^{v(x)} \rho(x,y) dy \tag{3.18}$$

and adding in our 2D Gaussian and considering the vertical symmetry of the distribution gives

$$\lambda_{xi}(x) = \frac{1}{\pi \sigma_x \sigma_y} \exp\Big(-\frac{x^2}{2\sigma_x^2}\Big) \int_0^{v(x)} \exp\Big(-\frac{y^2}{2\sigma_y^2}\Big) dy \tag{3.19}$$

Inverting this function to solve for $v(x)$ results in

$$v(x) = \sqrt{2}\sigma_y \text{erfinv}\Big[-\sigma_x \lambda_{xi}(x) \exp\Big(\frac{x^2}{2\sigma_x}\Big)\Big] \tag{3.20}$$

We desire a linearly ramped drive to create the drive and a long witness to sample the resulting wakefield so our desired transverse profile has the following form

$$\lambda_{xi}(x) = \begin{cases} ax + a(l_d + l_g/2) & -l_d - l_g/2 \leq x < -l_g/2 \\ 0 & -l_g/2 \leq x < l_g/2 \\ b & l_g/2 \leq x < l_g/2 + l_d \\ 0 & \text{otherwise} \end{cases} \tag{3.21}$$

where l_d is the length of the drive/witness, l_g is the gap length between the drive and witness bunches, a is the slope of the drive ramp and b is the linear charge density of the witness. This mask shape can be quite complex and requires careful tuning of beam size and location on the mask in order to successfully create the correct final profile.

An easier method, shown to be effective in shaping the bunch into a variety of profiles [72], was to create a uniform transverse beam distribution before the mask. In this case the mask shape is trivial as it is just a scaled version of the desired current profile. The only

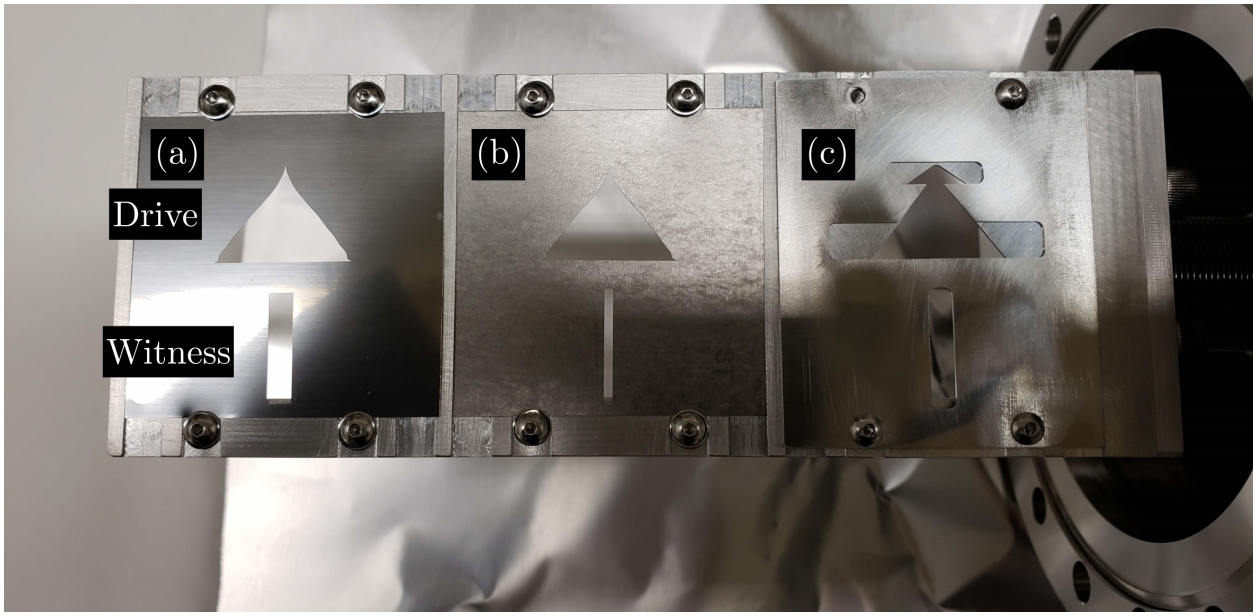

Figure 3.2: Masking mechanism inserted before the EEX beamline. The vacuum actuator contains three selectable masks (a) Single triangle drive with large witness, (b) Single triangle drive with small witness (c) Double triangle drive with large witness.

consideration that remains is making sure the beam size overlaps the cut out mask profile appropriately. A uniform beam was created by making a uniform laser distribution on the cathode, using a micro-lens array [43].

Ideally, the mask would be as thin as possible to scatter particles as a function of position only (thicker masks scatter particles as a function of position and divergence) while still being able to successfully scatter unwanted particles. Normally, tungsten masks are used due to their high density but it was observed experimentally that stainless steel masks were also viable. The EEX beamline has a small enough phase space acceptance that particles only need to be scattered a small amount to not make it through the EEX beamline.

Masks developed using these considerations are shown in Figure 3.2. The masks were fabricated from 2 x 2 inch tungsten/stainless steel plates which were laser cut and mounded on a 1D vacuum actuator. This allowed them to be exchanged *in-situ* which enabled rapid testing of different profiles. Each drive beam triangle was designed such that the beam out of EEX was two wavelengths long for a 110 Ghz wakefield structure. The double-triangle mask added a quarter wavelength smaller triangle to the drive head using a second, overlapped mask (laser cutting was not available for this mask) to ensure sharp corners in

the distribution.

Transverse beam distributions after masking for masks (a) and (c) are seen in Figure 3.3. We see that the beam does have some variation in transverse density on the order of 10-20%. Despite this the horizontal projection of the beam distribution is close to ideal. A slight curve in the beam head (-x direction) attempts to correct for higher order terms, resulting in a closer to ideal current ramp after EEX. We also see that when using mask (c) we are able to create a second small triangle at the beam head.

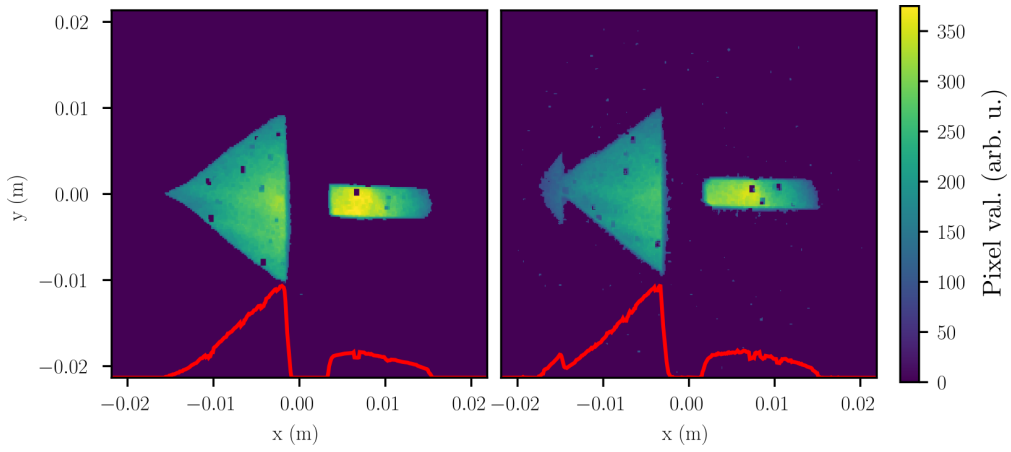

Figure 3.3: Measured transverse beam distributions after masking using masks (a)(left) and (c)(right) from Figure 3.2. Normalized horizontal beam projection is shown in red.

3.3 Drive and EEX Beamline Optimization

We begin with optimization of parameters of the beamlines already constructed at the AWA facility. Parameters inside of the EEX beamline are already set to establish the emittance exchange condition $1 + \kappa\eta = 0$ so they are not able to be changed. The drive beamline does have a number of variables to choose, as seen in Fig. 3.4. Our goal is to produce the ideal longitudinal beam profile with minimum transverse emittance and low energy spread at the end of EEX. The latter two goals become important for focusing into the plasma source as a small spot size is critical for the beam to interact properly with the plasma. Both emittance growth and energy spread increases the minimum spot size achievable due to the betatron envelope of the beam and chromatic aberrations.

Careful choice of simulation code is necessary as the beams are subject to collective

effects including space charge forces at low energy near the gun and coherent synchrotron radiation forces from strong bending angles in the EEX beamline. The Laminarity parameter ρ determines the dominance of thermal (emittance based) beam envelope evolution over space charge (electron to electron repulsive forces) dominated evolution [73]. This parameter is given as

$$\rho = \frac{I}{2I_A\gamma}\frac{\sigma^2}{\epsilon_n^2} \tag{3.22}$$

where I is the beam current, $I_A = 17$ kA is the Alfve'n current and γ is the relativistic parameter. For $\rho < 1$ the beam is emittance dominated, particle trajectories do not cross and the beam behaves like a laminar fluid. As $\rho \approx 1$ space charge forces become dominant. For the AWA gun these parameters are 12 nC in 6 ps or $I = 2.0$ kA, spot size on the cathode is $4\sigma = 10$ mm, and transverse emittance is 100 mm.mrad. In this case $\rho \approx 1$ for an energy of about 19 MeV; before reaching this energy the beam is space charge dominated, roughly the first half of the drive line.

To gain a sense of the effects of coherent synchrotron radiation we can calculate the power lost to radiation in one EEX bend. The power lost is given by [16]

$$\Delta P_{coh} \approx \frac{Q^2 c}{\epsilon_0 \rho^{2/3}\sigma_t^{4/3}}. \tag{3.23}$$

where Q is the total beam charge, ρ is the bend radius and σ_t is the temporal bunch length. This induces an average momentum loss and spread in the bunch that is independent of the beam energy for relativistic beams. Since this energy loss takes place in a dispersive region, it results in a modification to the beam phase space in the bend plane, which in turn increases emittance in that direction [74]. This effect is the dominant cause of large horizontal emittance after EEX, due to high bunch charge and strong bending angle.

The code OPAL [75] was chosen to model the drive and EEX sections of the beamline as it is able to model space charge and CSR effects. It also has an advantage of having a built-in genetic optimizer which is ideal for optimizing a large number of variables (as seen in Fig. 3.4) and offers flexibility in evaluating complex fitness functions.

Beamline parameters for the emittance exchange beamline, which remain fixed, are given in Table 3.1. The genetic optimizer was used to tune the drive beamline parameters to minimize the beam's transverse emittance, energy spread and particle loss coming out of the EEX beamline. Results from the optimization are seen in Figure 3.5. The optimized

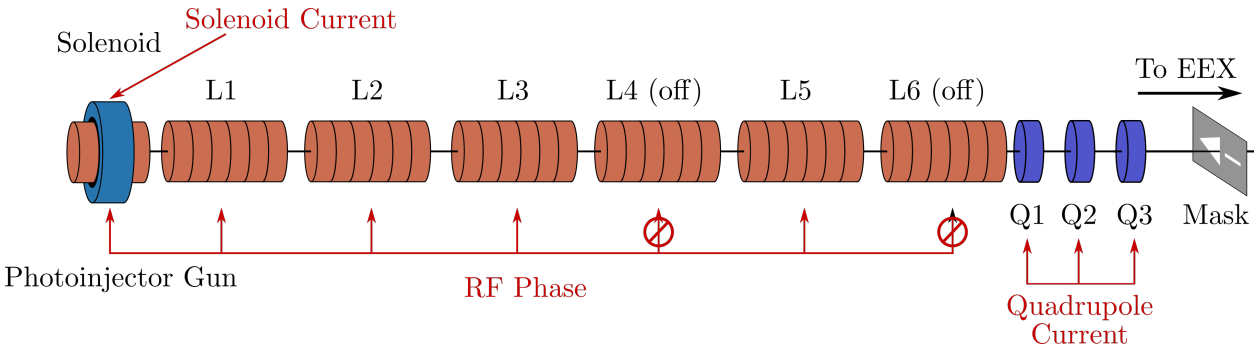

Figure 3.4: Major components of the drive beamline with optimization variables available (red).

Beamline parameter	Value	Unit
$\alpha_{1,2}$	20.0	Degree
L_B	0.31	m
L_D	2	m
L_C	0.48	m
$L_{D1,D2}$	0.5	m

Table 3.1: Design parameters for EEX beamline at AWA.

solution maximized transmission through the transverse mask used for shaping, by choosing the gun solenoid focusing strength. Energy spread and emittance growth are minimized by choosing an off-crest linac phase. The quadrupole are set such that the minimum vertical spot size inside the EEX beamline is at the deflecting cavity, thus minimizing energy spread due to a longitudinal kick for off-axis particles in the vertical direction. We also see a partial emittance exchange where the final transverse emittance approximates the initial longitudinal emittance. Incomplete exchange is due to CSR in the bends.

To verify the validity of our simulation results we conducted a quadrupole scan in a triplet arrangement and measured the energy spread after the emittance exchange beamline. The focusing strength of quadrupoles 1 and 3 were set to be equal and quadrupole 2 was set to negative two times the focusing strength of Q1. The strength was then scanned for Q1 while maintaining the same ratio for the others. Energy spread was measured in a spectrometer positioned after the EEX by subtracting the rms beam size with the spectrometer on/off and then subtracting the rms off beam size from the on beam size in quadrature. The beam

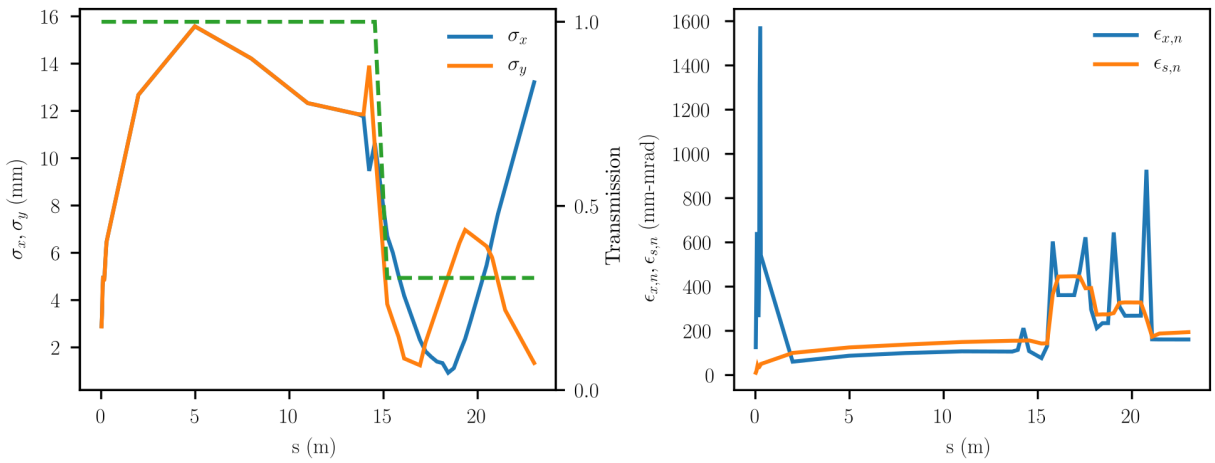

Figure 3.5: Simulated transverse beam properties as it propagates through the optimized AWA beamline up to the end of EEX. Left: Plot of the transverse size and beam transmission (dotted line) of the beam through the drive beamline and EEX. Masking is located at s = 15 m. Right: Plot of transverse and longitudinal normalized beam emittance.

size near the transverse deflecting cavity in the EEX beamline was also measured for each quadrupole setting. Results from this scan are seen in Figure 3.6. We clearly see a direct correlation between energy spread and beam size in the deflecting cavity.

After optimization we also compared transverse distributions of the measured beam after EEX with results from simulation, as seen in Figure 3.7. The measured beam shows moderate agreement with simulation results. We note that the beam projection in the vertical direction should remain constant throughout EEX. In both cases we clearly see a contribution from the witness bunch, which has a sharp cutoff in the y-direction due to its rectangular shape and is roughly uniform in density. The horizontal beam profile, which changes substantially due to the exchange, is fairly consistent in size and geometry between simulation and measurement. This beam distribution is used as the input for plasma beamline simulations, discussed in Chapter 5.

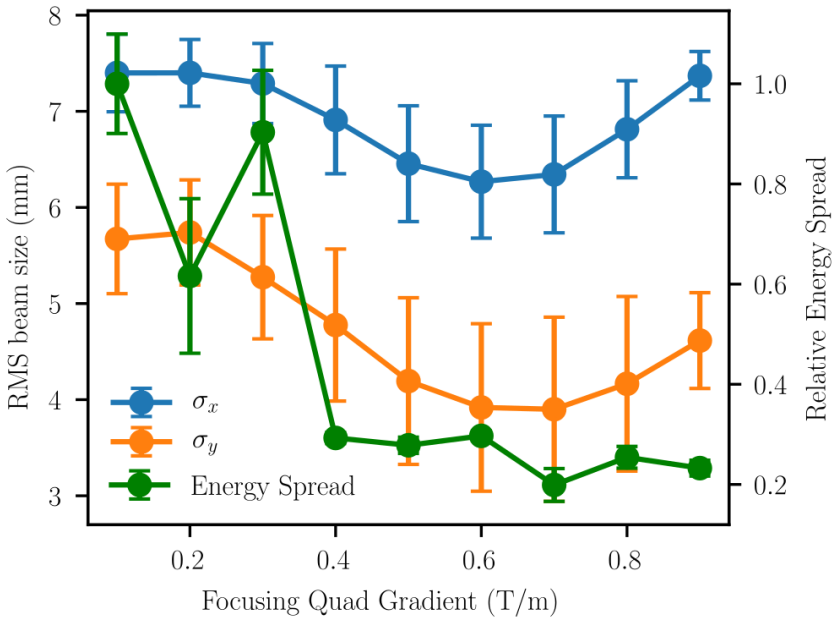

Figure 3.6: Measured beam size near the transverse deflecting cavity in EEX plotted and a measurement of the rms energy spread of the beam after EEX plotted as a function of quadrupole triplet strength.

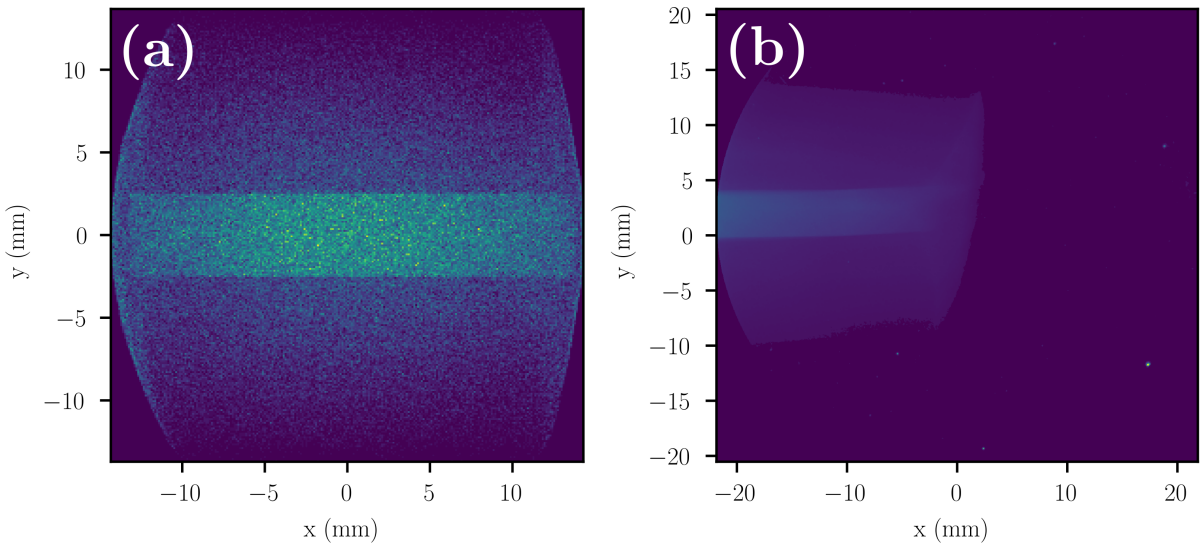

Figure 3.7: Transverse beam profiles out of EEX from simulation (a) and YAG screen measurements (b).

CHAPTER 4

Hollow Cathode Arc Plasma Source

In this chapter we will focus on the plasma source for the experiment. Our goal is to create a uniform plasma column of a density that closely matches achievable beam parameters from the emittance exchange beamline at the Argonne Wakefield Accelerator. It is also necessary to have the ability to tune the plasma density *in-situ* in order to characterize the effect of different plasma densities on similar electron beam profiles.

There are several different types of plasma sources used today for both LWFA and PWFA experiments. These sources generally fall into three categories, laser beam, electron beam and discharge ionization sources. All start with a choice of neutral gas in a vacuum chamber at pressures anywhere between mTorr and several atmospheres (760 Torr). The resulting plasma density depends on the gas pressure and the ionization fraction of the gas

$$n_0[\mathrm{m}^{-3}] = \frac{N_A}{22.4[\mathrm{L}]}\frac{p[\mathrm{Torr}]}{760[\mathrm{Torr}]}\eta \tag{4.1}$$

where N_A is Avagadro's Constant, p is the gas pressure and η is the ionization fraction. If we change this equation to convenient units we get

$$n_0[\mathrm{cm}^{-3}] = 3.52 \times 10^{16} p[\mathrm{Torr}]\eta. \tag{4.2}$$

We can see that plasma densities in wakefield experiments can range from $10^{13}-10^{19} cm^{-3}$. As discussed in Chapter 2 the plasma density dictates the overall scaling of the accelerating fields and the beam size. So it is important to match plasma characteristics to the injected beam to properly enhance the transformer ratio. To match the beam size we want the characteristic plasma frequency to be near 110 GHz. From the equation for plasma angular frequency $f_p[\mathrm{GHz}] = 8.9 \times 10^{-6}\sqrt{n_e[\mathrm{cm}^{-3}]}$ the plasma density should be roughly 1.5×10^{14} cm^{-3}.

As evident from their respective names, the different plasma source types differ in their method of neutral gas ionization. Laser ionization occurs when a powerful laser pulse is injected into the gas and the laser field magnitude is high enough to ionize the gas atoms. This

requires a TW class laser system in order to create the intensity necessary ($> 10^{12}$ W/cm^{-2}) in a large enough spot size ($\sim$ 1 mm) to accelerate a moderately sized beam [76] in a lithium vapor. Beam based ionization of neutral gases is similar to this method as a few nC beam can produce transverse electric fields that reach GV/m scales [77]. The downsides of these methods are that the laser/beam used to create the plasma can rarely be used for other purposes during an experiment, despite the amount of effort required to produce them. The advantage of these methods is that they allow complex and finely tailored plasma profiles [78], sometimes with multiple gas species in tandem [79].

Discharge methods by contrast offer a much simpler method of creating plasmas, while giving up precise control over the plasma density profile. A neutral gas is ionized via a capacitive discharge, powered by an external circuit. Its relatively simple ionization makes it ideal for experiments unconcerned with precise plasma distribution control, and as such is used in this experiment.

This chapter begins with a discussion of the relevant physics behind discharges with a particular focus on the requirements for formation. We will then apply this knowledge to our particular type of device, the hollow cathode arc plasma source. Finally we will conclude our source discussion with plasma measurement techniques and a characterization of the plasma used in this experiment. Part of the goals for this chapter is to have it serve as a reference guide for the plasma source used in this experiment, as useful references for the unique characteristics of this device are scarce.

4.1 Physics of Plasma Discharges

We start with an examination of the different plasma discharge regimes, as discussed in the helpful book "Fundamentals of gaseous ionization and plasma electronics" [1]. We consider a vacuum chamber containing neutral gas at a given pressure p. Inside the chamber there are two planar electrodes separated by a distance d and a voltage V is applied externally to the electrodes creating a uniform electric field $E_z = V/d$. The current that travels between the two electrodes for a given voltage is determined by a number of physical processes and is captured in Fig. 4.1. There are three main regimes, based on the observable phenomena in each. We start with the voltage below what is known as the breakdown voltage. In

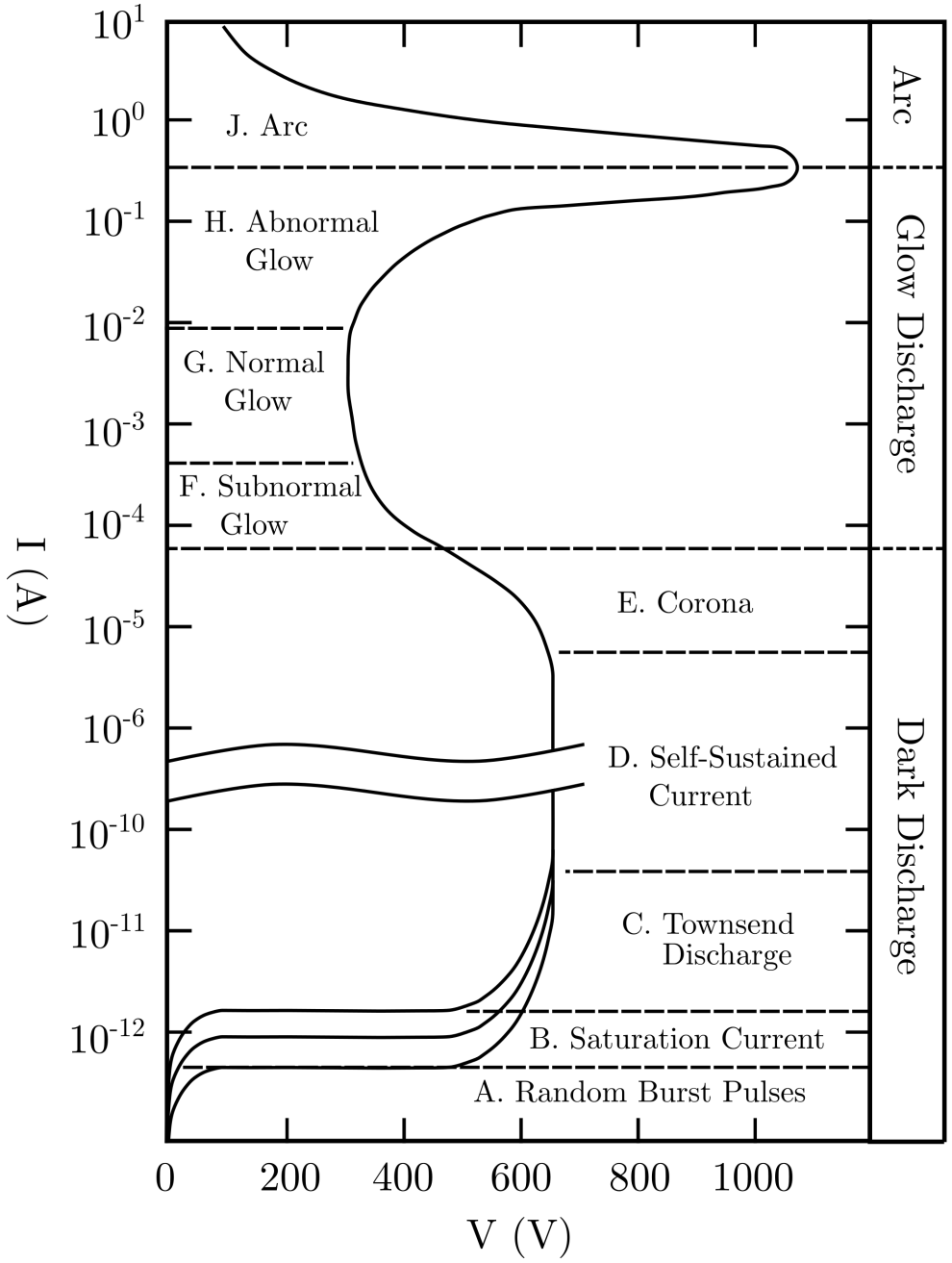

Figure 4.1: Typical voltage-current relation of a gaseous gap, for neon gas at 1 Torr with disk electrodes of 2 cm diameter and separation of 50 cm. Adapted from [1].

this regime, ions and electrons are created via random processes (external radiation such as photoemission or radioactivity) on the cathode and anode. These ions are accelerated by the electric field until they reach the opposing electrode. Current in this case is extremely low so nothing is visible to the eye, which is where this "dark" regime gets its name.

Once electrons are emitted from the cathode they travel towards the anode and have a chance of colliding with neutral gas molecules in the inter-electrode space. Average distance particles travel between collisions, or the mean-free path, is inversely proportional to the gas density and determines the energy gain in-between collisions, due to the electric field. Eventually, accelerated electrons have enough kinetic energy to liberate one extra electron from collisions with subsequent gas particles. These liberated electrons are also accelerated by the electric field and can then go on to liberate more electrons from other gas particles in what is called a Townsend avalanche/discharge. This creates an exponential growth in current from the cathode to the anode.

Ionized gas particles from collisions with electrons are simultaneously accelerated towards the cathode. At a given voltage their impacts on the cathode release secondary electrons from the surface. Depending on the frequency of electron emission from these results in an over-exponential growth current and the discharge becomes self sustaining, as long as a minimum voltage known as the "sustaining voltage", which is lower than breakdown, is applied. The resulting current in this regime becomes dominated by the electrode geometry and neutral plasma density. At this point the current is high enough to make the plasma visible to the eye, hence referred to as the "glow regime". The breakdown voltage required for a given gas pressure ρ and inter-electrode distance d is found using Paschen's Law [80] given by

$$V_{BD} = \frac{Bpd}{\ln(Apd) - \ln(\ln(1 + 1/\gamma))} \tag{4.3}$$

where $A = \sigma/k_B T$ and $B = U_I \sigma/e k_B T$ are calculated from characteristics of the plasma discharge. The avalanche is characterized by electron-ion collisional cross section σ, the probability of an ion releasing a secondary electron from the cathode γ and the energy necessary to ionize a neutral particle U_I. These parameters account for the three processes that govern the discharge, 1) the mean free path of electrons inside the neutral gas, 2) the energy gained by particles traversing that path relative to the collisional ionization energy, 3) emission of electrons and ions from electrode surfaces. Typical values for air

at room temperature and stainless steel electrodes are $A = 1.5$ mTorr^{-1}m^{-1}, $B = 36$ V-mTorr^{-1}m^{-1} and $\gamma = 0.02$. A plot of the breakdown voltage as a function of pressure times electrode separation pd is seen in Fig. 4.2. As we can see, the breakdown voltage required is often several kV which creates a significant technical challenge for long discharges at high pressures. We also observe a minimum voltage for discharge is required regardless of pd which is dependent solely on the gas parameters. Finally, we see asymptotic behavior in the discharge voltage when $pd \to \log(1+1/\gamma)/A$ this limit corresponds to a lack of available gas particles to sustain the discharge current.

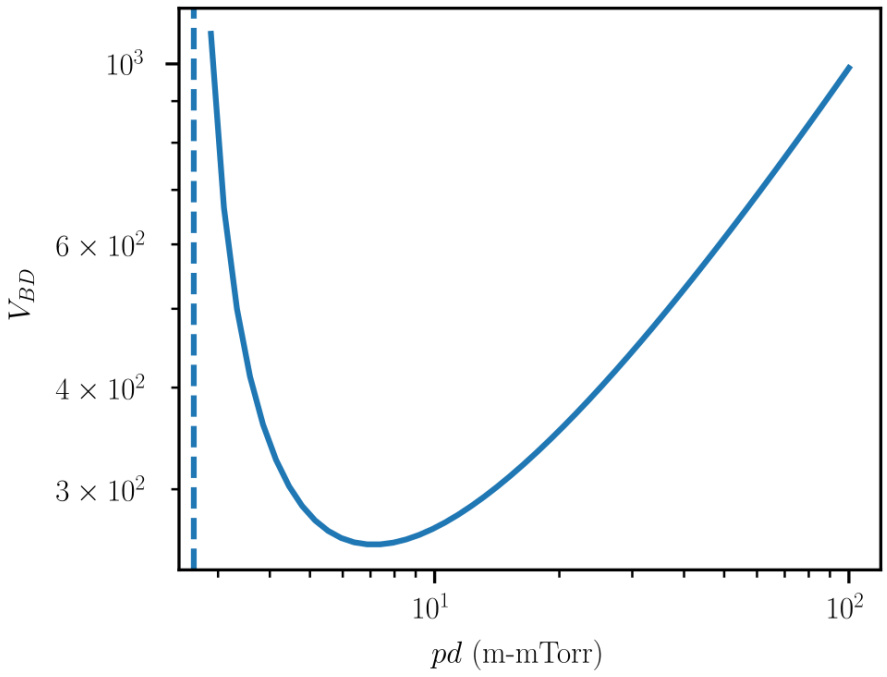

Figure 4.2: Plot of the minimum breakdown voltage as a function of pd for a discharge with $A = 1.5$ mTorr^{-1}m^{-1}, $B = 36$ V-mTorr^{-1}m^{-1} and $\gamma = 0.02$. Vertical dashed line shows limit of asymptotic behavior when $pd \to \log(1+1/\gamma)/A$.

If we establish the glow regime successfully, we can increase the voltage significantly beyond the sustaining level to reach the plasma arc regime. At this point ion bombardment of the cathode now heats the cathode surface. This results in two effects, it heats the surrounding neutral gas, allowing multiple liberated electrons per collision, and the heated cathode starts to emit electrons thermally. The thermal emission of electrons is described by Richardson's law [81]

$$J = A_G T^2 e^{-W/k_B T} \tag{4.4}$$

where $A_G = \lambda_R A_0$ or a constant $A_0 = 1.20173 \times 10^6$ $\mathrm{Am^{-2}K^{-2}}$ times a material specific correction λ_R. W is the material work function and T is the temperature. These two effects add a considerable number of free electrons to the inter-electrode space, significantly increasing the current and reducing the voltage needed to maintain the discharge. This regime is referred to as the arc, due to the extremely high plasma current, which is only limited by the external voltage circuit and electrode health. In most configurations plasma sources that operate in this regime are powered by two separate power supplies in tandem. A high voltage, low current starter is used to reach the arc regime and a low voltage, high power supply is used to sustain the plasma at a low voltage and allow current increase to desired levels.

4.2 The Hollow Cathode Arc Plasma Source

We now use these principals to investigate a specific subset of arc discharge plasma sources, known as the Hollow Cathode Arc (HCA) plasma sources. Progress on HCA development and fundamentals of operation was collected into a seminal paper by Delcroix and Trindade [3] and we reference their work here. These sources can be varied in geometry but have one thing in common, a cathode, into which the plasma region extends as seen in Figure 4.3. This assures a large area which the plasma strongly interacts with the cathode surface,

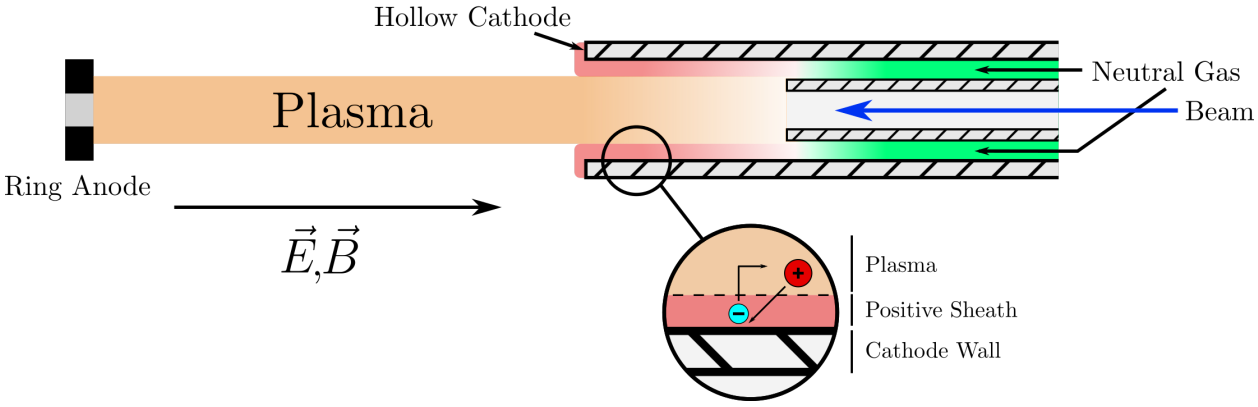

Figure 4.3: Basic structure of a hollow cathode arc plasma source showing ionized particle, neutral particle and plasma sheath regions.

which is the key to efficiently reaching the arc regime. It also increases the probability that emitted and liberated electrons collide with neutral particles before reaching the inter-

electrode space. Due to this, the resulting current from a hollow cathode is greater than a planer one. Work on hollow cathode arcs over a wide range of parameters such as electrode configuration, cathode materials, gas species and operational parameters found that an ideal the hollow cathode arc based source with a tantalum cathode and argon gas creates a pure plasma without contamination from cathode material, with a density of $10^{13} - 10^{14}$ cm^{-3} and is highly ionized (up to 95%) while maintaining a long cathode lifetime even at high currents (I $<$ 300 A) and high temperatures (T $<$ 2500 K).

We can separate operation of hollow cathode arc devices into several working regimes based on their pressure P, gas inlet flow rate Q and discharge current I as seen in Table 4.1. As is expected from its name, the normal regime has the optimal parameters for main-

Name	P	Q	I
Normal regime (N)	$<$ 0.1 Torr	$> 10^{-2}$ cm^3 STP	$>$ 10 A
Low gas-flow regime (LQ)	$<$ 0.1 Torr	$< 10^{-2}$ cm^3 STP	$>$ 10 A
Low current regime (LI)	$>$ 0.1 Torr	Indifferent	$>$ 10 A
High-pressure regime (HP)	$>$ 1 Torr	Indifferent	Indifferent

Table 4.1: Working regimes in a HCA plasma source. Adapted from [3].

taining discharge quality and cathode lifetime. In this regime the observed hot spot from ion bombardment is stretched over a large wall area as the plasma penetrates inside the cathode as supposed to smaller hot spots observed on planer cathodes. The requirement for gas pressure inside the hollow cathode is such that it allows for a high probability for wall-emitted electrons to collide with neutral particles and generate ions that heat the inner cathode wall. The hot spot location inside the hollow cathode can be controlled via the gas flow rate, as it decreases the plasma penetrates deeper into the cathode, thus pushing the hot spot due to ion bombardment deeper as well. This acts to raise the overall discharge voltage and accelerate the electrons more inside the cathode, where each emitted electron can undergo several ionizing collisions resulting in an increased discharge current.

The other regimes of HCA operation are to be avoided in order to successfully discharge the plasma and maintain long cathode lifetime. As we saw in the normal regime, if we decrease gas flow the discharge voltage rises. At some point the gas flow will be unable to maintain the pressure gradient required to sustain heating of a small region and sufficiently

higher voltages are required to achieve discharge. If on the other hand, if discharge current is too low then the ion bombardment is not sufficient to heat the cathode wall to create an internal positive column. In this case the hot spot is unstable, vaporization and damage to the cathode is expected due to instabilities. Finally, in the high pressure limit the hot spot becomes extremely localized regardless of the discharge current or location due to gas flow; damage of the cathode due to vaporization is also expected in this case.

The final parameter that effects plasma discharges is the application of an axial magnetic field. Charged particles in plasma generally have significant velocities associated with them. In the presence of a magnetic field they tend to spiral around magnetic field lines with the Larmour gyroradius of

$$r_g = \frac{mv}{|q|B}. \tag{4.5}$$

The radius decreases with magnetic field such that the charged particles can be confined to a localized region in a high magnetic field. For example, if a hollow cathode has a diameter of 1 cm and the plasma was created with a 150V discharge, the inter-electrode electrons would be confined to a column with the same radius using a magnetic field of 4 mT. This has been found to modify the discharge voltage required for a given current, dependent on the gas flow rate. The magnetic field can thus be used to increase or decrease the plasma confinement, which in turn allows easy modification of the plasma density during accelerator operations.

4.3 The UCLA Plasma Source

The specific hollow cathode arc plasma source used in this experiment has several differences from the previously described HCA design, but fundamentals of operation are the same. A partially cut out view of the UCLA plasma source is shown in Figure 4.4. Beams enter the plasma source from the top right, they travel through the hollow cathode (which is resistively heated by an external high current power supply) into the plasma region and then through a ring anode. Large solenoids outside the plasma chamber generate an on-axis magnetic field that acts to confine the plasma. In this section we discuss the design and operation of each subsystem in detail.

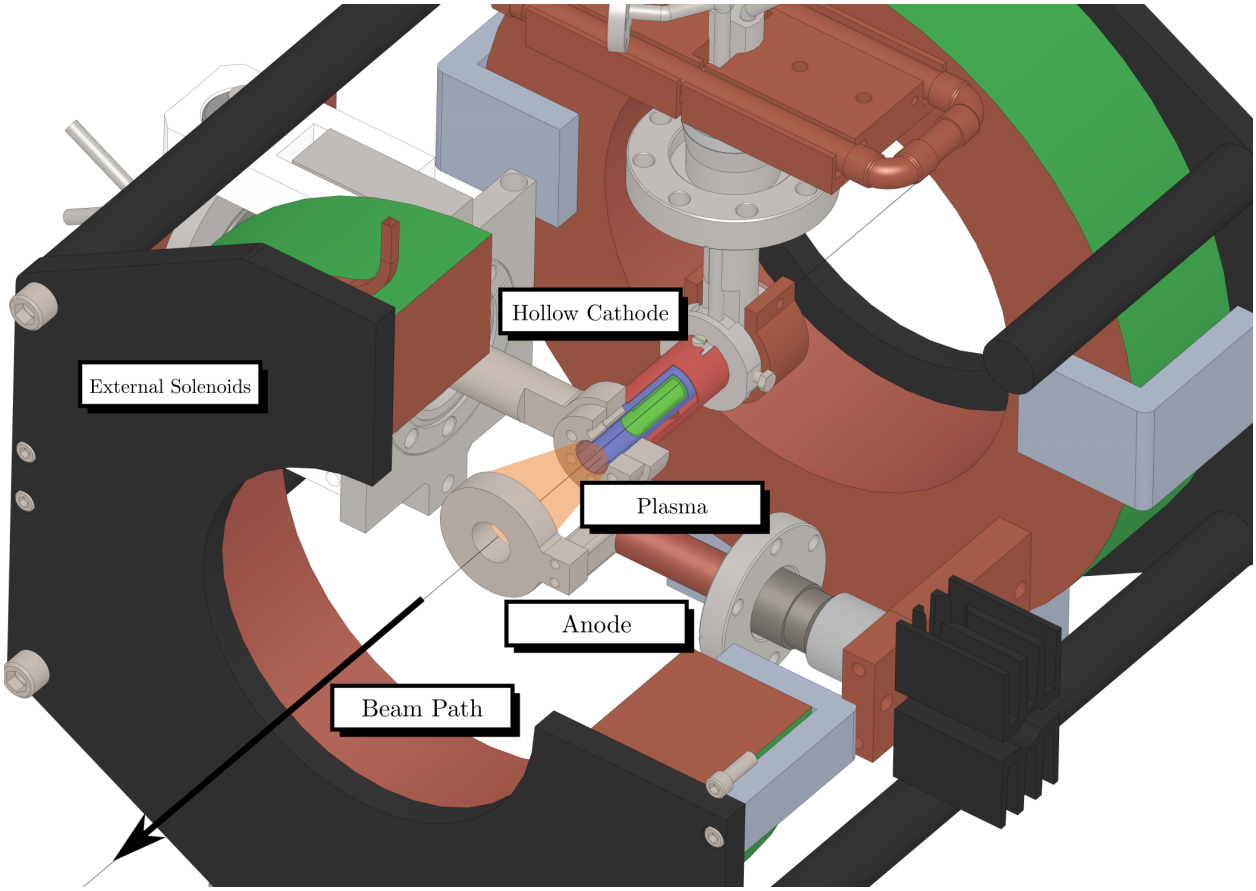

Figure 4.4: Partially cutout 3D image of the main components in the plasma source.

4.3.1 Mechanical Subsystem

The plasma discharge gap is formed by a simple ring anode and a hollow cathode which is comprised of three concentric tantalum tubes seen in Figure 4.5. Tantalum is the material of choice for the cathode surface due to its low conductivity, high temperature resistance, and historically good performance in previous hollow cathode arc experiments [3]. The central tube (colored blue in Figure 4.5) is supported on either side by two high current ($I < 1000$ A), low voltage ($V < 10$ V), water cooled electrical vacuum feedthroughs. Cathode arm A is welded to a set of small vacuum bellows and is attached to an external movement mechanism, which allows small changes in the front arm position *in-situ*. The ability to tune the tube location is necessary to accommodate any deformations in tube geometry due to repeated heating and cooling cycles. The other cathode arm is welded in place and can only be slightly rotated due to a rotatable flange. The tube is attached to the arms via compression on the flayed out portions on either end of the tube. It should be noted that this tube is the only electrical connection between the two cathode arms, a distinction that becomes important

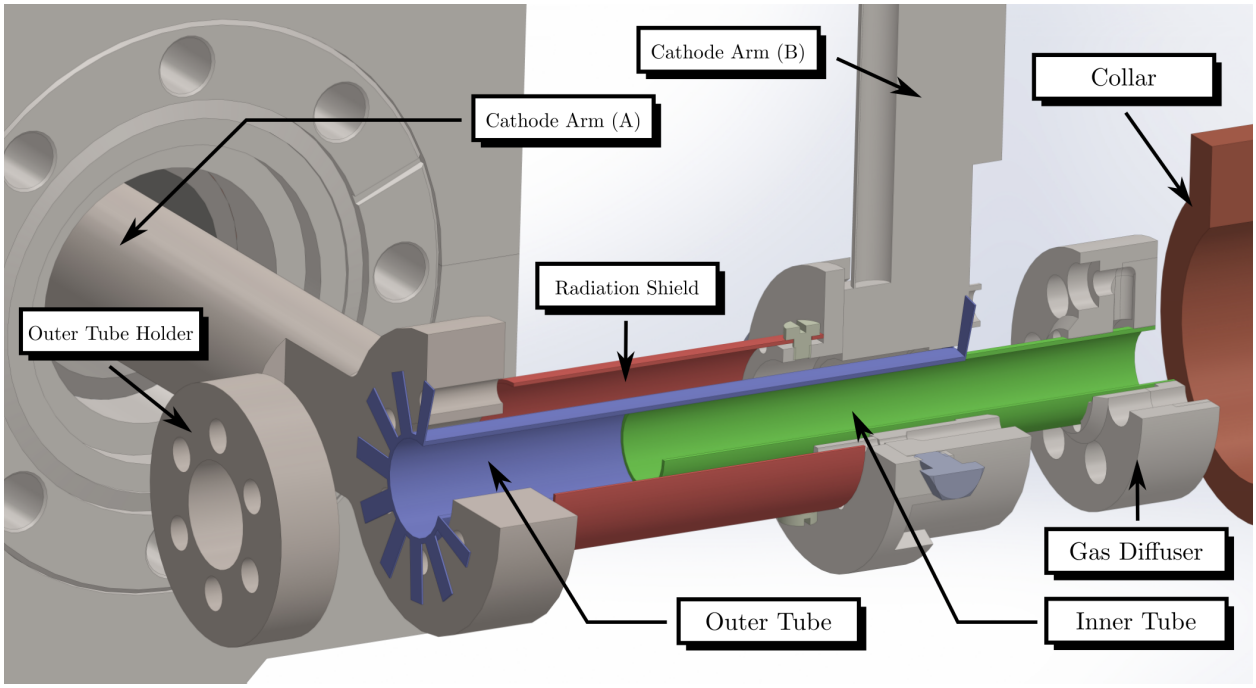

Figure 4.5: Partially exploded view of the hollow cathode assembly used in the UCLA plasma source.

when discussing the electrical subsystem.

The smallest tube (seen in green) is press fit into a gas diffuser mechanism (to be discussed in the next subsection) that is then attached to cathode arm B. It is secured in place with a number of long set screws which doubles as a holder for the central tube. A copper collar is then put in place around the cathode arm and gas diffuser to maintain alignment between the two pieces. This tube has a inside diameter of 11.4 mm which allows only a sub-mm gap in between the two central tubes. It is critical that these tubes are aligned properly [1] such that they do not come in contact with one another. It has been observed that these tubes can "weld" to each other if they come into contact, thus reducing overall external heating and prevents high current discharging.

The largest tube (seen in red) serves as a blackbody radiation shield. When the central tube is heated it gives off a significant amount of blackbody radiation. This is the main source of energy loss from the center tube which reduces the tube temperature, as conduction energy loss is limited towards the tube ends and convective losses are nonexistent in a vacuum. To reduce energy loss due to blackbody radiation the third tube is added to reflect this energy

[1] Experience says that the smallest tube axis should have a slight upward angle with the center tube axis, to take into account future droop due to heating.

back onto the central tube. It is important that this tube is long enough to reflect energy back onto the central tube but not come in contact with both cathode arms as to provide another path for heating current to travel along. In cases where contact does occur, this tube can deform, which leads to discharge problems.

4.3.2 Electrical Subsystem

The full electrical subsystem is shown in Figure 4.6. It consists of three main power systems, external heating, discharge, and solenoid.

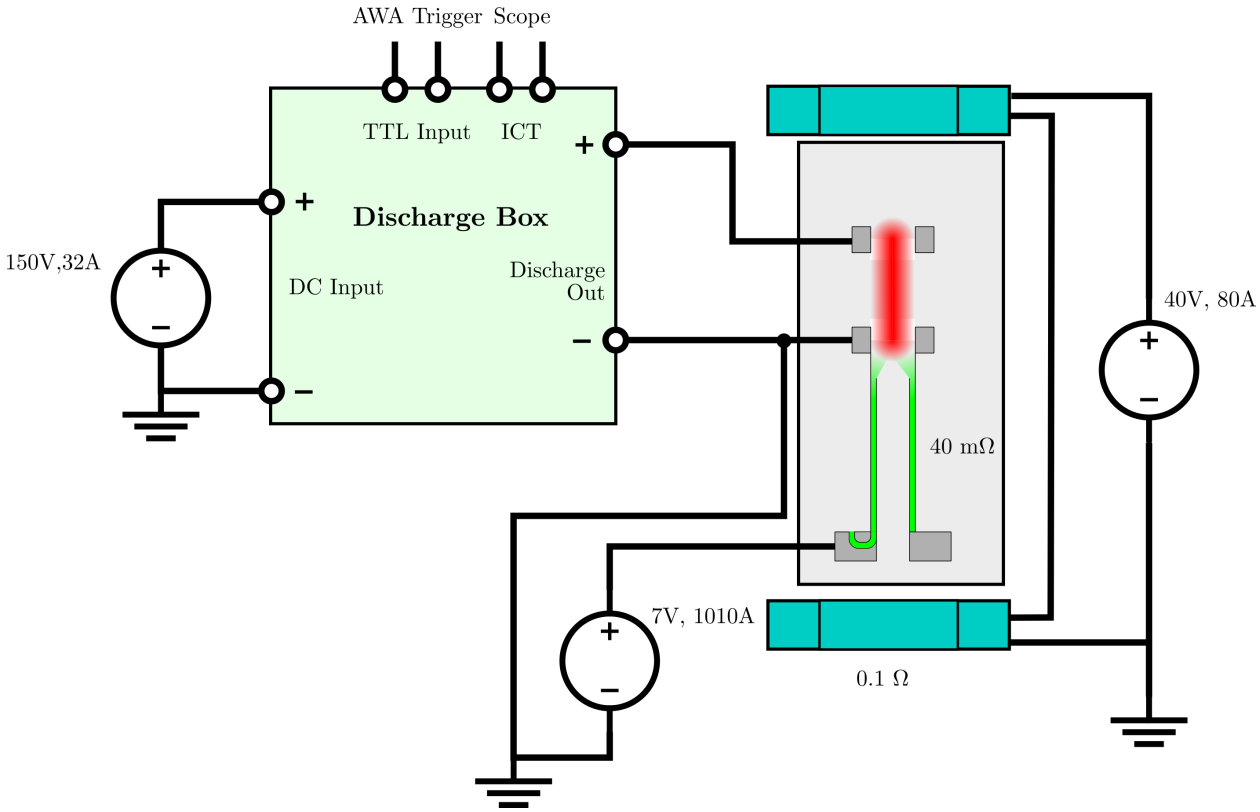

Figure 4.6: Schematic showing electrical systems of the UCLA Plasma Source

A unique feature of the UCLA plasma source is that the cathode tubes are heated externally prior to striking the discharge. As discussed in Section 4.1, the arc regime requires heating of the cathode surface and the nearby gas. Normally, this is achieved through ion bombardment when the electrode potential difference is on the order of 1 kV. To circumvent this limit, the tubes are resistively heated by an external power source supplying 1000 A seen in the electrical schematic in Fig. 4.6. Cathode arm (A) (as seen in Figure 4.5) is set to ground voltage as it will serve as the direct cathode for arcing, while Cathode arm (B)

can be raised up to 7 volts. Based on the measured potential difference and current across the tubes we can estimate the power delivered to the tubes. An optical pyrometer was used to measure the tube temperature as a function of power output from the supply as seen in Figure 4.7. It should be noted that monitoring the supply voltage is also a good way of monitoring cathode health as large deviations in resistivity outside of thermally dependent changes in resistance are a sign of damage.

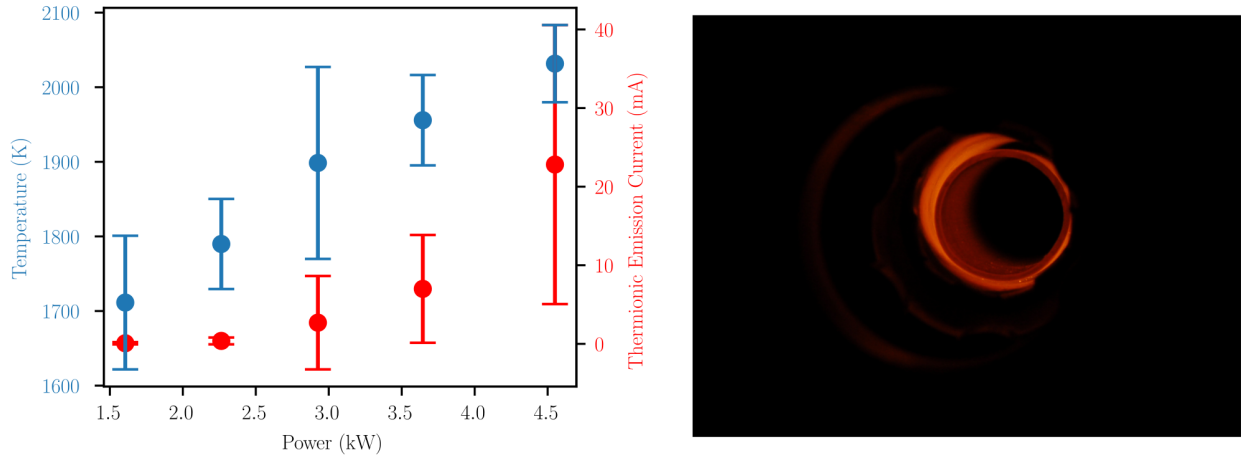

Figure 4.7: Left: Measurement of tube temperature and calculated thermionic current from Richardson's Law as a function of supply power. Right: Camera image of heated cathode at low power.

At a peak power output of ≈ 4.5 kW the tube temperature was roughly 2025 K while overall the temperature scaled linearly with supply power. From the camera image, we can clearly see that the innermost tube is heated significantly, despite it not receiving any direct electrical current. This is most likely due to radiation heating from the central cathode tube. Water cooling was used to maintain low temperatures in components exposed to the heater current of 1000 A. Water was pumped into a manifold which had separate hoses for each cathode arm, copper leads for high current wires and solenoids (discussed in Section 4.3.4). Nominal operational flow rate during plasma discharges was 4 gal/min. A collection of 4 0000 gauge wires (each rated for up to 300A) were used to connect the power supply to the plasma source.

Once the cathode is heated, the plasma is able to be discharge capacitively. As seen in Figure 4.8 a set of large capacitors with net capacitance of 48 mF was charged to 150V using

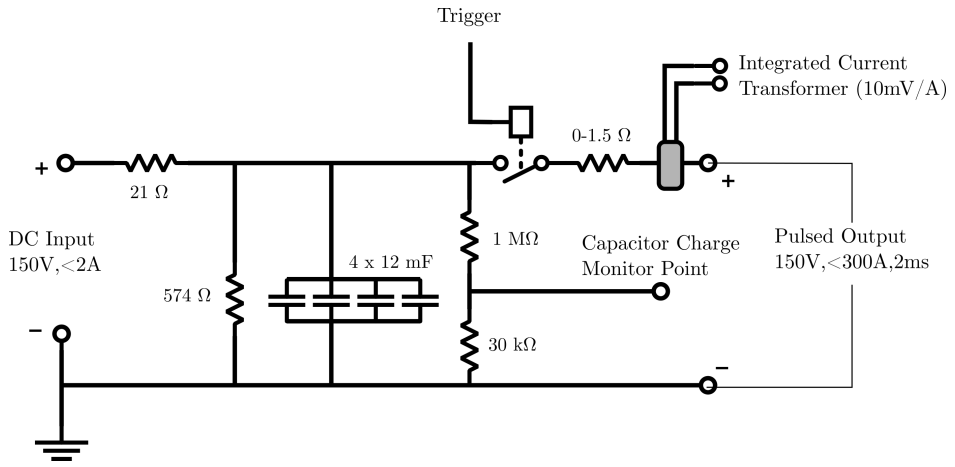

Figure 4.8: Schematic showing electrical circuit for plasma discharge box.

a DC power supply. A high power, solid state switch with an external trigger was used to discharge these capacitors across the plasma gap. As these capacitors store up to 0.5 kJ of energy when fully charged, a bleed resistor ($R = 574\ \Omega$) was connected in parallel to the capacitors to prevent charge build up when the plasma is not being discharged. Also in parallel with the capacitor bank was a pair of resistors to serve as a voltage divider (x 1/15) to safely monitor capacitor voltage.

The plasma discharge switch was triggered with a 200 μs, 5 V TTL pulse. Due to switch power constraints this is the maximum pulse length for a 150 V, < 300 A pulse at a repetition rate of 1 Hz. As discussed previously, during an arc discharge, the plasma current is determined by external circuit characteristics. In this case a high power, tunable resistor with $R = 0.0 - 1.0\ \Omega$ was used to control the discharge current. The approximate current expected from tuning this resistor value is $I = (V - 50)/R$ due to a 50 V potential drop across the plasma. With a capacitance of 48 mF and a resistance of 0.5 Ω, the discharge time constant $\tau = RC$ is 24 ms. This is substantially longer than the discharge pulse length of 200 μs which means we can assume that the voltage applied to the discharge is a constant 150 V over the pulse duration.

4.3.3 Gas Subsystem

Prior to arcing, argon gas is injected into the chamber in between the central HCA tubes. Without gas injection, the nominal chamber pressure is $P \approx 1 \times 10^{-6}$ Torr under continuous pumping using the attached turbo and scroll pumps. Assuming an ionization fraction of

at least 10%, the gas pressure in the inter-electrode region for a plasma density of $n_0 = 1.5 \times 10^{14}$ cm^{-3} should be about 10^{-1} Torr.

To inject Argon gas into our chamber at the appropriate density and flow rate, a hybrid constant flow-pulsed gas system was developed, as seen in Figure 4.9. The vacuum pumping system cannot operate at the given pressure above for extended periods of time so in order to reduce load on the turbo-molecular pump and prevent beam scattering from the gas, it was injected using a fast solenoid, triggered by a short TTL pulse. Once the solenoid is opened it takes some time T to travel into the chamber, depending on the vacuum feedthrough tube length so the discharge pulse is delayed relative to the solenoid opening pulse time. To evenly

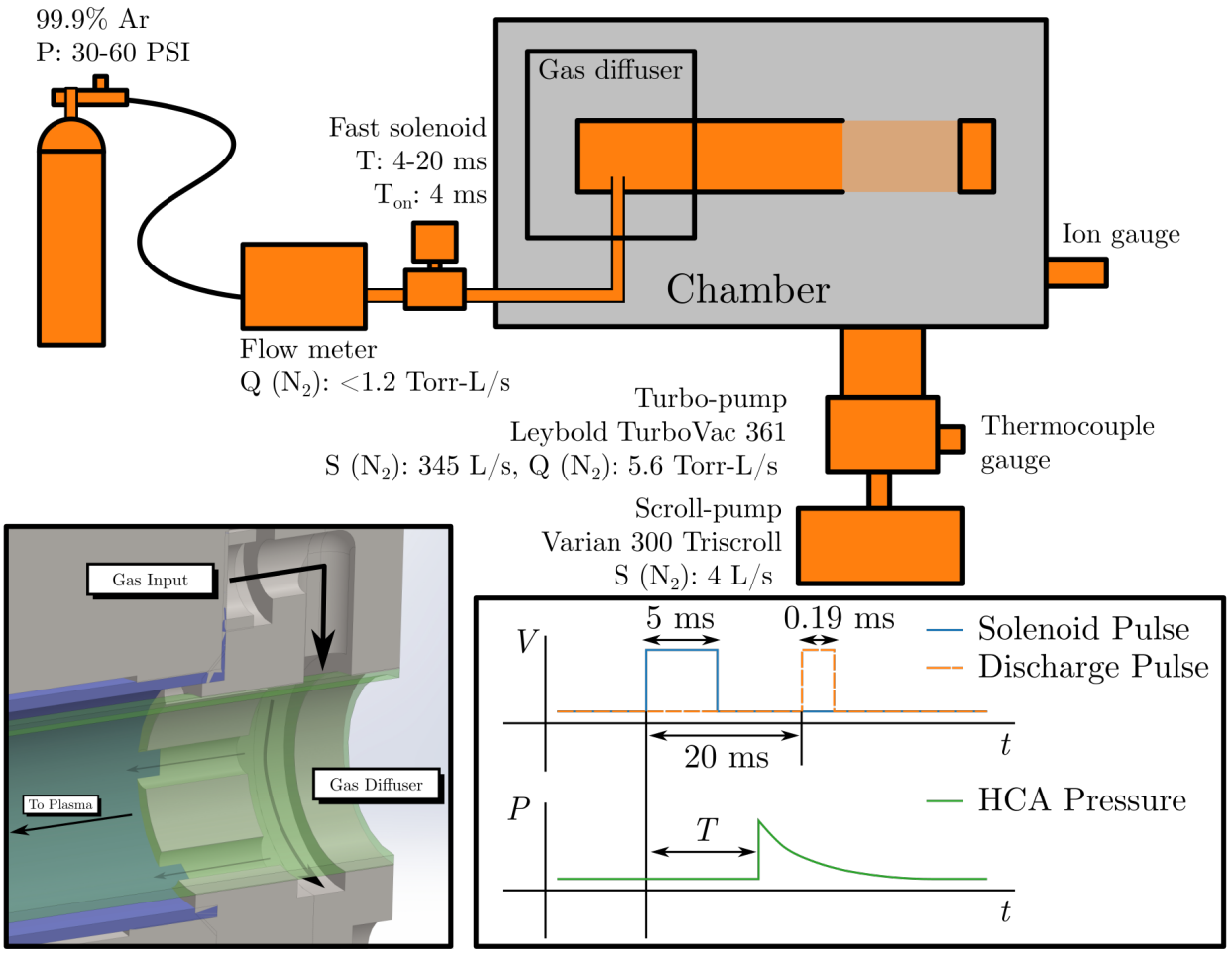

Figure 4.9: Top: Schematic showing the gas flow subsystem. Bottom Left: 3D detail view of gas diffuser. Bottom Right: Timing of voltage trigger pulses for gas solenoid and discharge with a sketch of pressure in the chamber over time.

disperse gas through the annular region between the inner and central tubes a gas diffuser was designed. It consists to two separate parts which are screwed together and then the

inner tube is press-fit into the central hole. When inserted into Cathode arm (B), as seen in Figure 4.9, it accepts gas input and then disperses it into the annular region via a number of smaller channels, evenly spaced around the inner tube.

Ideally gas would only be injected during the arcing period, but a solenoid valve with sub-ms opening/closing time is prohibitively expensive, which means another layer of control is needed to reduce gas flow into the plasma chamber. Our solenoid valve takes roughly 4 ms to open or close. If the chamber was exposed to the Argon source bottle pressure of 30 - 60 PSI for this time, the chamber pressure would destroy the pumps used to maintain vacuum. However, pressures on this order are required to achieve a suitable gas flow rate through feedthroughs into the cathode. To limit the total gas volume introduced into the chamber for each pulse, a tunable gas flow meter was used to limit gas flow into the tube region before the solenoid. Flow was set such that this anti-chamber was refilled to equilibrium pressure in between each pulse, but not high enough that it would flood the plasma chamber while the solenoid valve was open.

With this system in place we were able to maintain a chamber pressure as measured by the thermocouple gauge of below 5×10^{-2} Torr during discharges. Since this measurement happens at the turbo-pump inlet, it is expected that this is the lowest pressure inside our chamber. The pressure should rise significantly as we approach the cathode outlet, increasing by at least an order of magnitude to reach the target plasma density. We can roughly tune the gas pressure in the cathode during arcing by changing the discharge pulse delay. It was observed that for the setup at AWA the minimum pulse delay was 13 ms, before which the arc would not discharge. This depends on the tube length and diameter between the solenoid valve and the vacuum feed-through.

4.3.4 Solenoid Subsystem

A pair of two, water cooled solenoids was used to provide an on-axis magnetic field to confine the plasma. An iron yoke constructed around the pair confined magnetic fields inside the plasma source and improved flux flow through the magnetic circuit. ANSYS Electromagnetic suite [] was used to model the magnetic fields for various coil current densities. On-axis magnetic fields were measured using a longitudinal hall probe on a 1D translation stage to verify simulation accuracy. This measurement, conduced for a number of different solenoid

currents, is seen in Figure 4.10. From this measurement we can see that the magnetic field is

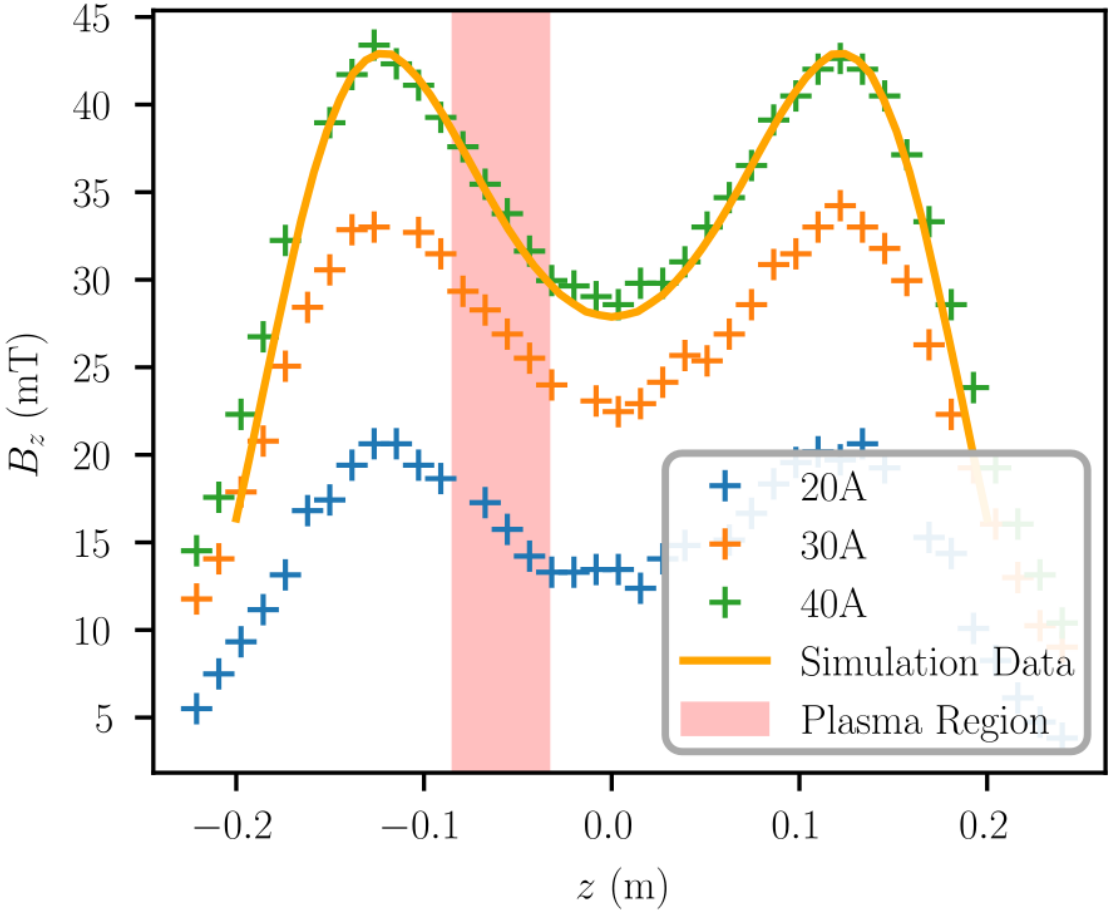

Figure 4.10: On-axis hall probe measurements of the longitudinal magnetic field for different solenoid current settings compared to simulation results. Longitudinal region where the plasma exists is highlighted.

not perfectly uniform inside the plasma region. This is not ideal as it will directly influence the plasma density profile. However, gas density across the discharge is not uniform either, which makes it difficult to achieve a perfectly uniform column regardless. Further intense study of how the gas density and magnetic field interact to make an idealized plasma column.

4.4 Plasma Diagnostics

The measurement of the plasma density and plasma electron temperature is necessary for correctly tuning the plasma source to match simulations and incoming beam parameters. Furthermore, the pulsed nature of the hollow cathode arc source limits the ideal measurement scheme to ones that operate on the 100 µs timescale. A triple Langmuir probe design was then selected to measure the time-resolved plasma density and electron temperature along the longitudinal direction. This section starts with a brief review of basic Langmuir probe theory for context, then it explores the theory of triple Langmuir probes and finally presents the technical design and limitations of the device used for the plasma density measurement.

4.4.1 Plasma Sheaths

To understand the physics involved with probe measurements we must first explore the concept of plasma sheaths. We start by assuming a Maxwellian velocity distribution for both the plasma electrons and ions. If we introduce an isolated, metallic probe into the plasma, electrons and ions will impact the probe surface. Due to their large mass, the ions have a significantly lower temperature than the electrons by several orders of magnitude, which means that electron velocities are higher by at least a factor of $\sqrt{m_i/m_e}$. Significantly more electrons than ions will impact the probe surface and the probe will become negatively charged. Electrons inside the plasma will then be repelled from the probe surface while ions are attracted resulting in a sheath of positive charge, an effect often referred to as Debye shielding [82]. This creates a potential drop from the probe surface to the plasma bulk, as seen in Figure 4.11.

We can solve for the Debye sheath condition by considering the plasma steady state behavior near a metallic boundary at $z = 0$ extending in the positive direction. We assume that particle densities outside the sheath create a quasi-neutral plasma $n_i = n_e$ and that the ion and electron temperatures are given by T_i, T_e respectively. The 1-D ion velocity is given by conservation of energy as

$$\frac{1}{2}m_i u(x)^2 = \frac{1}{2}m_i u_0^2 - e\phi(x) \tag{4.6}$$

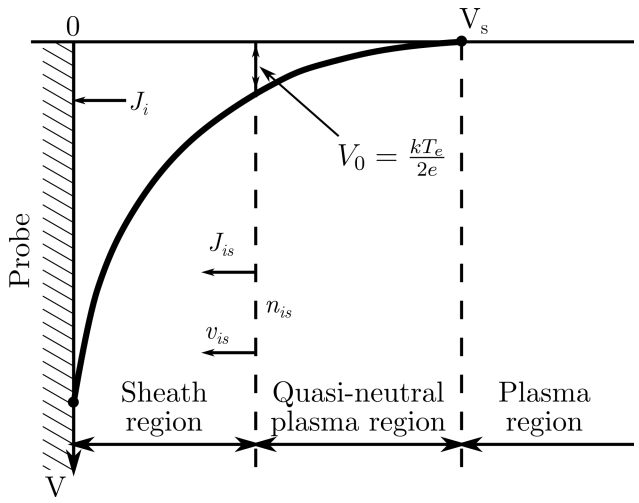

Figure 4.11: Steady-state ion sheath development around a single metallic probe inserted into a plasma.

where u_0 is the ion velocity as it enters the sheath. Conservation of particle number gives

$$n_0 u_0 = n_i(x) u(x). \tag{4.7}$$

In equilibrium and with the presence of an external field, electron density is given by the Boltzmann distribution [83]

$$n_e(x) = n_0 \exp\left(\frac{e\phi(x)}{kT_e}\right). \tag{4.8}$$

Finally, Poisson's equation in 1-D is given by

$$\frac{d^2\phi(x)}{dx^2} = \frac{e(n_e(x) - n_i(x))}{\epsilon_0}. \tag{4.9}$$

If we normalize the potential, position, and ion velocity to

$$\chi(\xi) = -\frac{e\phi}{kT_e} \tag{4.10a}$$

$$\xi = \frac{x}{\lambda_D} \tag{4.10b}$$

$$y = \frac{m_i u_0^2}{2kT_e} \tag{4.10c}$$

$$n_{e,i} = \frac{n_{e,i}}{n_0} \tag{4.10d}$$

where $\lambda_D = \sqrt{\epsilon_0 kT_e/n_0 e^2}$ (or $\lambda_D = 7.2 \times 10^3 (T_e[\text{eV}]/n_0[\text{m}^{-3}])^{1/2}$ in practical units) is the Debye length. Combining these definitions we can calculate the ion density to be

$$n_i = (1 + \chi/y_0)^{-1/2}. \tag{4.11}$$

Poisson's equation can be integrated after multiplying χ' and using the boundary conditions $\chi, \chi' \to 0$ for $\xi \to \infty$ giving

$$(\chi'(\xi))^2 = 4y_0[(1+\chi/y_0)^{1/2} - 1] + 2(e^{-\chi} - 1). \tag{4.12}$$

A solution for this equation can only be found numerically, but we can gain some information by considering that the left side must be greater than zero due to the square. If we expand our equation as $\xi \to 0$ to be

$$(\chi')^2 = \Big(1 - \frac{1}{2y_0}\Big)\chi^2 + \mathcal{O}(\chi^3) \tag{4.13}$$

we find that $y_0 \geq 1/2$. Thus the sheath only forms if the ion velocity satisfies

$$v_0^2 \geq \frac{kT_e}{m_i} \tag{4.14}$$

which is known as the Bohm criterion [84]. If the ion velocity u_0 at the boundary is to small, the sheath potential will "eat" its way deeper into the bulk plasma to accelerate the ions further. Eventually, a quasi-neutral plasma region will develop with a potential drop $V_0 \sim kT_e/2e$ to accelerate ions such that they satisfy the Bohm criterion, as seen in Figure 4.11.

Development of this sheath will be affected if we provide a biasing potential relative to the plasma. Electron and ion currents into a biased probe as a function of bias voltage is shown in Figure 4.12. Several probe bias levels are of particular interest in order to use a

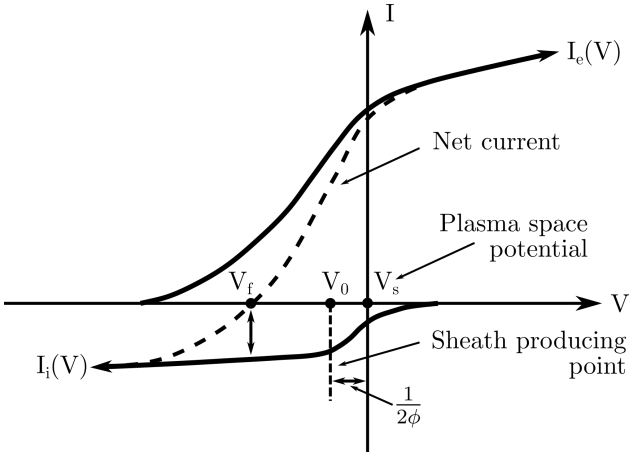

Figure 4.12: Electron and ion current into a biased probe as a function voltage difference between probe tip and plasma where $\phi = e/kT_e$.

probe to measure the plasma density and temperature. When the probe voltage is set above

the plasma space potential, all electrons in a given area near the probe are collected while no ions have the kinetic energy to reach the probe. In this case, the total current is determined solely by the electron density. If we continue to increase the probe voltage, the collection region becomes so large that the probe begins to act as an anode which results in a disruption of the plasma discharge. When the probe voltage is set to V_s such that $\Delta V = 0$ no sheath develops and the net current is due only to thermal particle motion, thus collecting mostly electron current.

Once the bias voltage is reduced to below the space potential such that ions who are accelerated meet the Bohm criterion at V_0, a positive sheath develops. This acts to prevent electrons below a certain energy threshold from reaching the probe, thus reducing the collected electron current. Eventually, the sheath is strong enough to repel a significant portion of the electrons such that no net current is absorbed by the probe. This is equivalent to the isolated probe case discussed earlier. As the probe voltage is pushed lower no electrons have enough energy to reach the probe surface and the electron current goes to zero. The ion current is roughly constant when ΔV is below the sheath producing voltage difference, as the number of ions captured by the sheath region is limited by the overall plasma density. This limit is usually referred to as the ion saturation current. A slight deviation from constant is observed due to a small growth in the sheath size as we push the probe voltage lower.

4.4.2 The Triple Langmuir Probe

Now that we understand how plasma electrons and ions respond to the presence of biased probes we can use them to measure plasma temperature and density.

The single Langmuir probe is the simplest way to measure the density and electron temperature of a plasma. It consists of a simple bare wire inserted into a plasma region with a power supply to bias the probe relative to the plasma potential. Calculation of the density and electron temperature is generally done by fitting the I-V curve near the plasma space potential to determine the electron temperature and then measuring the ion saturation current and solving for the plasma density, using the temperature calculated in the first step.

Despite its simplicity, the single Langmuir probe has several issues. Generally, the probe is operated by automatically sweeping the applied voltage and measuring the response current during the sweep. This requires complicated electronics to do the bias sweep and simulta-

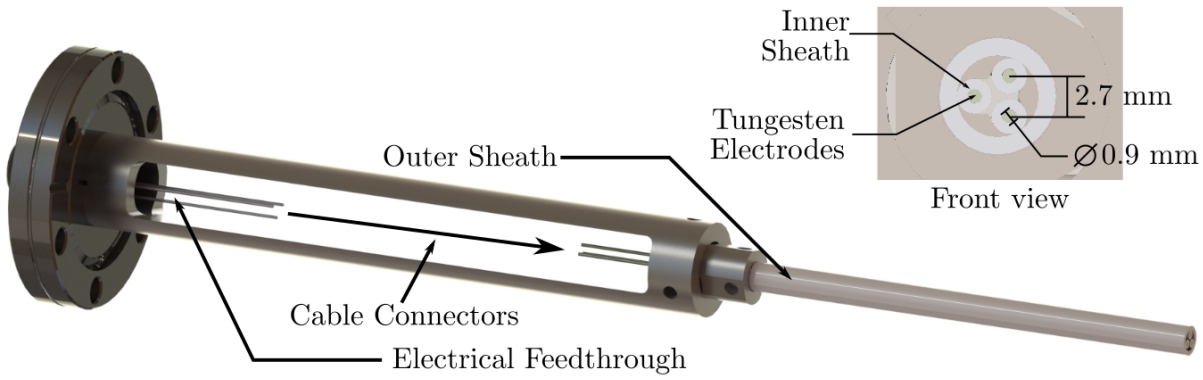

Figure 4.13: CAD drawing of triple probe geometry showing alumina insulating sheath and tungsten probes.

neously measure mA scale currents from the plasma. This along with post-processing can introduce systematic errors in the measurement. Furthermore, sweeping the voltage takes a finite amount of time which prevents time-resolved measurements of the plasma dynamics below the sweep period. State of the art voltage sweepers can reach only 500 µs periods, whereas plasma phenomena can take place on a 100 MHz - 100 GHz timescale.

The triple Langmuir probe design solves the time resolution problem by making three simultaneous measurements of the I-V curve. Simply put, the triple Langmuir probe is a combination of three individual probes which are biased at different voltages relative to the plasma space potential. The design was first published in a paper by S. Chen and T. Sekiguchi [2]. Their theory and resulting design are reproduced here for reference. The analysis contained here rests on three assumptions, (a) the electron energy distribution in the plasma is Maxwellian. (b) The mean free path of the electrons is larger than both the ion sheath thickness as well as the probe radius. (c) The ion sheath thickness is smaller than the probe separation, such that the interaction effects between adjacent probes are negligible. The first assumption is valid for most laboratory plasmas, the second and third conditions are satisfied by probe design choices. An estimate for the mean free path $\bar{\lambda} = 1/\pi d^2 n_0$ for electrons in an argon gas ($d = 140$ pm) with a pressure of 10^{-1} Torr is equal to about 105 mm. The Debye length (the scale size for the ion sheath) for our plasma density is about 2 µm which is significantly smaller than the mean free path. To satisfy conditions (b) and (c) the triple probe used in this experiment had three tungsten probes with a separation of 2.7

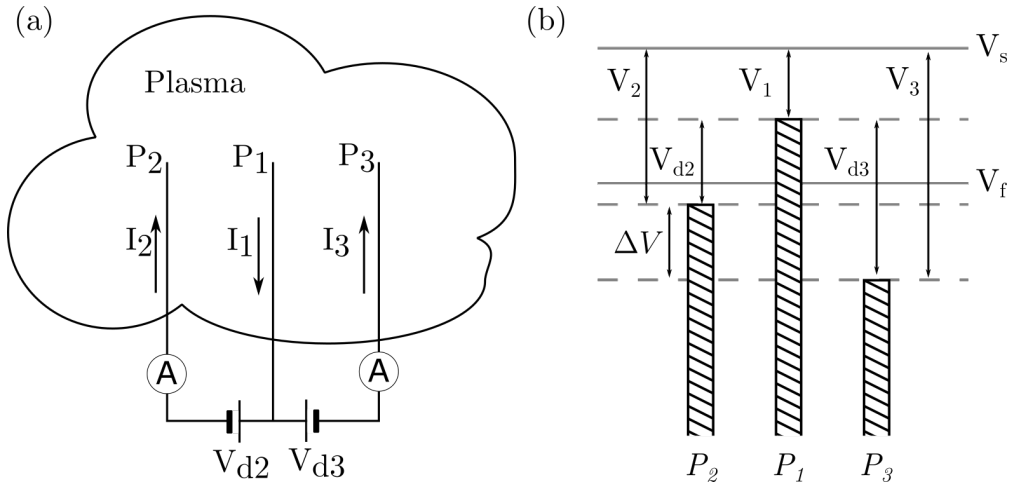

Figure 4.14: (a) Electrical schematic of triple probe measurement system and (b) relative potential of each probe due to biasing (adapted from [2]).

mm and a diameter of 0.9 mm, as seen in Figure 4.13.

An electrical schematic of the probe is shown in Figure 4.14. The outer two probes are biased with respect to the central probe and current in the two biased probes is measured. If the bias voltages Vd2 and Vd3 are both zero then no current flows between the probes and their voltages become fixed at the plasma floating potential (see single Langmuir probe section). If the bias voltages become negative with respect to the reference probe then P2 and P3 are forced below the floating potential which dictates that current flow through these probes is mainly ion current. Conversely, if the reference probe is raised slightly above the plasma floating potential and sees mostly electron current.

Current flowing into the probes at any instant is given by

$$-I_1 = -SJ_e \exp(-\phi V_1) + SJ_i(V_1) \tag{4.15a}$$

$$I_2 = -SJ_e \exp(-\phi V_2) + SJ_i(V_2) \tag{4.15b}$$

$$I_3 = -SJ_e \exp(-\phi V_3) + SJ_i(V_3) \tag{4.15c}$$

$$\phi = e/kT_e \tag{4.15d}$$

$$J_e = n_e e(kT/2\pi m_e)^{1/2} \tag{4.15e}$$

where S is the probe surface area exposed to the plasma and J_e, J_i are the electron and ion saturation currents respectively. We wish to operate the probes at voltages far below the sheath producing voltage V_0 (see Figure 4.12). In this limit the ion current density is roughly independent of the probe reference, i.e. $SJ_i(V_1) \simeq SJ_i(V_2) \simeq SJ_i(V_3)$. If we assume that

this is indeed the case we find that

$$\frac{I_1 + I_2}{I_1 + I_3} = \frac{1 - \exp(-\phi V_{d2})}{1 - \exp(-\phi V_{d3})} \tag{4.16}$$

which gives an explicit measurement of the electron temperature T_e. We can also solve for the ion saturation current

$$J_i = \frac{1}{S} \frac{I_3 - I_2 \exp(-\phi \Delta V)}{1 - \exp(-\phi \Delta V)} \tag{4.17}$$

where $\Delta V = V_{d3} - V_{d2} = V_3 - V_2$. The three currents I_1, I_2, I_3 are related through Kirchhoff's law so I_1 can be determined via I_2, I_3. Those measurements, along with the known biasing potentials, directly measures the electron temperature T_e and the ion saturation current J_i.

As voltages of the triple probe are below the plasma voltage, we cannot directly measure the electron saturation current and thus the plasma density. We aim to use our understanding of sheath development to translate measurement of the ion saturation current to infer the plasma density. We know ion saturation velocity and current at the sheath boundary must satisfy Bohm's criterion, thus

$$v_{is} = (kT_e/m_i)^{1/2} \tag{4.18a}$$

$$J_{is} = en_{is}v_{is} = en_{is}(kT_e/m_i)^{1/2}. \tag{4.18b}$$

Assuming that the electron and ion densities are roughly equal in the quasi-neutral region and the electron density is given by Eqn. 4.8 at the sheath boundary then

$$n_{is} \simeq n_{es} = n_e \exp(-\phi(1/2\phi)) = n_e \exp(-1/2) \tag{4.19}$$

If we assume that the sheath boundary has nearly the same surface area S' as the probe S then the ion current can be related to the plasma density

$$J_i = (S'/S)J_{is} \simeq J_{is} = en_e(kT_e/m_i)^{1/2} \exp(-1/2). \tag{4.20}$$

Thus a measurement of both the ion saturation current and the electron temperature is enough to infer the plasma density.

4.4.3 Direct-Display System

A modification to the triple probe design seen in Figure 4.6 allows an easier, direct measurement of the electron temperature and plasma density. A schematic describing this modification is seen in Figure 4.15. We disconnect P_2 from the other two probes and terminate

it with an MΩresistor to prevent current flow into the probe ($I_2 = 0$). This causes the probe voltage to immediately increase up to the floating potential of the plasma. It also sets $I_1 = I_3$, thus Eqn. 4.16 becomes

$$\frac{1}{2} = \frac{1 - \exp(-\phi V_{d2})}{1 - \exp(-\phi V_{d3})}. \tag{4.21}$$

From this we can calculate the electron temperature simply by measuring the voltage difference between the reference probe (P_1) and our floating probe (P_2). If we choose our bias voltage V_{d3} such that $\phi V_{d3} >> 1$ then the electron temperature is simply $kT_e = eV_{d2}/\ln(2)$. If we plug these currents into the equation for saturation current Eqn. 4.20 and use Eqn. 4.21 we get

$$J_i = (I/S)[\exp(\phi V_{d2}) - 1] \tag{4.22}$$

yielding the plasma density to be

$$n_e = \frac{m_i^{1/2} I}{S} \frac{\exp(1/2)}{e\sqrt{kT_e}[\exp(\phi V_{d2}) - 1]} \tag{4.23}$$

In practical units, $n_e[\mathrm{cm}^{-3}]$, $S[\mathrm{mm}^2]$, $I[\mu\mathrm{A}]$, $T_e[\mathrm{eV}]$, and M (effective ion mass), and plugging in $kT_e = eV_{d2}/\ln(2)$ this becomes

$$n_e = 1.05 \times 10^9 \frac{M^{1/2} I}{S T_e^{1/2}} \tag{4.24}$$

If our argon based plasma (M = 40), has a density of $n_e = 1.5 \times 10^{14}$ cm^{-3}, and an electron temperature of 10 eV we expect a voltage difference $V_{d2} = 6.9$ V and a probe current of $I \sim 45$ mA.

With this in mind we can choose the circuit parameters seen in Figure 4.15. We directly measure the voltage difference between V_f and V_+ by subtracting waveforms measured on an oscilloscope, both terminated by 1 MΩ internal resistors. The probe current I is measured using a shunt resistor with a resistance of 100 Ω and measuring the potential difference across the shunt. Biasing voltage is chosen such that the potential difference $V_{d3} >> kT_e/e$, taking into consideration the voltage drop across the shunt resistor. In order to measure voltages relative near the plasma floating voltage the bias potential was supplied using a collection of isolated 9 V batteries for a total voltage of 54 V, exceeding an expected electron temperature of 10 eV [3] by at least a factor of 4.

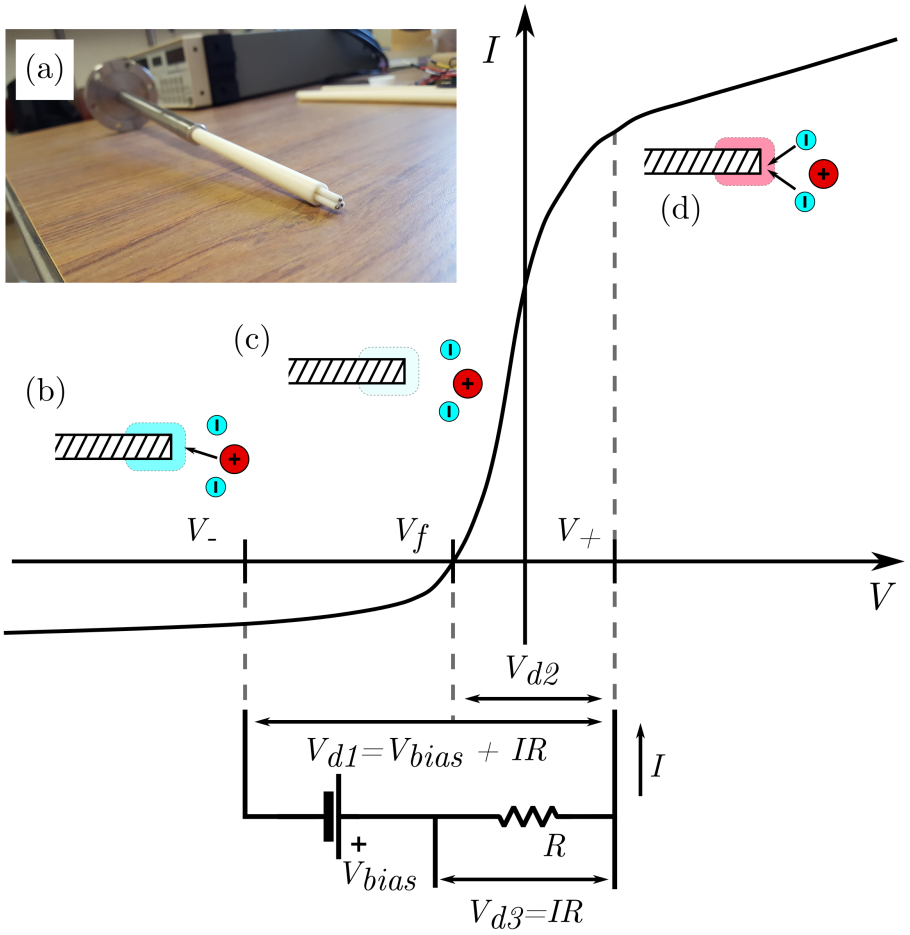

Figure 4.15: Overview of Triple Langmuir Probe direct display plasma density measurement. Three electrodes (a) are inserted into the plasma region. Two of the probes are biased with respect to one another to collect ion saturation (b) and electron current just above the floating voltage (d). The final probe (c) is left at the plasma floating potential which collects no net current. A simultaneous measurement of the floating potential and the current through the biased probes yields a direct measurement of the plasma temperature and density.

4.5 Plasma Measurements

Measurements of the plasma discharge response from the pulsed voltage source are seen in Fig. 4.16. Figure 4.16(a) shows a measurement of the modified Paschen curve due to external cathode heating. For each chamber pressure p, the voltage was increased from 0 V until a discharge with current of at least 1 A developed which was considered to be the breakdown voltage V_B. The measured curve shows differences in structure when compared to cold cathode measurements. A lack of asymptotic behavior at low gas pressures is particularly significant and is most likely due to constant thermionic electron current creating a "quasi-

self sustaining" discharge.

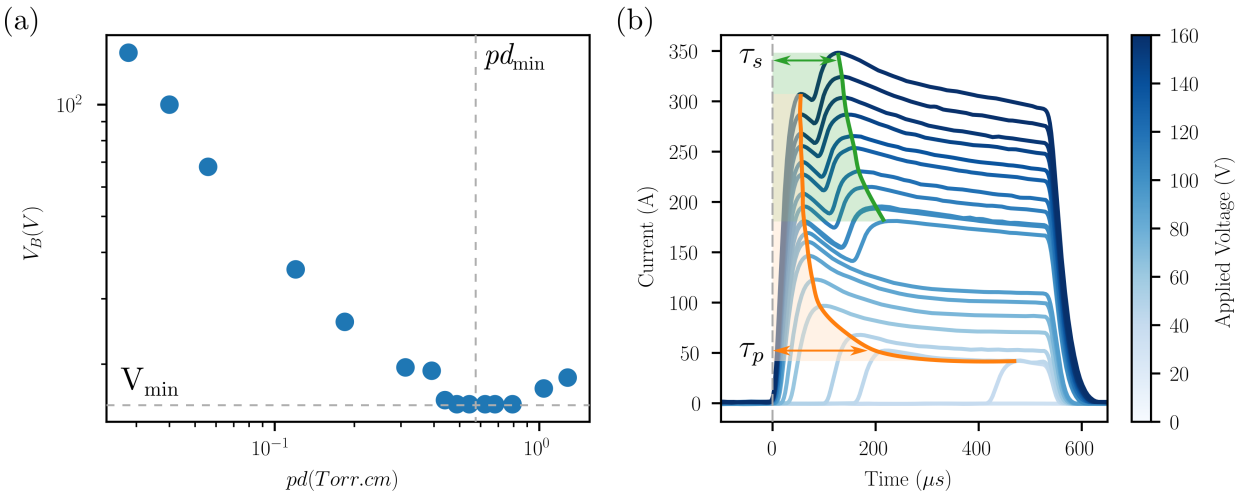

Figure 4.16: Plasma discharge measurements with external heating at 5 kW and solenoid current of 10 A. (a) Modified Paschen curve [80] of plasma breakdown voltages V_B with at least 1 A discharge current. Minimum breakdown voltage is 15.6 V at pressure $p = 7.8 \times 10^{-2}$ Torr ($d = 8$ cm). (b) Current traces of discharges at different applied voltages. Discharges start at $t = 0$ and τ_p, τ_s are the primary and secondary formative time lags for reaching steady state discharge.

Figure 4.16(b) shows the plasma discharge temporal evolution as a function of discharge voltage. We observe that at low voltages the discharge current reaches a peak significantly after the voltage is applied (orange line). This effect is known as the primary formative time lag τ_p of the plasma discharge, and is influenced by the "overvoltage" applied $V_o = V - V_B$. If the voltage applied is precisely equal to the breakdown, $V_o = 0$ and the formative time $\tau \to \infty$. As overvoltage increases, the time lag decreases in an exponential manner, consistent with previous experiments [1].

A secondary peak in the discharge current is observed once a higher applied voltage of ≈ 80 V is reached which is due to secondary electron emission mechanisms [1]. This is most likely due to cathode emission due to positive-ion impact. As discussed before, plasma ions are accelerated towards the cathode by the discharge potential. Once this reaches a high enough level, impact from these ions triggers secondary electron emission. The ion drift velocity is much slower than the electron drift and thus the secondary emission formative time τ_s is greater than the primary time scale.

Initial measurements of the plasma density were carried out at a single location. Results of the time dependent plasma temperature and density are seen in Figure 4.17. Time dependent measurements of the plasma temperature and density were taken during ten consecutive shots at a frequency of 1 Hz and the average time dependent plasma parameters were calculated. In this case we see a plasma density close to 3×10^{13} cm^{-3} and an electron temperature of nearly 40 eV. The measured electron temperature is suspect, as it is at least a factor of four larger than the majority of historical measurements for related devices [3]. There are a number of potential systematic errors in our measurement. We began our probe analysis assuming that the electron temperature had a Maxwellian distribution. In the case of high gas flow and/or a large discharge voltage we could imagine that the electron velocity is significantly anisotropic, biased towards the anode. This could allow more electrons to climb the plasma sheath into the electrodes, resulting in a higher electron temperature. Exactly how much error this introduces into our measurement would have to be the subject of further study. However, if we suppose that the real electron temperature is a factor of four smaller (10 eV) than our measurement, then the plasma density would only be off by a factor of two. Our goal is to match the plasma density to the beam parameters by at least an order of magnitude, so this systematic error is tolerable. Furthermore, we will have a chance to compare these measurements with a measurement of the plasma wakefield wavelength, which can also provide an estimate for the average density.

The triple Langmuir probe was then used to measure the on-axis plasma density. It was mounted on a linear stage in order to map out plasma density inside and outside of the inter-electrode region. The profile was measured for three different solenoid settings relevant for beam-plasma experiments. These results are seen in Figure 4.18. As mentioned earlier plasma collimation using solenoids affects the voltage required for discharge. This prevented discharges at 150 V, so in order to achieve discharge, power to the cathode tubes was increased to raise the tube temperature.

The triple Langmuir probe was comparable to the radius of the hollow cathode and it was found that the probe prevented discharges when nearing the cathode exit (hollow points in Figure 4.18). It's reasonable to assume that the triple probe size is what prevents discharges in this case, either due to disrupting the gas flow or discharge path. In order to characterize this region we used direct imaging of the plasma afterglow using a CCD camera. Normally,

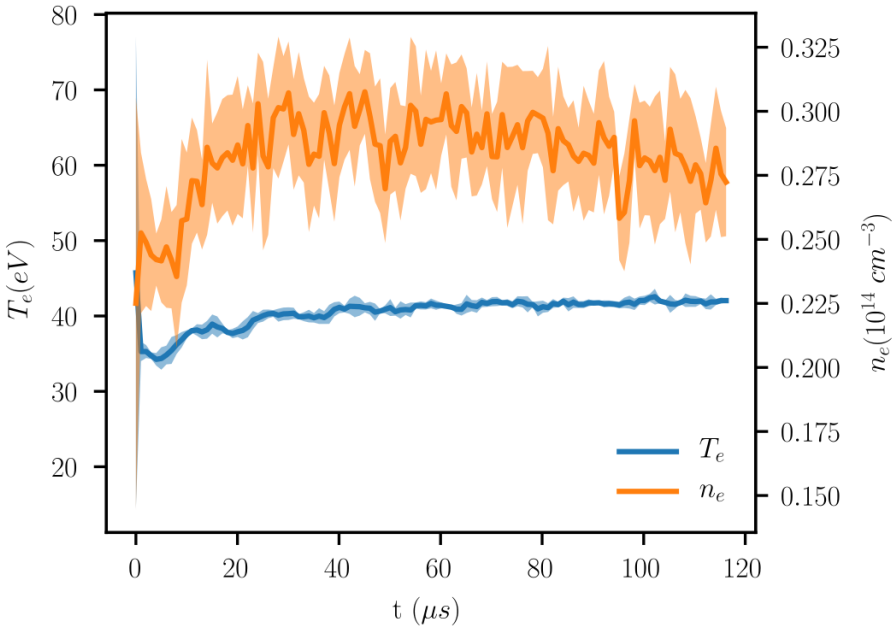

Figure 4.17: Plasma temperature and density as a function of time during a plasma discharge with solenoid current set to 40 A and probe located approximately 2 cm from the cathode. Shading represents a one-sigma deviation from the average of 10 shots.

light from heating the cathode prevents imaging anything inside of the plasma source. To get around this, the CCD was electronically gated to a pulse length of 20 µs and triggered (with an adjustable delay) by the discharge TTL pulse. It captures instantaneous light from arc, which is much brighter than the background blackbody radiation during this ultra-short period. If we assume that the light intensity is proportional to the plasma density [85] we can use these images to extrapolate absolute plasma density in tandem with the triple probe measurement, as seen by the dotted lines in Fig. 4.18. Furthermore, we can see the transverse extent of the plasma is roughly equal to the hollow cathode diameter. We have no way of imaging the plasma profile immediately after the cathode end or inside the hollow region of the cathode. Based on what we think the gas density is in this region we can guess that the plasma density is at its' highest just inside the cathode and then drops quickly to zero at the smaller tube end, where gas density drops to zero.

This measurement gives us clues as to how the beam behaves inside the plasma region. Without plasma present, the beam simply reaches a waist halfway through the inter-electrode space and then expands just as in a normal drift space. With plasma present, the beam first sees a sharp rise in plasma density which acts to non-adiabatically focus a part of the beam

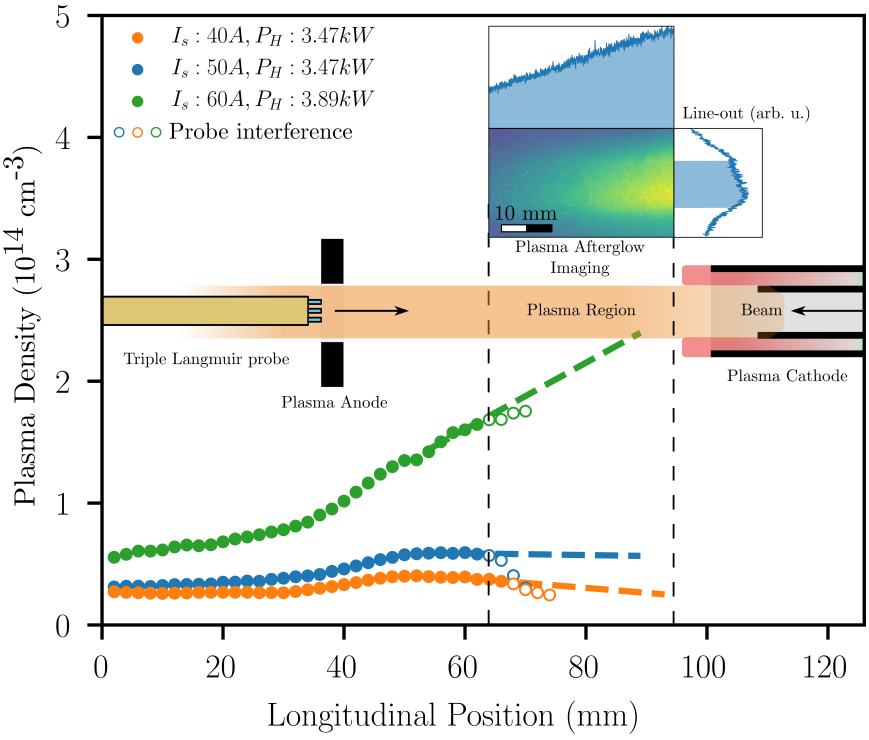

Figure 4.18: Longitudinal plasma density characterization for different discharge settings of solenoid current I_s and heater power P_H. A longitudinally scaled cartoon of source geometry and diagnostics. Plasma profile is extrapolated (dashed lines) through direct plasma afterglow imaging (inset) and fitting longitudinal glow line-out. Transverse plasma density line-out is also shown.

to match the plasma wavelength. This portion of the beam goes through several betatron oscillations, exciting a wakefield in the plasma that modulates the beam energy. Finally, the beam exits the plasma region, adiabatically expanding as the decrease in plasma density is over several betatron periods. Of course we cannot verify any of this behavior directly but we can see aspects of the interaction in longitudinal phase space measurements. Details regarding the transverse motion of the particles is contained in the efficiency of acceleration, as mismatched particles are lost to the walls of the accelerator and are not detected in our diagnostic. Transverse motion can also account for a reduction in the final acceleration of the beam, as the plasma wakefield response also depends on the beam's transverse size. We can attempt to characterize these plasma profiles by calculating their effective length L_{eff}

and the mean plasma density $< n_p >$ as

$$L_{eff} = \frac{1}{max(n_p)} \int_{z_{min}}^{z_{max}} n_p(z')dz' \tag{4.25a}$$

$$< n_p > = \frac{1}{z_{max} - z_{min}} \int_{z_{min}}^{z_{max}} n_p(z')dz' \tag{4.25b}$$

For a zero order calculation we assume a linear plasma ramp from the end of the extrapolation (at $z = 95$ mm) region to the end of the inner cathode tube (at $z = 110$ mm) we calculate these attributes for the three profiles in Fig. 4.18 in Table 4.2

Solenoid Strength (A)	Heater Power (kW)	L_{eff} (mm)	$< n_p >$ (10^{14} cm^{-3})
40	3.47	76	0.3
50	3.47	76	0.4
60	3.89	57	1.3

Table 4.2: Calculated plasma stats for profiles in Fig. 4.18.

It's clear from these metrics and Fig. 4.18 that an increase in solenoid field increases the plasma density as expected from confinement calculations. Furthermore, we can see evidence that an increase in tube temperature due to increased heater power gives rise to a much greater increase in plasma density than the solenoid increase by itself. It is likely that an increase in thermal electron current from the heated cathode leads to a higher ionization fraction, as the plasma density increases without an increase in gas pressure or flow rate.

CHAPTER 5

Experimental Beamline Optimization and Design

In this chapter we will discuss experimental beamline design issues for beam transport to the plasma source and longitudinal diagnostics. The 6D beam distribution, as determined by OPAL simulations (see Chapter 2), is complex due to the emittance exchange process. Care must also be taken to preserve the current profile. Here we discuss design and simulation of the dedicated plasma experiment beamline and the issues herein. Finally, we will discuss the design of various critical diagnostics including beam size monitoring inside the plasma source and longitudinal phase space measurement of the beam after plasma interaction.

5.1 Plasma Beamline Design Goals

Goals for the plasma beamline design are as follows: 1) Transport output from the EEX beamline to the plasma source IP, where the beam size at the IP matches expected plasma density betatron size, 2) Preserve the current profile through our beamline to the longitudinal phase space (LPS) diagnostic, 3) Prevent emittance growth to reduce beam losses throughout the beamline and allow resolvable measurement of the longitudinal phase space in both energy and time.

Optimization and design of the beamline was done using the simulation code elegant [86] which uses a simplex differential optimizer and is ideal for rapid optimization of quadrupole elements. It also contains an accurate model for multiple scattering in materials, used to model vacuum windows before and after the plasma source. The particle distribution from OPAL after emittance exchange served as the starting point of the elegant simulation. Constraints for optimization included maximum available field gradients from quadrupoles and practical constraints pertaining to maximum beamline length (< 8 m) and minimum distances between elements.

5.2 Beamline Overview

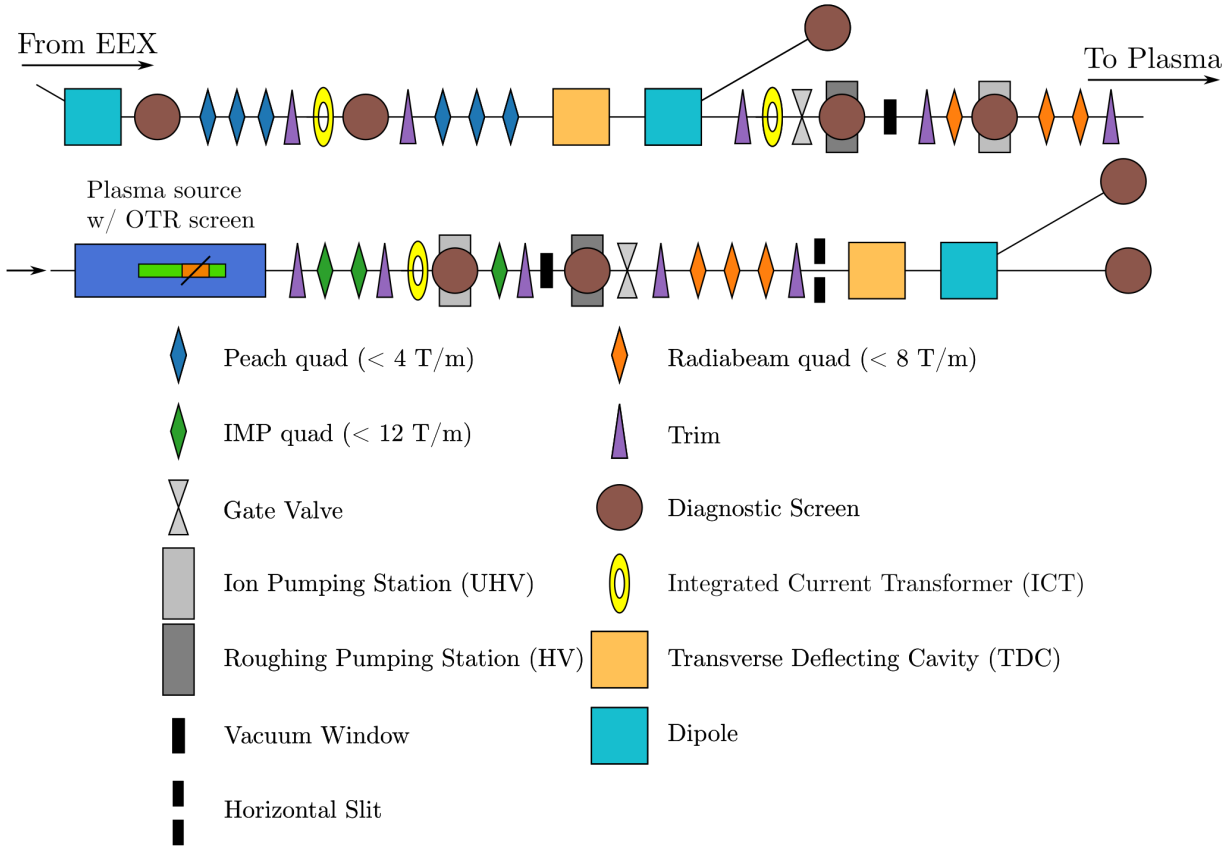

Figure 5.1: Design of entire plasma experimental beamline showing major magnetic, vacuum and diagnostic components.

The major components of the final beamline design are shown in Figure 5.1. The overall design is as follows:

Beams coming from the emittance exchange beamline are transported through the transfer line (area between final EEX dipole and the next dipole). This portion of the beamline was kept, as it forms part of the to-be-installed double emittance exchange beamline [71]. The outgoing beam from EEX can be characterized in this region through the use of a quadrupole or slit scan to measure the emittance. Beam charge can also be measured using an integrated current transformer (ICT).

Beams are then focused into the first vacuum window. A 125 µm thick Beryllium sheet is used to separate the ultra-high vacuum (UHV) drive and EEX beamlines from the plasma source vacuum. The window also prevents particulates from reaching the clean UHV region, as water vapor and organic compounds can destroy the sensitive cesium-telluride cathode

and copper accelerating structures contained in the drive beamline. Window thickness is minimized until a material strength limit is reached, as the window must be able to withstand atmospheric pressure on one side when the plasma source is attached. Minimizing the window thickness is necessary to prevent beam emittance growth from multi-particle scattering. Beam particles have a chance to elastically scatter off of atoms in the window, thus strongly deflecting the particle trajectory. If the material thickness is large enough, it is likely that beam particles will scatter off of multiple atoms in the material. We can approximate the interaction as an uncorrelated addition to the particle divergence ξ with a Gaussian distribution and an rms angle of [87]

$$\sigma_\xi = 13.6\frac{\sqrt{X/X_0}}{p\beta}[1 + 0.088\log_{10}(X/X_0)] \tag{5.1}$$

where X/X_0 is the material thickness in terms of their radiation length, p is the beam momentum in MeV/c and β is the relativistic velocity v/c. We calculate the final single-particle divergence as

$$x'_f = x'_i + \xi. \tag{5.2}$$

The final rms divergence after the window is

$$\sigma^2_{x',f} =< x'^2_f >=< x'^2_i > + < \xi^2 >= \sigma^2_{x',i} + \sigma^2_\xi \tag{5.3}$$

where $< x'_i\xi >= 0$ because the scattering angle is uncorrelated. We see that the relative error in the final rms divergence due to the scattering term can be reduced if the incoming divergence of the beam is large, which is maximized by locating a beam waist at the window location. Beam emittance in this case is given by[1]

$$\epsilon^2_x = \sigma^2_x\sigma^2_{x'} = \sigma^2_x(\sigma^2_{x',i} + \sigma^2_\xi) \tag{5.4}$$

thus the growth in emittance is proportional to the beam size at the window. Scattering also acts to changes the beam waist if it is not located at the window itself [88].

The beam is then focused into the plasma source. To match a plasma density of 1.5×10^{14} cm^{-3} we wish to focus the beam to meet the equilibrium betatron function at the beam waist $\beta^* \approx 5$ mm. The betatron function in a drift near the waist is given by

$$\beta(z) = \beta^* + \frac{(z - z^*)^2}{\beta^*} \tag{5.5}$$

[1]Note that at a waist $\sigma^2_{xx'} = 0$.

where z^* is the longitudinal location of the waist. To achieve a tight focus without losing beam to scraping we would like to place our focusing quadrupoles as close as possible to the interaction point to limit large beam sizes in the quadrupoles. However, to properly align the beam going through the plasma cathode we need transverse screens to measure the beam position before and after the plasma source. This requires significant beamline space that prevents quadrupoles from getting closer to the waist. Balancing these needs resulted in the modified triplets seen in the beamline overview, where the alignment screen is placed in-between the first and second quadrupole triplet magnets.

Unfortunately, even after this design effort, the closest a quadrupole can get to the plasma interaction point is roughly 0.25 m. To reach the desired waist size the betatron function at this final quadrupole is $\beta(0.25) = 12.5$ m, which for beams with a normalized transverse emittance of 400 mm-mrad corresponds to an rms beam size of 8 mm. In a final focus triplet arrangement, the beam can grow even larger in one direction through the middle quadrupole. This can result in significant beam losses before and after the waist location, especially if misalignments are present in the upstream beamline leading to unexpected emittance growth or beam scraping on the beamline walls.

Measurement of the transverse beam size at the plasma interaction point was done using an optical transition radiation (OTR) diagnostic. When a charged particle approaches a perfectly conducting metallic boundary at a 45 deg angle, as seen in Fig. 5.2(a), it sees an opposite image charge traveling perpendicularity, created by rearrangement of electrons in the metal. Due to forces from this image charge the incident electron decelerates and thus emits radiation. The resulting radiation power at optical frequencies is given by [89]

$$\frac{d^2I}{d\omega d\Omega} = \frac{1}{4\pi^2 c}\left|\frac{-e\sin\theta}{1-\beta\cos\theta} + \frac{e\sin\theta'}{1-\beta\cos\theta'}\right|^2. \tag{5.6}$$

For highly relativistic beams $\beta \to 1$ and the radiation lobes tend to be perpendicular to the beam axis, thus $\theta \approx \pi/2$ and $\theta' << 1$. In this case the first term in Eqn. 5.6 can be ignored and $\sin\theta' \approx \theta'$. With this limit taken into account Eqn. 5.6 becomes

$$\frac{d^2I}{d\omega d\Omega} = \frac{e^2}{4\pi^2 c}\left[\frac{\theta'^2}{(1-\beta\cos\theta')^2}\right] \tag{5.7}$$

if we use $\beta = 1 - 1/(2\gamma^2)$ and continue our use of the small angle approximation we get

$$\frac{d^2I}{d\omega d\Omega} = \frac{e^2}{4\pi^2 c}\frac{\theta'^2}{(\theta'^2+\gamma^{-2})^2} = \frac{e^2}{4\pi^2 c}f(\theta'). \tag{5.8}$$

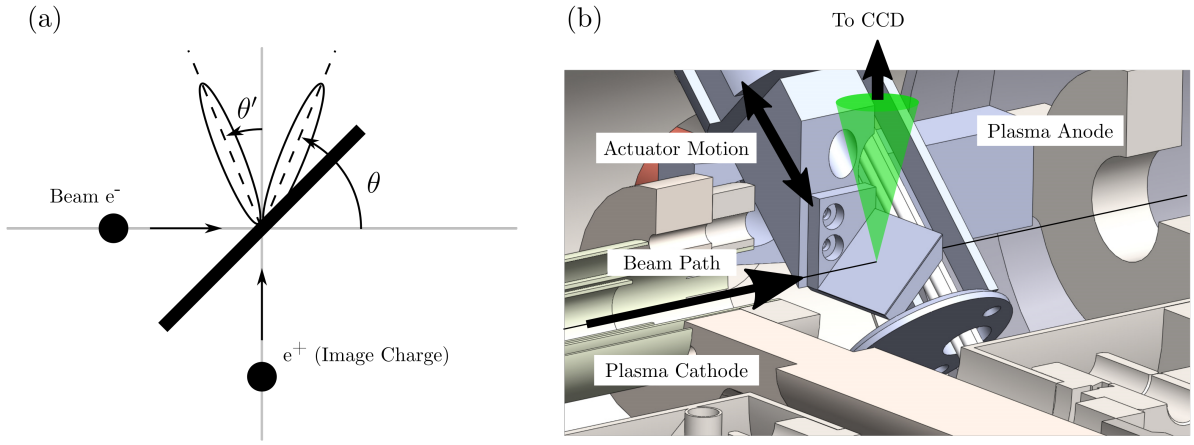

Figure 5.2: (a) Cartoon of optical transition radiation (OTR) beam interaction with metallic foil. (b) OTR diagnostic shown inserted into the plasma source.

If we find the maximum of $f(\theta')$ by taking the derivative and setting it to zero we find that it reaches a peak at $\theta'_m = 1/\gamma$. For the design of our diagnostic we need to simply capture this light through a camera aperture, so with our beam energy of 40 MeV, we require an angular acceptance of 13 mrad.

The OTR diagnostic design inside the plasma source is shown in Fig. 5.2(b). The diagnostic cannot be present in the beam path when plasma discharges are active so it is mounted on an actuator that removes it during plasma discharges. Maintaining the surface quality of the metal is also important, so a shield protects it during plasma discharges. In place of a thin foil, a round Thorlabs silver coated mirror with a peak to valley surface flatness of 5λ at 632.8 nm was used to guarantee specular reflection.

Once the beam is transported through the plasma source, it is sent into another vacuum window which protects the longitudinal phase space diagnostic from the dirty plasma vacuum. To focus the beam into this window a mirrored quadrupole triplet with respect to the plasma waist is used, symmetrizing the beam size on either side of the plasma source. Once through the second window, a final triplet is used to focus beam into the LPS diagnostic.

The longitudinal phase space (LPS) diagnostic consists of a rotated transverse deflection cavity and a 20 deg dipole spectrometer separated by a drift. The 6D transport matrix for these components is given by

$$M_{LPS} = M_{d_2} M_{DIP} M_{d_1} M_{TDC} \tag{5.9}$$

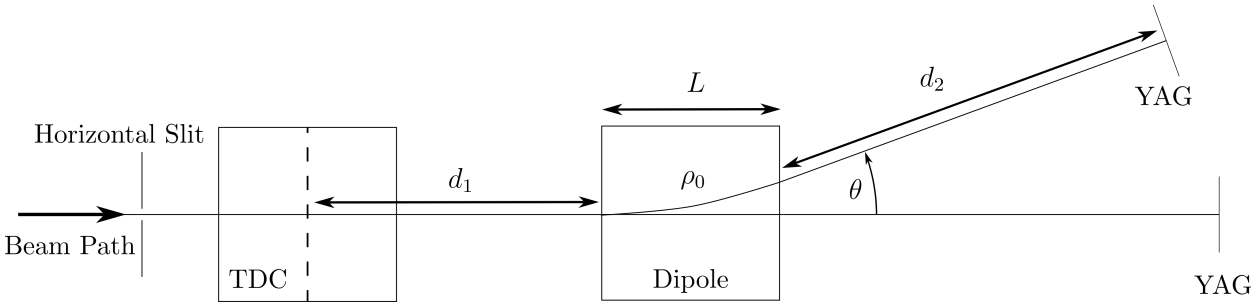

Figure 5.3: Geometry of longitudinal phase space diagnostic elements.

From this we can calculate single particle transverse coordinates at a screen are given as

$$\begin{aligned} x_f &= (C - hSd_2 + hCTd_2)x_i + (C(d_1 + d_2 + d_1d_2hT) + S(1/h - hd_1d_2 + Td_2))x_i' \\ &\quad + k\Big(Sd_2 - \frac{(1-C)(1+hTd_2)}{h}\Big)y_i \\ &\quad + (Sd_2 - \frac{(1-C)(1+hTd_2)}{h})\delta_i \end{aligned} \tag{5.10a}$$

$$y_f = (1 - hTd_2)y + (d_1 + d_2 + L - hT(d_1d_2 + d_2L))y_i' + \kappa(d_1 + d_2 + L - hT(d_1d_2 + Ld_2))(ct_i) \tag{5.10b}$$

where $h = 1/\rho_0$ with the dipole bend radius ρ_0, L is the rectangular dipole length, (S, C, T) are $(\sin(\theta), \cos(\theta), \tan(\theta))$ respectively, d_1, d_2 are the distances from the center of the TDC to the dipole edge and the dipole edge to the screen respectively. The parameter κ is the geometric kick strength of the transverse deflecting cavity and we have made the substitution $z_i = ct_i$. An ideal measurement of the LPS would mean that x_f, y_f were purely functions of δ_i, z_i but this is clearly not the case. For a given beamline geometry and element strength, we want to reduce the beam emittance to improve minimum resolution of each measurement (characterized by the absolute size of unwanted terms not a functions of δ_i, z_i). Unfortunately, due to multiple scattering in the vacuum windows our emittance is quite large, significantly damaging the minimum resolution of our diagnostic. We can mitigate this by using collimation, at the expense of observable beam charge. The choice of collimator depended on YAG screen sensitivity and full collimation in both directions would have reduced the overall beam charge too much. Vertical collimation with a horizontal slit was chosen based on the importance of temporal resolution and it also removes the y_i component of the final x_f equation.

5.3 Beamline Simulation and Optimization

As discussed previously the beam distribution output form OPAL was used at the beginning of an "elegant" simulation to model the plasma beamline. Optimization of the quadrupole strengths and locations was performed with the results seen in Fig. 5.4. Five sets of quadrupole triplets are used to achieve beam waists at the two vacuum windows, plasma source and LPS diagnostic screen (beamline end).

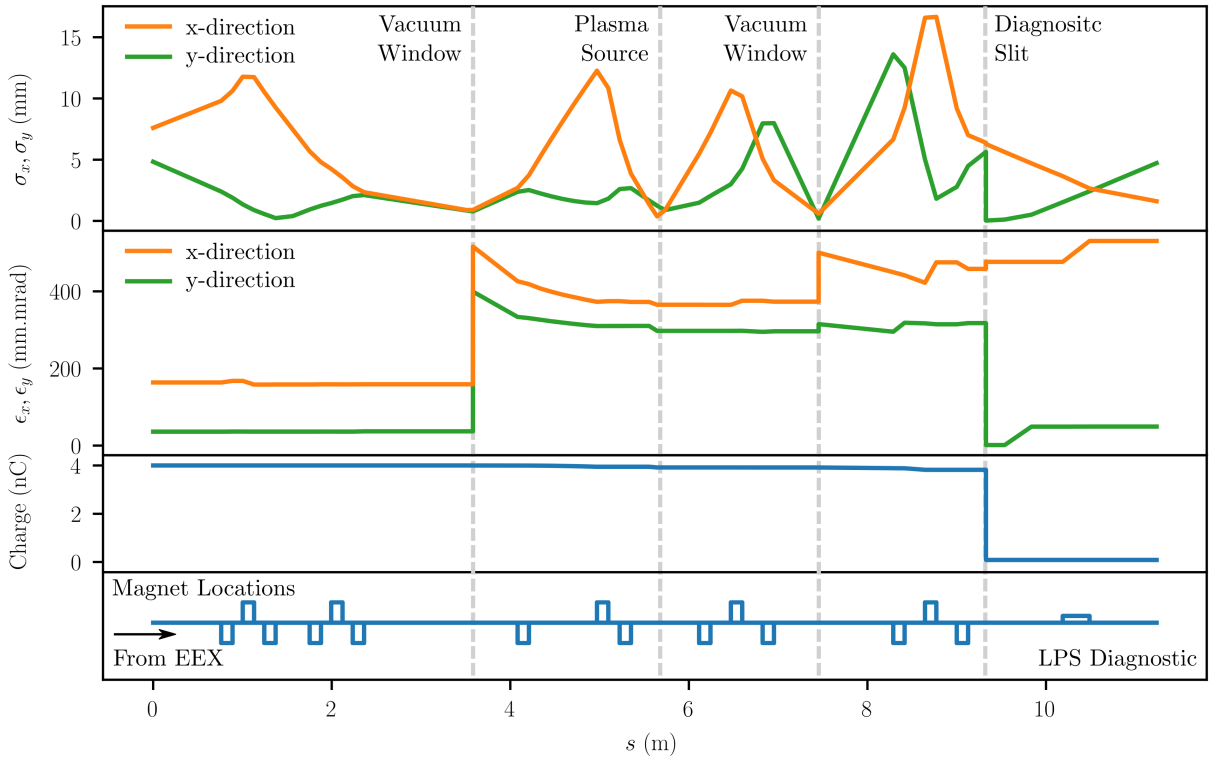

Figure 5.4: Simulated beam dynamics (rms beam size σ, normalized rms. beam emittance ϵ and charge) through the optimized plasma beamline design.

Despite attempts to strongly focus the beam at each Be window, the beam emittance grows significantly. This could have been reduced by placing the second triplet closer to the window, but this was prevented by unmovable components for the future double emittance exchange installation. The elegant model contained hard boundaries equal in diameter to the beamline vacuum components which removed particles that were too far off axis. Hard boundaries for the hollow cathode arc plasma source were also included. In this optimized simulation we see the beam experiences almost no charge losses due to scraping until the beam reaches our LPS diagnostic horizontal slit. It is expected however, that due to real-life

changes in the beam and misalignment issues we will lose some charge in the horizontal direction at each size maxima.

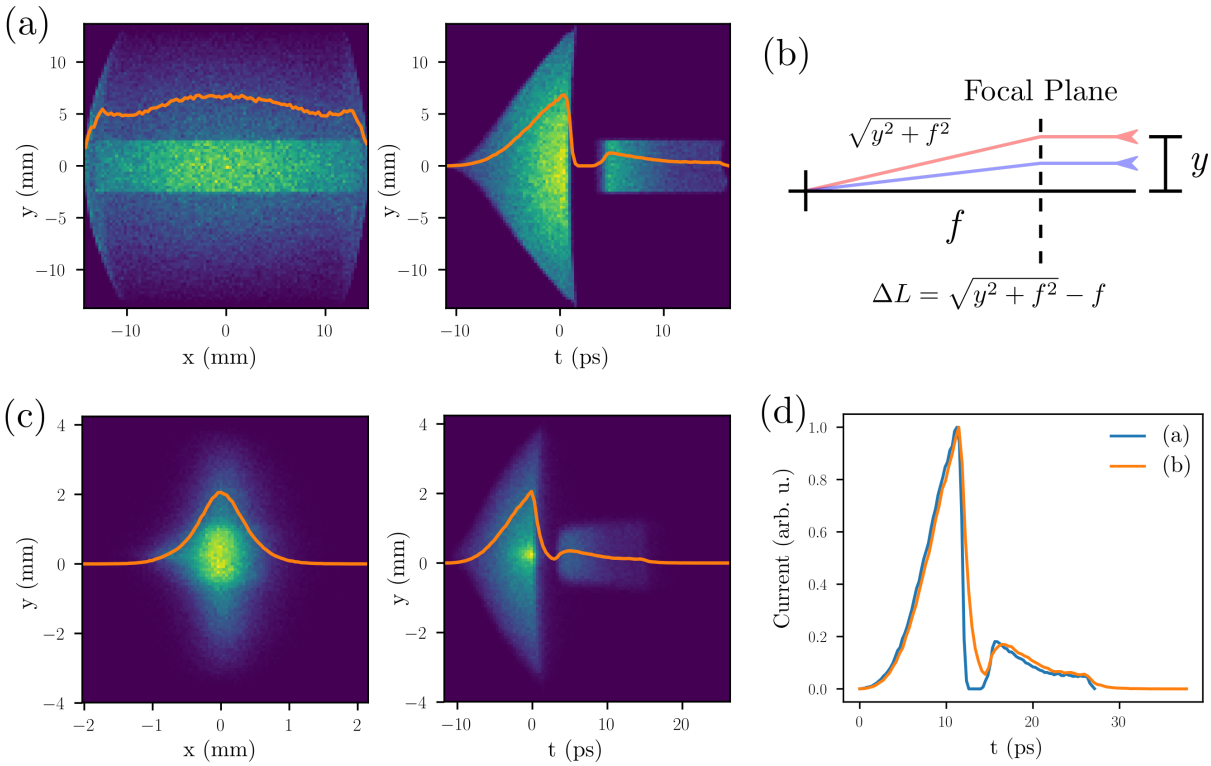

Figure 5.5: Simulated transverse and longitudinal beam cross section at the EEX beamline exit (a) and plasma interaction point (c). (b) Diagram showing path length difference for off-axis beam particles. (d) Normalized beam current at measured locations for (a),(b).

As discussed in Chapter 2 the transformer ratio is strongly dependent on any tail features after the linear ramp. Particles in the drive tail load the wakefield slightly, thus reducing the peak accelerating field seen by the witness. Repeated focusing in the plasma beamline might cause path length aberrations that can lead to a tail developing.

If we consider particles traveling on and off axis going through a single, thin lens, focusing element as seen in Fig. 5.5(b) and we assume that particle deviations in the transverse direction y are small compared to the focal length f of the element i.e. $y << f$, we can show that off axis particles lag behind on-axis particles by

$$\Delta t = \frac{\Delta L}{c} = \frac{f}{c}\frac{y^2}{2f^2} = \frac{yy'}{2c}. \tag{5.11}$$

For a strongly convergent beam, where $y_{max} = 15$ mm and $f = 0.1$ m the maximum slippage could be up to 4 ps. Throughout, repeated focusing and defocusing this slippage can build up to a large tail after the linear ramp that itself is only 20 ps long.

If the longitudinal position of particles in a ramp was not correlated to either of the transverse directions this would not be an issue. Unfortunately, as seen from the distribution output from EEX (Fig. 5.5(a)) there is a significant z-y correlation present. This is leftover from masking as the emittance exchange beamline is simply a drift to first order in the EEX beamline. When masking most off-axis particles in the y-direction are at the end of the transverse ramp and results in the largest transverse longitudinal slice of the beam at the back of the ramp.

Figure 5.5(c) shows beam cross-sections after it propagates through three sets of quadrupole triplets to reach the plasma interaction point. A comparison of beam current profiles between the beam before and after transport is shown in Fig 5.5(d). When compared to the original current distribution a clear tail has developed after the ramp in (c) due to this effect.

As particle coordinates in the x-direction do not have this temporal correlation, we can mitigate tail development by choosing the quadrupole signs properly, allowing the beam to grow in x while keeping the beam small in y as seen in the optimized beam evolution (Fig. 5.4).

CHAPTER 6

Experiment Analyses

In this chapter we will discuss wakefield measurements performed using the designed beamline described in the previous chapters. We start with beam measurements around the plasma interaction point, including charge, transverse beam size and emittance. We then describe calibration of the longitudinal phase space diagnostic and systematic centroid offsets due to transverse plasma kicks. We discuss transformer ratio measurement results for two different beam current profiles and show a method of reconstructing the beam profile at the plasma using only wakefield results. Finally, we analyze measurements of several different plasma densities to probe the transition from linear to nonlinear regimes.

6.1 Beam Parameter Measurement at the Plasma IP

During experimentation, several beam parameters at the plasma interaction point (IP) are of interest to improve wakefield interaction quality, which corresponds to the peak acceleration/deceleration of the wakefield and a reduction of beam losses in the plasma. Relevant parameters include the transverse beam size, emittance and bunch charge, which all contribute to making the dense beam required to excite a strong wakefield.

Jitter in the timing systems of the accelerator can lead to strong shot-to-shot variations in beam position, charge and energy, as these attributes are strongly correlated with beam production at the photocathode. To accommodate for this variation, each measurement in this chapter reflects a collection of up to 100 accelerator shots. In order to reduce statistical variation in beam measurement, an average charge was calculated for the collection, and shots that had more than a one sigma deviation in beam charge from the average were discarded.

Transmitted charge through the beamline was measured using integrated current trans-

formers (ICTs). Significant losses at the emittance exchange mask, final focus triplet and plasma source are expected. The exact charge at the interaction point was difficult to measure as ICT's could only be located before and after the plasma source. As significant beam losses happen between these two measurements, we can only hypothesize the beam charge at the IP based on previous measurements, simulations and charge data collected on either side of the plasma. Previous measurements of focusing before the plasma source was installed and simulation of the beamline suggest that the beam loses about 25% of its charge in the first final focus triplet and none afterwards. Measured charge before the final focus triplet was 2.5 ± 0.2 nC and taking into account beam loss at the final focus triplet we estimate that the charge at the IP was 1.8 ± 0.2 nC. This is consistent with measurements of the beam charge after the post-plasma source triplet of 1.4 ± 0.1 nC as we expect further losses due to scattered particles from the plasma interaction and clipping of the beam observed at the YAG after the plasma source exit. As this measurement does not factor into our transformer ratio observation directly, an order of magnitude estimate of the IP beam charge is sufficient.

As discussed in Chapter 5, optical transition radiation (OTR) was used to image our beam in the plasma source inter-electrode space. An example beam image from the OTR screen is shown in Fig. 6.1. The physical size of each image pixel is calculated from the known diameter of the OTR mirror. Based on this, the rms beam size was calculated to be $\sigma_x = 900 \pm 72$µm, $\sigma_y = 465 \pm 16$ µm.

The last measurement of beam properties near the IP is transverse beam emittance. Along with a measurement of the spot size, we can use this to estimate the betatron function at the IP. As discussed previously in Chapter 2 if the beam betatron function at the plasma interaction point $\beta^* = \sigma_x^2/\epsilon_x$ matches the equilibrium betatron function for a given plasma density, the beam size will stays constant inside the plasma channel. This increases stability of the longitudinal wakefield and reduces emittance growth, thus improving the overall measurement.

We measure the beam emittance by directly measuring the beam size at the vacuum windows. From chapter 5 if we assume that the beam waist is at the window, such that the beam has no x-x' correlation, then the total beam emittance is given by

$$\epsilon_x^2 = \sigma_x^2 \sigma_{x'}^2 = \sigma_x^2(\sigma_{x',i}^2 + \sigma_\xi^2) \tag{6.1}$$

If we further assume that emittance contributions due to the vacuum window are much larger

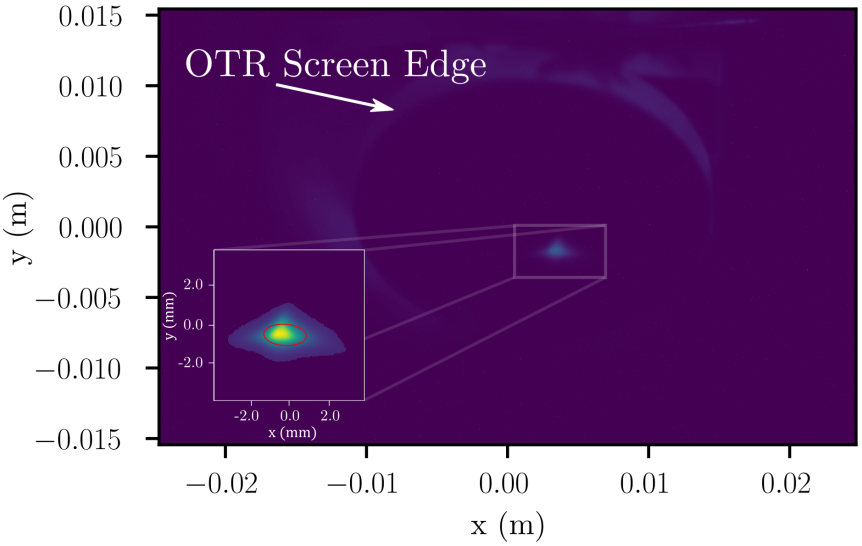

Figure 6.1: Spatially calibrated OTR radiation image showing transverse beam profile on OTR mirror. The mirror edge is seen due to Cherenkov radiation emitted from electrons traveling through the dielectric mirror substrate.

than any other source, then we can estimate the emittance by measuring beam size at the window. These are reasonable assumptions as the windows are thick enough to contribute greatly to the emittance due to their 125 µm thickness. We attempted to minimize the beam size at the window by minimizing the spot at a nearby YAG screen. However, since the waist is located at the YAG, not the window itself, we expect that the beam size is larger at the window location then measured at the YAG. Not only does this increase our overall emittance growth, it also underestimates emittance after the window.

Location	σ_x (mm)	σ_y (mm)	ϵ_x (mm-mrad)	ϵ_y (mm-mrad)
1^{st} window	5.50 ± 0.12	5.58 ± 0.10	24.6	25.0
2^{nd} window	2.50 ± 0.08	2.60 ± 0.20	11.2	11.5

Table 6.1: Beam sizes and corresponding emittance estimations for beams after the two vacuum windows. Note: Emittance estimates have significantly larger unknown systematic errors than statistical error from beam jitter.

Estimated emittance measurements after both mirrors shows a significant discrepancy with simulation, most likely due to systematic errors in beamline tuning (beamline element

misalignment, higher order terms in the photoinjector etc.). The large emittance measured explains the discrepancy between simulation and experiment when looking at charge loss. As seen in Chapter 5, we were able to tune the beamline such that no charge was lost before the horizontal slit. However, during experiment the maximum charge transmission through the plasma source was roughly 75%. This discrepancy is most likely due to larger beam sizes in the plasma focusing quadrupoles, which scrape the beamline walls. Beam loss also accounts for the lower emittance measured at the second window, as particles away from the beam core in phase space are lost at a higher rate.

From this measurement we can estimate the betatron function size at the interaction point using the estimated emittance and the OTR spot size measurement. We find $\beta^* \approx 34$ mm which exceeds the matched beta function by only a factor of five. Furthermore, if the real beam emittance is larger than our estimation, the IP beta function shrinks and matches better with the plasma. Having a higher emittance is obviously not ideal as it reduces the strength of our wakefield interaction by increasing the overall size of the beam, thus decreasing the beam density resulting in a smaller wake. This also leads to less beam capture by the plasma bubble region, where the most dominant wakefield forces are felt. We expect that a significant portion of the off-axis beam only weakly interacts with the plasma wakefield, and thus remains at a constant energy and trajectory.

6.2 Wakefield Measurements

Our goal is to use the longitudinal phase space diagnostic to measure the entire beam wakefield due to beam-plasma interaction in a single shot. Previous wakefield measurements [39] use a number of beam shots to sequentially map out the wakefield by measuring energy change of a short witness beam whose distance behind the drive can be scanned. This method assumes a number of experiment parameters such as beam charge and plasma density are constant shot-to-shot. While some stability of the accelerator and plasma source can be assumed, errors in the wakefield measurement due to jitter are expected. A single shot method on the other hand, does not have this issue, as it measures the entire wakefield without any assumptions about stability. While the wakefield for each shot will have some variation due to beam and plasma jitter, a single wakefield measurement can be trusted.

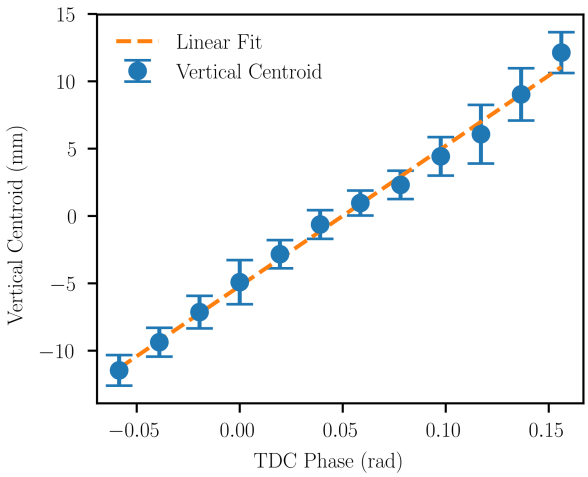

Figure 6.2: Vertical centroid measurements for TDC calibration.

6.2.1 Longitudinal Phase Space Image Calibration

Before using the longitudinal phase space diagnostic, calibration of traverse screen coordinates to longitudinal phase space is necessary. As discussed previously, the single particle transport through the LPS diagnostic is given as

$$x_f = \left(Sd - \frac{(1-C)(1+hTd)}{h}\right)\delta_i \tag{6.2a}$$

$$y_f = \kappa(d_1 + d_2 + L - hT(d_1 d_2 + d_2 L))(ct_i) \tag{6.2b}$$

where $h = 1/\rho_0$ with the dipole bend radius ρ_0, L is the rectangular dipole length, (S, C, T) are $(\sin(\alpha), \cos(\alpha), \tan(\alpha))$ respectively, d_1, d_2 are the distances from the center of the TDC to the dipole edge and the dipole edge to the screen respectively. Parameter κ is the geometric kick strength of the transverse deflecting cavity. Here we neglect error terms associated with phase space coordinates x_i, x_i', y_i, y_i'.

Calibration of the screen in the horizontal direction is relatively simple, as all of the terms are geometric in nature and easily measured if the beam is assumed to be centered on the YAG screen during LPS measurement. We can also cross check this calibration using simulation as the beam central energy is well defined based on transport through the emittance exchange beamline. These calculations resulted in a calibration of 0.014 MeV per pixel. The full screen is roughly 640 pixels in diameter allowing an energy acceptance of $\pm$ 4.48 MeV at the screen center.

Calibration of the screen in the vertical-direction is done experimentally by measuring

beam deflection while scanning the TDC phase with the spectrometer dipole off. Offset of the observed beam centroid should follow linearly with RF phase for small deviations from the zero crossing. To ensure accurate measurement of the deflection, bunch charge was reduced to a few pC to limit emittance growth in the EEX beamline and reduce wakefield effects in the deflecting cavity. Results from this measurement are seen in Fig. 6.2 and the calculated geometric kick strength is $\kappa = 1.84$ m^{-1}. This yields a calibration of 0.084 ps per pixel allowing beams up to 53 ps long too be imaged.

6.2.2 Characterization of Transverse Kicks from the Beam-Plasma Interaction

As we saw in Chapter 4, the plasma discharge current can be upwards of 300 A. If we assume that the current travels through the plasma cross section while the beam is present, then the magnetic field from the discharge current will affect the beam trajectory, if the beam is misaligned slightly with the plasma axis. If we assume a uniform current density cross-section in the plasma, an azimuthal magnetic field appears inside the plasma column calculated by using Ampere's law [50]

$$B_\phi(r) = \mu_0 J_z r = \frac{\mu_0 I_0}{2\pi R^2} r \tag{6.3}$$

where I_0 is the total current and R is the plasma radius. This results in a radial focusing force that can alter the centroid trajectory of the beam if it is off axis or has an incoming angle relative to the plasma axis. As the beam goes through roughly two full betatron periods from plasma to LPS imaging diagnostic, this kick will show up as a centroid offset on the LPS screen.

These transverse centroid offsets from the plasma interaction must be taken into account to accurately measure the beam energy. As our diagnostic relies on the transverse positioning of the beam any changes to the beam centroid between plasma on and off shots will result in a shift of the energy and temporal coordinates of the beam distribution. The horizontal slit prevents any offset in vertical centroid as it does not move during the experiment. It was found that the beam does shift by -0.57 mm in the horizontal direction on the straight ahead screen when the plasma is active. Since the path length from the dipole beginning to the detection screen is equal regardless of whether or not it is turned on, we can assume the horizontal offset is the same.

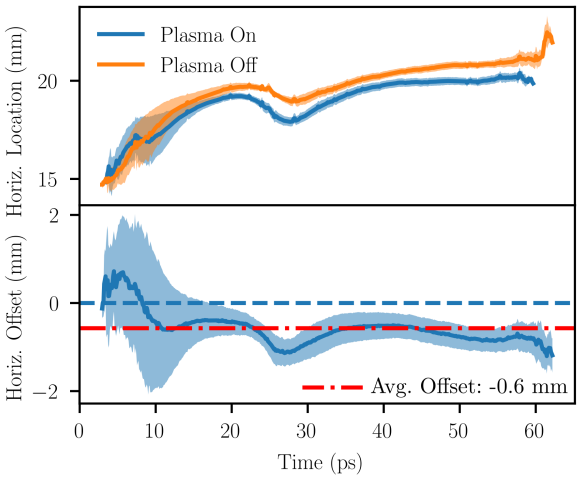

Figure 6.3: (a) Time dependent horizontal centroid of plasma on and off shots with spectrometer off. (b) Measured horizontal offset between plasma on and off shots.

6.2.3 Adaptive Windowing

To calculate the time dependent wakefield we use the LPS diagnostic to find the time dependent energy centroid of the beam $< E(t) >$. If the beam has a phase space distribution of $\rho(t, E)$ this measurement is equivalent to

$$< E(t) >= \int_{-E'_{min}}^{E'_{max}} E'\rho(t, E')dE'. \tag{6.4}$$

When mapped onto the transverse plane inside the LPS diagnostic this becomes equivalent to

$$< x(y) >= \int_{-x'_{min}}^{x'_{max}} x'G(y, x')dx'. \tag{6.5}$$

where $G(y, x)$ is the distribution imaged on the vertical (y) and horizontal (x) axis of the YAG screen.

This measurement can be skewed if a significant portion of our image is background light. Furthermore, since the screen has a round shape, influence from the background light is weighted higher near the screen center. This is due to the vertical size of the screen being larger in the center and thus contributing more background which averages out modulations in the beam centroid.

A simple solution to removing the background is by simply setting a threshold level at the average background pixel brightness and then subtracting this level from the entire image. While this works fine theoretically, in practice choosing the threshold level is difficult and

generally subjective. Moreover, it doesn't completely capture the physics dynamics we are interested in. From simulation studies seen in Chapter 2 we see that the strongest wakefields are present in the beam center. If a significant portion of beam particles are outside of the blowout region they will not see strong accelerating or decelerating fields. When the energy centroid is calculated. These off-axis particles which have not seen any energy change, will mask on-axis particle energy gain or loss. Thresholding cannot be used to fix this problem, as it removes the most accelerated particles, which are small in number, due to strong defocusing forces near the peak accelerating point.

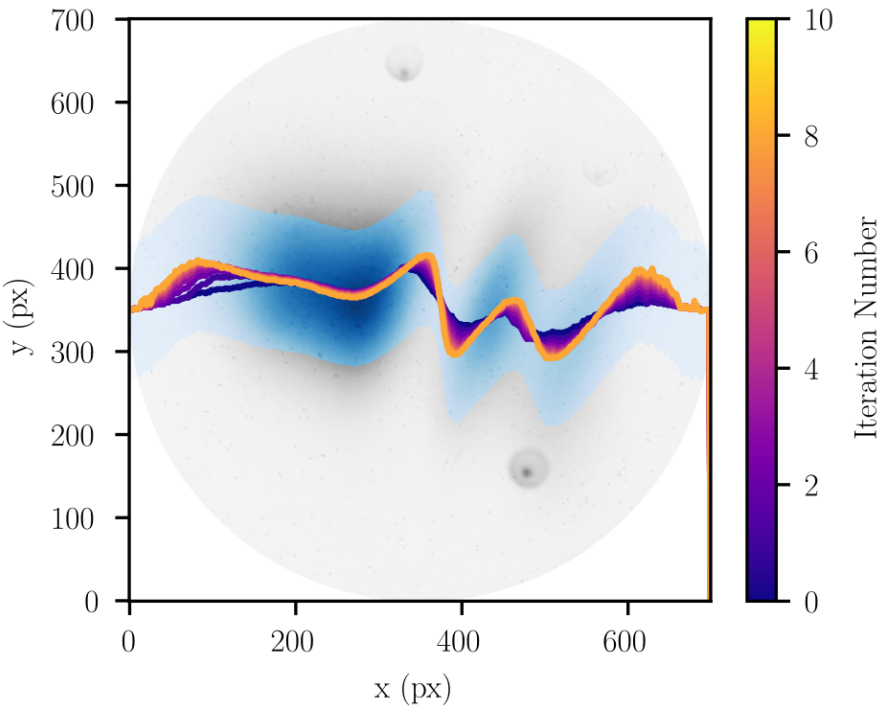

Figure 6.4: A plot showing the iterative windowing procedure. The original longitudinal phase space image is seen in gray-scale. Time dependent (x-axis) calculated energy (y-axis) centroids for each iteration are plotted as well as the final beam image in blue-scale after iterations converge.

To accurately represent the energy distribution of particles on axis, we implemented an iterative method of masking the distribution in the energy direction (y)[1]. Starting with the original $n \times m$ image array where each individual pixel has an integer value $I_{n,m}$, the initial

[1]To match previous ways of formatting wakefield graphics with time on the horizontal axis, beam images here have been rotated 90 degrees.

weighted average $f_{0,n}$ is calculated to be

$$f_{0,n} = \sum_m \frac{mI_{n,m}}{I_{n,m}} \tag{6.6}$$

for each column. A vertical window of width $2d_0$ is created, where image pixels greater than a distance d_0 away from the centroid are set to zero, creating a new image array I_1. The weighted average was then recalculated for the windowed array

$$f_{1,n} = \sum_m \frac{mI_1}{I_1} \tag{6.7}$$

and the masking process was then repeated with a new distance given by

$$d_i = d_{i-1}\left[1 - A\frac{\sum_n |f_{i,n} - f_{i-1,n}|}{\sum_n f_{i,n}}\right] \tag{6.8}$$

where A is a scaling strength parameter (set to 20 in this case) that dictates how aggressively the window is shrunk between successive iterations. The new distance decreases fractionally with the normalized difference between the centroid before and after the windowing step. As $f_{i,n}$ starts to match $f_{i-1,n}$ the change in window size decreases until it no longer changes the centroid, for which we say the windowing has converged.

An example of this process is shown in Figure 6.4. The initial beam image (shown in gray-scale) is a raw image captured from the LPS diagnostic screen with plasma source discharging active. The initial calculated centroid is shown in dark blue (iteration number 0). As the iterative process slowly reduces the window size we begin to observe sharper features in the beam distribution until successive centroids converge, around iteration 8. The final windowed image (shown in blue) ignores most of the background region by only cutting off particles that are far off axis. We also observe that undulations in the centroids, which correspond to changes in the slice energy centroid, increase in amplitude as off-axis particles are cut, consistent with our predictions and simulation results.

6.2.4 Plasma Off LPS Measurement

We characterized the beam longitudinal phase space without any plasma interaction as a background measurement. This is significant especially at AWA due to the strong coupling between transverse and longitudinal phase spaces. Normally, temporal jitter in linear accelerators is easily accounted for via proper triggering, or below temporal tolerances as small

deviations in energy from phase errors in RF systems do not create issues in accelerators without bends. In this case though, temporal jitter leading to energy deviations causes significant angular jitter in the plasma beamline due to the EEX process. Furthermore, during experimentation the RF phase would drift over a time scale of about 5-10 minutes. This required constant steering corrections in order to maintain proper alignment through the plasma source. In order to take jitter into account, a number of shots were taken over a short period of time during each experiment and the overall variance in shots was calculated.

Figure 6.5 shows longitudinal phase space measurement of the beam without plasma interaction. A number of images were collected, along with corresponding beam charge at ICT locations throughout the beamline. As mentioned earlier, shots that had measured charge outside one sigma deviation from the mean were discarded. For each remaining shot, the time dependent energy centroid was calculated and an average profile with time dependent variance was found for the collection, seen in Fig. 6.5.

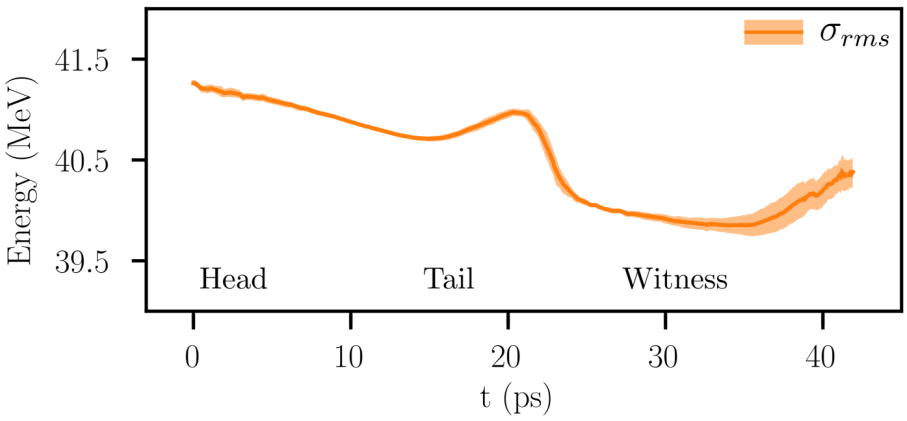

Figure 6.5: Charge windowed, mean time dependent energy centroid of plasma off shots (38 shots) with time dependent rms variation (shading).

From our measurement of the average time slice energy centroid we observe a longitudinal energy chirp, which is a result of the emittance exchange process due to the longitudinal energy kick of off-axis particles in the EEX transverse deflecting cavity. An energy hump observed at t = 20 ps is likely a consequence of phase slippage from the ramp tail, as these particles have similar energy to those who remain in the ramp and is observed to a lesser extent in previous wakefield measurements [40]. This feature will be subtracted away during

wakefield calculations as it is independent of the plasma interaction to first order[2].

The shaded region in Figure 6.5 captures the rms variance in the beam centroid over 34 shots. This region characterizes the net jitter of the accelerator, capturing sources of transverse and longitudinal jitter due to strong coupling. When compared to plasma on shots, this in turn will be the time dependent error of the wakefield amplitude. Despite the complexities of our experimental beamline and the large number of sources for jitter, the measured longitudinal phase space centroid is fairly stable, which will result in small errors for our wakefield calculation.

6.2.5 Plasma On LPS Measurement

We now turn to measurement of the longitudinal phase space when the plasma is active. Analyses of these measurements are similar to those previously discussed. The main difference is that we consider each shot independent of one another. As we saw in the previous measurement, taking a statistical average and spread of the centroid measured accelerator stability. If we were to do the same for plasma "on" measurements, the accelerator jitter would be convolved with discharge stability. As we are not interested in measuring overall stability of the system, we treat each plasma on shot as an independent experiment and assume that some shots will contain closer to an ideal interaction. Our long, low charge, witness beam allows us to characterize the multi-period wakefield for each individual experiment independently, thus allowing a unique transformer measurement for each shot.

In order to accurately compare plasma on measurements to the measured centroid background (plasma "off" average) we interlaced plasma "on" and "off" shots. During experimentation, various parameters of the accelerator would slowly drift over several minutes, most notably laser timing relative to the RF phase. Normally, in dispersionless beamlines, small drifts in the laser phase are acceptable (< 1 deg) and only lead to deviations in centroid beam energy. Timing drift becomes more difficult to handle when dispersion is present and when RF cavities run off crest, which results in larger energy deviations from timing errors. This leads to transverse alignment issues, which are particularly detrimental in our beamline, as it contains a number of tight apertures and alignment with the plasma column is

[2]Higher order effects, such as differences in the transverse transport of the beam slice due to the slightly increased energy.

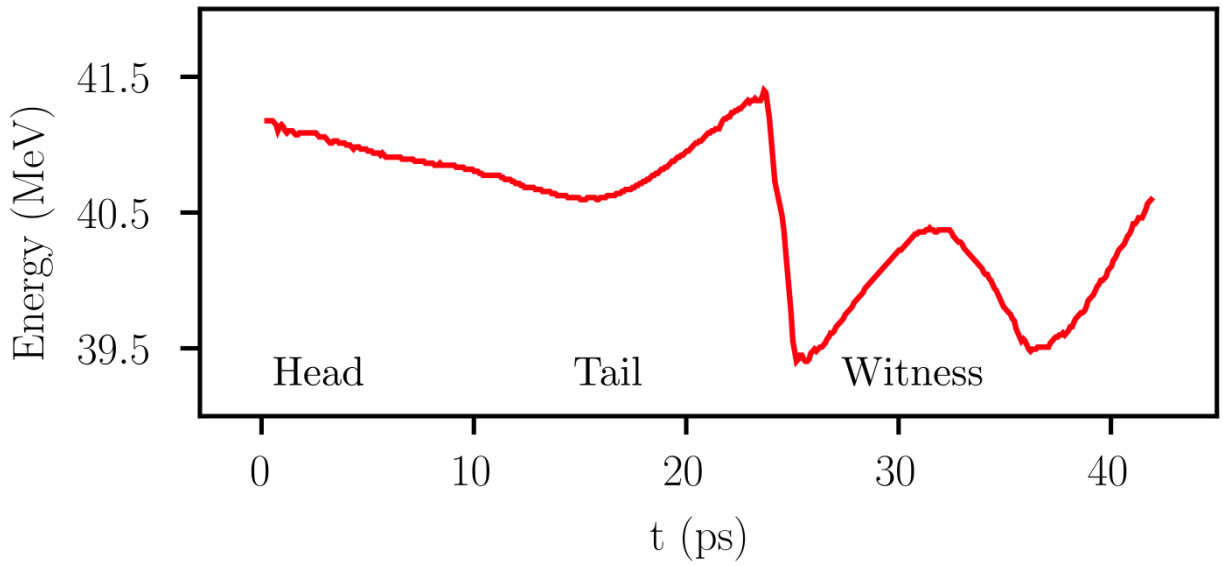

Figure 6.6: Time dependent energy centroid of single plasma "on" shot.

critical to supporting a successful wakefield interaction. Interlacing plasma on and off shots allows experimental and background measurements to be done simultaneously, reducing drift contributions when we subtract the plasma "off" background from our "on" shots.

An example of a plasma "on" measurement is shown in Figure 6.6. The beam energy is clearly modulated temporally as is evidenced by the centroid energy. To calculate the wakefield profile we will measure the energy difference between plasma "on" and plasma "off" shots. Modulation in the beam energy from the wakefield over the interaction length $0 < z <= L$ can be given as

$$\Delta E(\xi) = \int_L eW_z(z,\xi)dz. \tag{6.9}$$

In the quasi-static approximation, the wakefield remains static in the moving frame over the interaction length, thus $W_z(z,\xi) = W_z(\xi)$ and the energy gain simply equals $\Delta E(\xi) = LeW_z(\xi)$.

The real plasma will have a somewhat different effect on the beam energy centroid due to a non-uniform plasma density profile. In this case we cannot assume a quasi-static picture of the wakefield as it propagates through the plasma, so measurement energy gain of the beam is effectively an averaged wakefield contribution over the entire plasma distribution. This is not an issue however, because we previously saw, the wakefield changes over time, even in an uniform plasma region due to beam profile evolution. Furthermore, this method of wakefield measurement is closer to applicable systems as we are concerned with the final

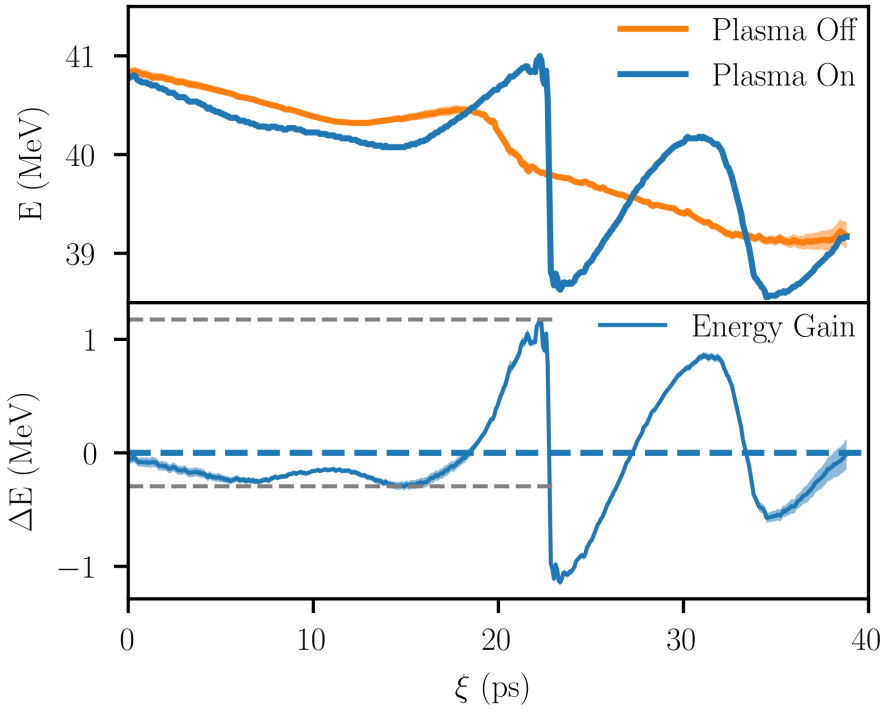

Figure 6.7: Top: Time dependent energy centroid background and plasma on shot plotted together. Bottom: Plasma energy gain calculated by subtracting background centroid from plasma "on" centroid.

energy distribution of the beam anyways.

The averaged wakefield is thus calculated by

$$< eW_z(t) >= (< E(t) >_{\text{plasma on}} - < y_{\text{kick}} >) - < E(t) >_{\text{plasma off}} \tag{6.10}$$

where $< y_{\text{kick}} >$ is the average centroid offset due to the discharge current focusing kick. A comparison between the background time dependent energy centroid and a plasma on shot is shown in Fig. 6.7. In this case the single triangle mask was used and the solenoid current was set to 50 A. Based on triple Langmuir probe measurements from Chapter 4 we expect an average plasma density of 0.4×10^{14} cm^{-3}.

The measured centroid energy perturbation to the plasma on beam can be used as a check for consistency in our longitudinal phase space analysis. We observe that the beam head experiences no energy gain or loss which is consistent with causality arguments laid out in Chapter 2. This is a check on correctly subtracting horizontal offsets due to transverse kicks by the beam-plasma interaction. Errors in this regard would show up as a non-zero

offset in the energy gain at the beam head.

We can also use the wakefield to estimate the average plasma density. The periodic structure of the wakefield should match the plasma frequency $\omega_p = \sqrt{n_0 e^2/4\pi m^* \epsilon_0}$ which, in the linear case where the effective mass $m^* = m_e$, only depends on the plasma density n_0. However, if the plasma electrons in the wakefield become relativistic, their effective mass will increase, thus reducing the modulation frequency. While we cannot exactly measure the relativistic factor of plasma electrons in our interaction, based on our analysis of simulations shown in Chapter 2 we can guess that deviation from the linear frequency due to this effect is small.

6.2.6 A Note Regarding Beam Current Measurement

At first examination, it seems trivial to use the LPS diagnostic to measure the beam current profile simply by looking at the projection of the beam distribution onto the temporal axis. Our use of slitting means that we only see a small portion of the beam projected onto the diagnostic screen. This would not be an issue normally, as the beam current is roughly uniform transversely. However, as we saw in Chapter 5 the beam we are dealing with has a strong z-y correlation. Most particles that contribute to our beam having a ramped profile are actually off axis and do not make it through the horizontal slit. This prevents an accurate measurement of the beam current due to this correlation.

An example of this effect is seen in Figure 6.8. Here we see a collection of beam current measurements using a projection of the beam image at the LPS diagnostic onto the vertical (time) axis. For both cases we see the development of a long tail after the drive ramp, such that the beam current does not completely go to zero in between the drive and witness beams which is consistent with predictions from beamline simulations (see Chapter 2). Looking at the plasma "off" case, we see a strong shot-to-shot variation in the measured drive beam current when compared to variation seen in the witness. We also see a reduction in the ratios of peak current in the drive and witness bunches when compared to the transverse beam projection from the EEX mask from about 4 to 2. Asymmetry between the drive and witness bunch current reduction and variation could be attributed to several factors, all due to the larger transverse beam size of the drive beam relative to the witness. We could imagine that as the beam centroid jitters transversely as it travels through the beam pipe or

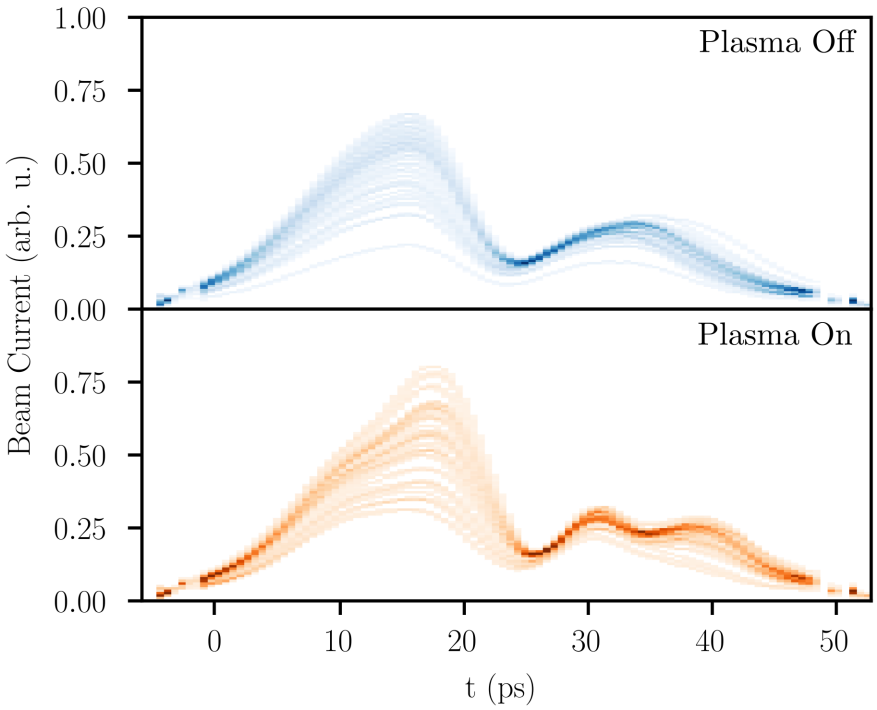

Figure 6.8: Density of beam current measurements for 50 plasma "off" and 50 plasma "on" shots. The vertical axis for each graph is normalized by the same factor and the time axis is shifted to match Figure 6.7.

at the horizontal mask, then the large drive bunch will lose more particles than the smaller witness.

We can also compare the beam currents between when the plasma is on or off. We observe a significant difference in the witness current when the plasma is active. The minima observed at $t \approx 34$ ps corresponds to the negative zero crossing in Figure 6.7. This current reduction be explained by on-axis defocusing fields when the secondary bubble collapses as seen from simulation results.

In the drive beam, we also can see a qualitative change in the beam current distribution. The drive shows a distinct, linear region near the peak current density, regardless of measurement jitter. One potential explanation for this effect is due to particles exiting the plasma bubble during the beam-plasma interaction. Particles that exit the rarefaction region do not experience any transverse focusing forces and can be lost during beam transport to the diagnostic. This particle loss is in addition to losses experienced by a beam not interacting with the plasma. We can also observe a slight overall increase in total drive bunch charge

(as each graph is normalized by the same factor) when the plasma is on. This might be due to slight focusing created by the beam-plasma interaction. Further study would be required to measure and verify hypothesis stated here.

6.2.7 Current Reconstruction

From analysis in the previous section, it is unlikely that a measurement of the beam current at the LPS diagnostic correctly predicts the beam profile at the plasma interaction point. Nevertheless, we would like a different method of predicting the beam current profile in order to provide context for our wakefield measurements.

We can try to get a reconstruction of the longitudinal beam profile by using the measured wakefield response in the linear regime. We previously calculated a linear perturbation to the plasma density from a symmetric electron bunch in Section 2.1. The plasma response is given by Eqn. 2.34

$$\frac{\partial^2 n_1}{\partial \xi^2} + k_p^2 n_1 = -k_p^2 n_b \tag{6.11}$$

where we found the plasma perturbation to be

$$n_1(r,\xi) = \begin{cases} 0 & \xi < 0 \\ -k_p \sigma(r) \int_\xi^\infty \sin(k_p(\xi' - \xi)) d\xi' & \xi > 0. \end{cases} \tag{6.12}$$

It can be shown that for any given transverse beam distribution $\sigma(r)$ that is rotationally symmetric, the transverse electric field on axis is $E_r(r = 0, \xi)$. From this, Gauss's law on-axis reduces to

$$\nabla \cdot \mathbf{E} = \frac{dE(0,\xi)}{d\xi} = \frac{e}{\epsilon_0}(n_b + n_1) \tag{6.13}$$

We can then combine this equation with Eqn. 2.34 and remove the radial form factor to get

$$\frac{dE(\xi)}{d\xi} = -\frac{e}{\epsilon_0 k_p^2}\frac{d^2 n_1}{d\xi^2} \tag{6.14}$$

Integrating from $-\infty$ to ξ gives

$$\frac{dn_1(\xi)}{d\xi} = -\frac{k_p^2 \epsilon_0}{e}[E(\xi) - E(-\infty)] = -\frac{k_p^2 \epsilon_0}{e} E(\xi) \tag{6.15}$$

where $E(-\infty) = 0$ because of causality (wakefield is zero before beam starts at $\xi = 0$). Integrating again we get

$$n_1(\xi) = -\frac{k_p^2 \epsilon_0}{e} \int_{-\infty}^{\xi} E(\xi') d\xi' \tag{6.16}$$

plugging this in and then solving for the beam density in Eqn. 6.13 we get

$$n_b(\xi) = \frac{\epsilon_0}{e}\left[\frac{dE(\xi)}{d\xi} + k_p^2 \int_{-\infty}^{\xi} E(\xi')d\xi'\right] \tag{6.17}$$

The resulting equation for beam density (up to a radial form factor) is solely a function of our observed wakefield. Verification of this method was done though a numerical calculation using several different drive beam current profiles seen in Fig. 6.9. For each case, the wakefield was calculated according to linear wakefield theory and the normalized drive current was calculated with Eqn. 6.17. We see that the reconstruction method (orange, dashed

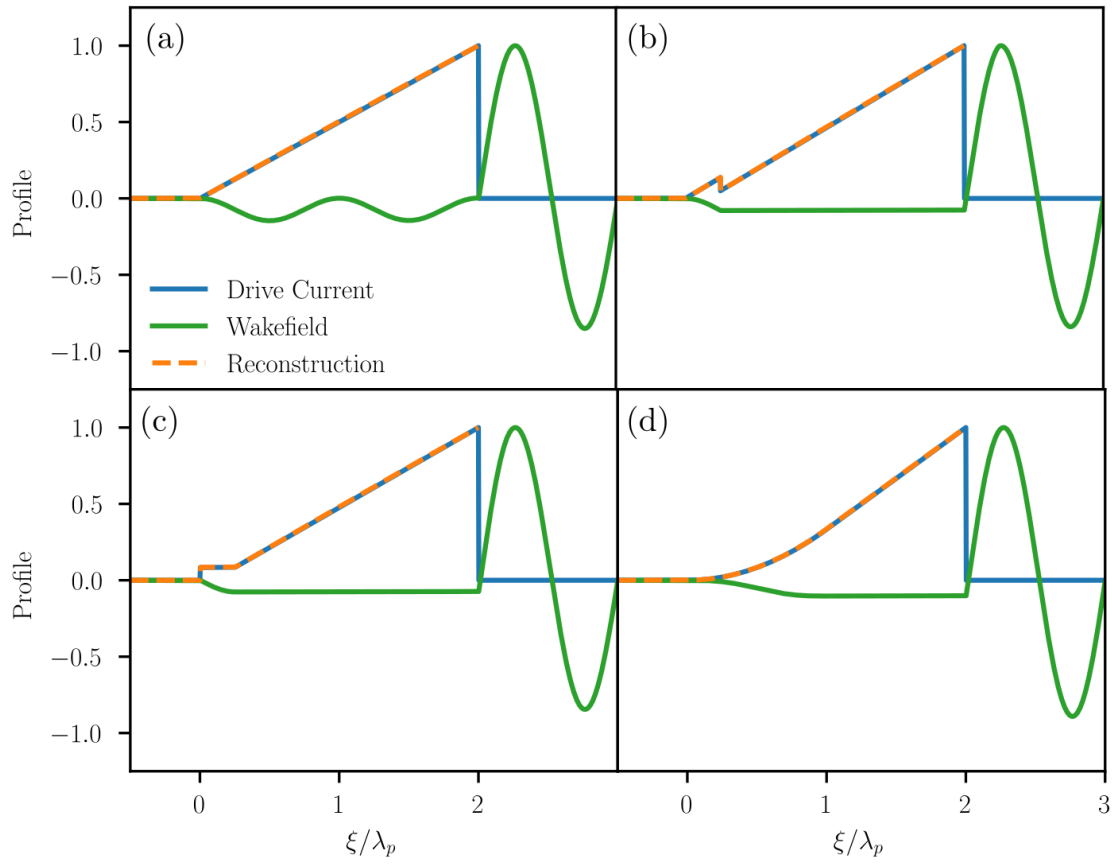

Figure 6.9: Normalized drive current (blue), single mode longitudinal wakefield (green) and reconstruction (orange, dashed) for (a) single triangle, (b) double triangle, (c) doorstep, and (d) parabolic head drive profiles.

line) perfectly predicts the input drive beam current (blue line) including non-differentiable features such as the double triangle and the doorstep. In order to use this method for analysis of our experimental results, the wakefield must have a linear, single mode response. To justify its use for a blowout plasma wake, we return to our analysis in Section 2.4.1,

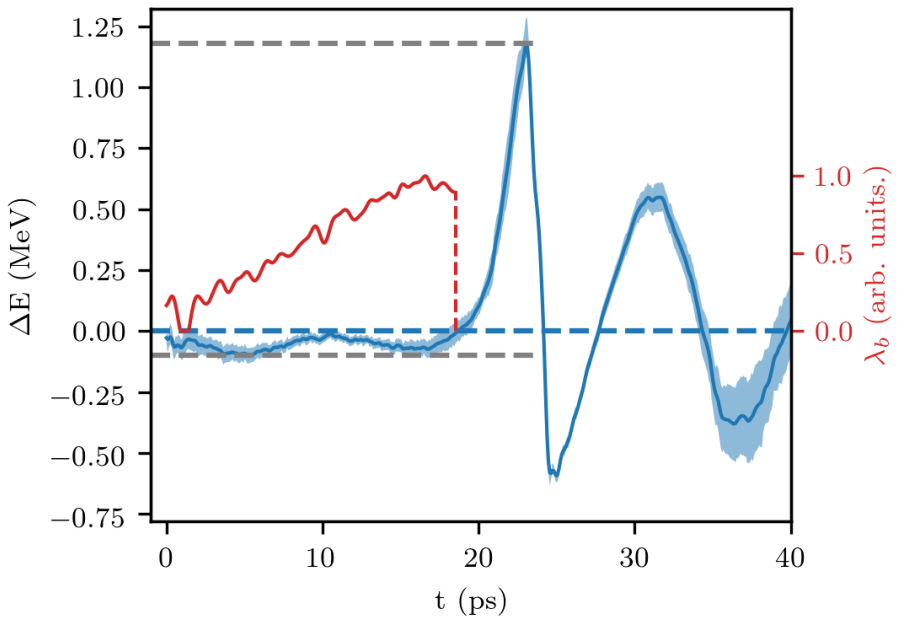

Figure 6.10: Wakefield measurement showing highest transformer ratio observed along with linear beam current reconstruction.

where we saw that because our blowout is non-relativistic we can approximate the wakefield response as linear. Based on simulations with the appropriate beam parameters that match observations, this is indeed the case. Furthermore, the observed wakefield inside the drive in Figure 6.7 closely resembles a linear response.

6.3 Wakefield Measurement Results

We will now discuss the results of using the single shot wakefield measurement and current reconstruction methods. Here we examine two individual wakefield measurements, (1) a measurement that shows the highest transformer ratio observed and (2) a measurement that shows wakefield flattening in the drive. We will then discuss a comparative measurement when we change the plasma density to examine multi-period non-linear effects.

6.3.1 Maximum Transformer Ratio

We first examine the maximum transformer ratio observed. The measured wakefield, along with its reconstructed profile is seen in Fig. 6.10. This measurement took place using the single triangle mask with the plasma source solenoid current set to 50A. The wakefield we

see in the drive from t=0 to t=19 ps is characteristic of a linear response to a ramped beam, as seen by the reconstruction. There are two undulations in the drive wakefield with a return to almost zero in-between, which corresponds to a drive length that extends over two plasma wavelengths. When a linear regime is assumed in this region, we can calculate the plasma density by measuring width between the two minima in the wake. Here separation is 10 ps, which corresponds to a plasma density of 1.3×10^{14} cm^{-3}. This is off by a factor of three, when compared to triple Langmuir probe plasma density measurements for this solenoid current (0.4×10^{14} cm^{-3}). Our discrepancy might be a result of systematic errors in the triple probe measurement, or this could be due to changes in wakefield wavelength due to relativistic mass increases (see Chapter 2). A better argument could be made for the former, as we have already established that systematics of the triple probe measurement gave us a much higher electron temperature than expected, which in turn decreases our apparent plasma density. Furthermore, the relativistic argument is inconsistent with our simulations, which show a relatively weak blowout that implies the particles are sub-relativistic.

Wakefield behavior after the drive beam shows strongly nonlinear components. Calculations of the analytical wakefield after the drive show a purely sinusoidal dependence on ξ. Here, the wakefield behind the drive shows a sharp spike directly after the drive due to a large plasma density spike at that location. We also observe sawtooth like behavior between the first and second maxima is characteristic of nonlinear response, as it starts to develop a number of harmonics previously observed [39].

Furthermore, we can also examine the wakefield response amplitude to support the argument for nonlinearity. We observe that the maximum accelerating wake is larger in amplitude than the largest decelerating wake by roughly a factor of two. This asymmetry can be attributed to asymmetries in plasma density deviations from the mean. Positive excursions of the plasma density in this region are much larger than the negative excursions as the plasma cannot supply anymore electrons. Finally, the magnitude of further oscillations in the wakefield slowly decreases due to beam loading by the witness.

The transformer ratio of this averaged wakefield is measured by taking the ratio of the maximum positive centroid energy change to the maximum negative energy deviation, shown by the dotted gray lines in Fig. 6.10. Error in the transformer ratio is given by taking this ratio for both positive and negative time dependent error bars (shaded regions). For this

measurement the transformer ratio is $7.8^{+2.5}_{-1.7}$ which is significantly higher than calculated TR in the linear (single mode) regime. An ideal current ramp over two plasma wavelengths should give a transformer ratio of 2π. As when have seen, our beam develops a tail due to focusing in the plasma line and reduces TR due to partial wakefield loading.

As we showed previously, this discrepancy in TR is expected. The addition of higher harmonics in the wakefield due to nontrivial density perturbations increases the transformer ratio substantially. This increase in TR mirrors the rationale for introducing the nonlinear regime for plasma accelerators in order to increase TR for Gaussian beams. We will systematically examine this effect later by measuring wakefields from different plasma densities while maintaining the same beam attributes.

6.3.2 Uniformization of Drive Wakefield

The next case we will examine is a measurement where wakefield flattening is observed in the drive. It was shown previously that fully flattening the wakefield leads to the highest transformer ratio. It also limits energy spread in the drive beam due to wakefield decelerating forces. This has a number of benefits, as it allows a longer interaction length without partial dephasing of the drive when it nears full energy depletion. Lemerey and Piot have collected a number of different current distributions that achieve this uniformiztion effect [47]. We observed one of those cases here.

An observation of wakefield flattening is shown in Fig. 6.11. The beam shows a small drop in the centroid energy difference and then flattens out for a period, until the drive beam ceases. By looking at the reconstruction, we can see the cause of this effect is a quadratic ramp perturbation to the linear profile with a length of 6.9 ps. This is consistent with analytical predictions of the wakefield structure [47], as the quadratic head region flattens the decelerating field when its length is an integer multiple of the plasma wavelength. This was measured by looking at wakefield zero crossings in the witness, as there are no undulations able to be measured in the drive. For Figure 6.11, the wavelength was calculated to be 8.9 ps, corresponding to a plasma density of 1.6×10^{14} cm^{-3}. This differs from the parabolic head length by about 25%, which explains why the wakefield is not perfectly flat in the drive.

Here the transformer ratio is measured to be 5.5. This is noticeably lower than the transformer ratio measured when the beam current didn't have the parabolic head, which by

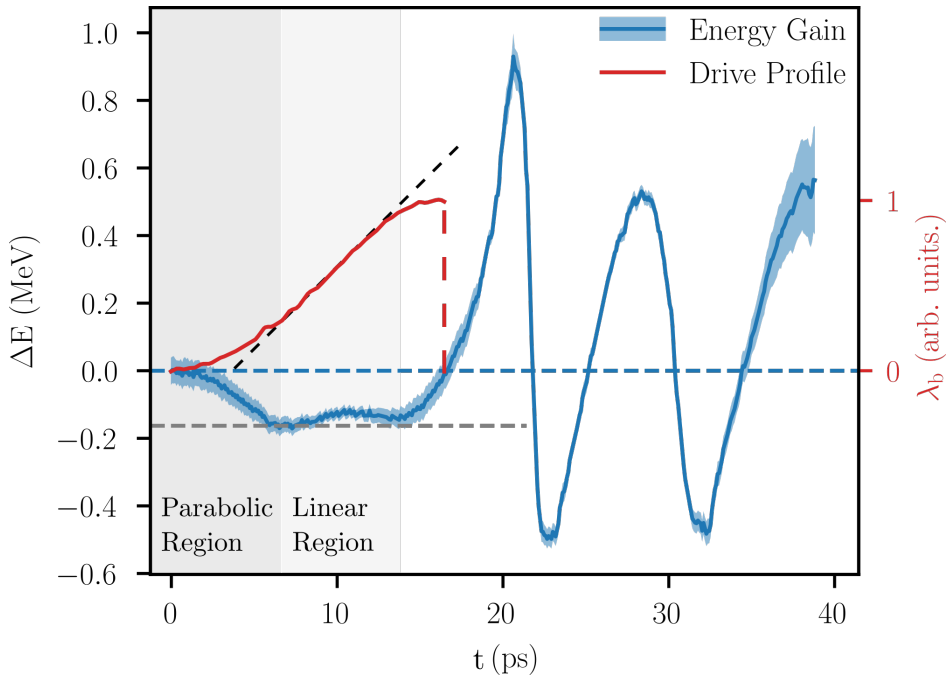

Figure 6.11: Wakefield measurement showing partial wakefield flattening in the drive due to a quadratic perturbation of the drive head.

itself is unexpected, as TR is maximized when the drive wakefield is uniform. It's interesting to note that the maximum negative deviation in drive energy is roughly the same as in the ultra-high TR case, accounting for a slight difference in plasma density which would lead to a proportional change in the wakefield. A constant decelerating field amplitude is understandable, as due to causality, the wakefield does not know the beam current behind it. This must mean that the difference in TR is due to a higher accelerating field in the witness. When we consider that the drive beam region that experiences a uniform field is relatively small, it is understandable that the accelerating field is not as strong as the high TR case. We also see that the reconstructed profile has a significant roll off near the peak which, as we have seen previously, loads the accelerating wake and reduces the peak transformer ratio.

6.3.3 Probing the Nonlinear Wakefield Response

We can also study the dependence of nonlinearities in PWFA by tuning the plasma source density while maintaining the same beam current. A reduction of the plasma density increases the nonlinearity parameter given by

$$\tilde{Q} \equiv \frac{N_b k_p^3}{n_0} = 4\pi r_e k_p N_b \tag{6.18}$$

where N_b is the beam charge and $k_p = 2\pi/\lambda_p$ is the plasma wavenumber. If $\tilde{Q} << 1$ the beam charge in a cubic skin depth is less than the plasma density and the response is linear. Conversely if $\tilde{Q} > 1$ then the beam has a higher density and the plasma wakefield response is highly nonlinear.

The plasma source density was tuned by changing the confinement solenoid current, which significantly changes the plasma density as measured by triple Langmuir probe. We started by collecting a number of plasma "on" measurements for each solenoid setting. An average wakefield was calculated and shots that deviated strongly from the mean were discarded and the mean recalculated in an iterative process, until only 10 shots remained. This was done to ensure that wakefield characteristics were consistent for each plasma density setting, and not just a result of single-shot jitter.

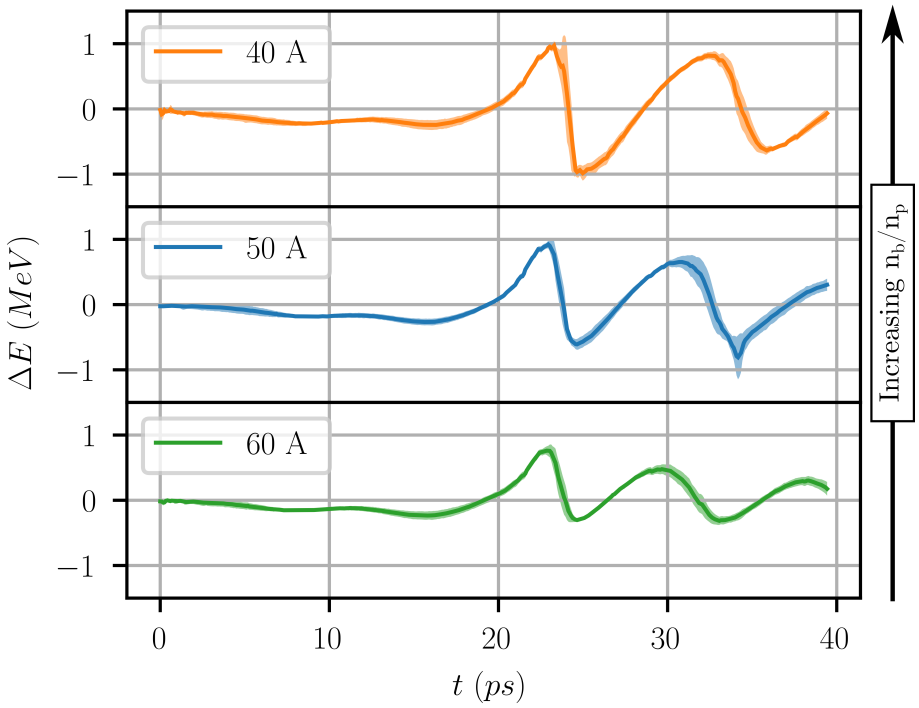

Figure 6.12: Plot showing evolution of the plasma wakefield as the density is scanned via scanning the source solenoid current. Shading shows one-sigma deviation from the average of ten selected shots.

Results from this study are seen in Figure 6.12. Based on triple Langmuir probe measurements, an increase in solenoid current should correspond to an increase in plasma density by a factor of 4. We can immediately see that for the multi-period wakefield, the wavelength

shrinks from ∼10 ps to ∼7 ps. Given that $n \propto 1/\lambda_p^2$ we calculate that the effective plasma density changed by a factor of 2. This discrepancy could either be due to density dependent systematic errors in plasma measurement or it could be due to the nonlinearity itself. We also observe that the overall amplitude of the wakefield decreases as plasma density is increased (or nonlinearity is decreased). This is consistent with analytical predictions [90].

CHAPTER 7

Conclusion

We now conclude this thesis with a summary of experimental accomplishments, their relevance to the broader field of PWFA and the way forward for experiments at Argonne. In this experiment we have used a novel beam shaping technique, emittance exchange, to create longitudinally shaped drive bunches and long, low charge witness bunches to sample the multi-period wakefield response. The beam was then transported to the hollow cathode arc plasma source which itself was extensively tested and characterized to produce a tunable plasma column. The resulting perturbation to the energy distribution due to the plasma interaction was characterized using a longitudinal phase space diagnostic. Our unique, single-shot wakefield measurement was enhanced through the development of a drive current reconstruction technique that allowed us to predict the profile just from the wakefield data and linear plasma theory.

We measured several wakefields created by our precision tuned longitudinal bunch shapes. Our measurement of a beam loaded transformer ratio of 7.8, as of writing, is the highest TR measured for any wakefield accelerator. This exceeds the classical transformer ratio of 2π for an equivalent beam in a single-mode wakefield device [32], such as a dielectric structure or a plasma in the linear response regime. Nonlinearities in the plasma wakefield due to a high charge drive bunch gave rise to multiple harmonics in the acceleration region behind the drive, which allowed a higher TR than expected analytically. Furthermore, we observed near-flattening of the decelerating wakefield inside the drive, if it contained a parabolic head with a length of about one plasma wavelength. Finally, we scanned the plasma density while maintaining the same beam current profile, thus changing the nonlinearity of multi-period wakefields behind the drive.

These experimental results have broad applications to the field of advanced accelerators. As discussed in the introduction, an increase in transformer ratio significantly reduces the

drive beam energy necessary to accelerate a witness beam to a target energy in a single stage wakefield accelerator. This allows access to electrons with energies at the GeV scale, while still maintaining a small facility footprint for drive beam creation. An additional advantage from the use of shaped beams for plasma accelerators in particular is the ease of access to the blowout regime. This regime is often sought after due to its high peak accelerating fields and strong transverse focusing forces. However, for high density plasmas one often has to compress the longitudinal beam size significantly to reach high peak currents (often several kA), leading to its own set of beam-based challenges [91]. We saw that the nonlinear regime can be established over several wakefield periods with a long ramped beam, which adds a design path that reaches the strongly nonlinear regime but does not necessitate strong longitudinal compression.

Results from this experiment also provide a clear path forward for future experiments. Improvements to the vacuum window and plasma source design would allow higher quality measurements by reducing emittance growth and improving plasma interaction. The 125 µm thick mirrors give rise to significant growth in transverse emittance which, in turn, lowers the overall experiment quality due to lower diagnostic resolution and lower plasma wakefields. To improve this a thinner window is needed, which can be achieved by using a sub-5 µm thickness kapton window, mounted on a vacuum gate valve so it does not need the mechanical strength to withstand a 1 atm pressure differential. Improvements to the plasma source could include changes to the overall hollow cathode tube geometry to prevent source downtime and repair. A new plasma density diagnostics system which uses an optical H-line broadening measurement [92], could also be implemented. Finally, beam size diagnostics using the OTR type screen used in this experiment could be integrated into the source, directly before and after the cathode and anode respectively. OTR brightness also corresponds directly to beam charge [89] and can be calibrated externally for measurements at the plasma IP.

Once these improvements are made there a number of experiments that can be done at AWA which expands on work done here. One important beam shaping experiment would be to shape the longitudinal drive profile as done here but then to also shape the witness bunch into a "reverse triangle" where the current decreases linearly along the witness bunch. This has been shown to flatten the accelerating wakefield that is experienced by the witness bunch, thus reducing the final energy spread of the witness [93]. Furthermore, with the introduction

of laser pulse shaping at AWA [94] coupled with extremely high bunch charges from the gun, we could attempt to create a linearly ramped drive with a peak electron density of 100x the plasma density, which as we saw in Section 2.4.1 also flattens the drive deceleration wake due to the relativistic blowout.

The large transverse size of the plasma column, along with tune-ability of the longitudinal density profile and AWA's flat beam generation experiments [95] make testing asymmetric beam-plasma interaction also appealing as an experiment. Other types of plasma sources, such as capillary discharge devices, have very small transverse apertures [96]. This makes it difficult to transport so-called "flat" beams with large emittance ratios between horizontal and vertical axes through the source aperture without losing charge to scraping. The longitudinal plasma density for capillary devices is also difficult to tune, something that is easily done in an HCA device through the use of magnetic confinement. These attributes are ideal for expanding the concept of adiabatic plasma lens focusing [97], where a beam that enters a plasma whose density increases slowly over several betatron oscillation periods becomes strongly focused due to the increase in plasma density. This has never been attempted for flat beams, which has particular relevance for strong focusing in the context of colliders, which use flat beams to increase their collision luminosity [59].

REFERENCES

[1] E. Nasser, *Fundamentals of gaseous ionization and plasma electronics.* Wiley-Interscience, 1971.

[2] S. Chen and T. Sekiguchi, "Instantaneous Direct Display System of Plasma Parameters by Means of Triple Probe," *Journal of Applied Physics*, vol. 36, no. 8, pp. 2363–2375, Aug. 1965. [Online]. Available: http://aip.scitation.org/doi/10.1063/1.1714492

[3] J.-L. Delcroix and A. R. Trindade, "Hollow Cathode Arcs," in *Advances in Electronics and Electron Physics*, L. Marton, Ed. Academic Press, Jan. 1974, vol. 35, pp. 87–190. [Online]. Available: http://www.sciencedirect.com/science/article/pii/S0065253908602814

[4] E. O. Lawrence and M. S. Livingston, "The production of high speed light ions without the use of high voltages," *Physical Review*, vol. 40, no. 1, p. 19, 1932.

[5] J. Arthur, W. Graves, M. Renner, J. Rosenzweig, G. Faigel, Z. Huang, M. Wulff, J. Hajdu, I. Evans, K. Kulander, and others, "Linac coherent light source (LCLS) conceptual design report," Tech. Rep., 2002.

[6] G. Aad, T. Abajyan, B. Abbott, J. Abdallah, S. A. Khalek, A. A. Abdelalim, O. Abdinov, R. Aben, B. Abi, M. Abolins, and others, "Observation of a new particle in the search for the Standard Model Higgs boson with the ATLAS detector at the LHC," *Physics Letters B*, vol. 716, no. 1, pp. 1–29, 2012.

[7] P. F. Dahl, *Flash of the Cathode Rays: A History of JJ Thomson's Electron.* CRC Press, 1997.

[8] D. Wilson, "Rutherford-simple genius," 1983.

[9] W. R. Nitske, *The life of Wilhelm Conrad Rntgen, discoverer of the X ray.* University of Arizona Press Tucson, 1971.

[10] V. Marx, *Structural biology:'seeing'crystals the XFEL way.* Nature Publishing Group, 2014.

[11] J. D. Bozek, "AMO instrumentation for the LCLS X-ray FEL," *The European Physical Journal Special Topics*, vol. 169, no. 1, pp. 129–132, 2009.

[12] F. Krtner, F. Ahr, A.-L. Calendron, H. ankaya, S. Carbajo, G. Chang, G. Cirmi, K. Drner, U. Dorda, A. Fallahi, and others, "AXSIS: Exploring the frontiers in attosecond X-ray science, imaging and spectroscopy," *Nuclear Instruments and Methods in Physics Research Section A: Accelerators, Spectrometers, Detectors and Associated Equipment*, vol. 829, pp. 24–29, 2016.

[13] T. Schultz and M. Vrakking, "Attosecond and XUV physics," *Wiley-VCH Verlag*, vol. 10, p. 9783527677689, 2014.

[14] R. W. Hamm and M. E. Hamm, *Industrial accelerators and their applications.* World Scientific, 2012.

[15] H. Baer, T. Barklow, K. Fujii, Y. Gao, A. Hoang, S. Kanemura, J. List, H. E. Logan, A. Nomerotski, M. Perelstein, and others, "The International linear collider technical design report-volume 2: physics," *arXiv preprint arXiv:1306.6352*, 2013.

[16] A. A. Sokolov and I. M. Ternov, "Synchrotron radiation," *Akademia Nauk SSSR, Moskovskoie Obshchestvo Ispytatelei prirody. Sektsia Fiziki. Sinkhrotron Radiation, Nauka Eds., Moscow, 1966 (Russian title: Sinkhrotronnoie izluchenie), 228 pp.*, 1966.

[17] T. Behnke, J. E. Brau, B. Foster, J. Fuster, M. Harrison, J. M. Paterson, M. Peskin, M. Stanitzki, N. Walker, and H. Yamamoto, "The international linear collider technical design report-volume 1: Executive summary," *arXiv preprint arXiv:1306.6327*, 2013.

[18] M. Banks, *Disappointment as Japan fails to commit to hosting the International Linear Collider*, Apr. 2019. [Online]. Available: https://physicsworld.com/a/disappointment-as-japan-fails-to-commit-to-hosting-the-international-linear-collider/

[19] D. Broemmelsiek, B. Chase, D. Edstrom, E. Harms, J. Leibfritz, S. Nagaitsev, Y. Pischalnikov, A. Romanov, J. Ruan, W. Schappert, and others, "Record high-gradient SRF beam acceleration at Fermilab," *New Journal of Physics*, vol. 20, no. 11, p. 113018, 2018.

[20] R. Schonberg, H. Deruyter, W. Fowkes, W. Johnson, R. Miller, J. Potter, and J. Weaver, "Portable, x-band, linear accelerator systems," *IEEE Transactions on Nuclear Science*, vol. 32, no. 5, pp. 3234–3236, 1985.

[21] K. L. F. Bane, P. B. Wilson, and T. Weiland, "Wake fields and wake field acceleration," in *AIP Conference Proceedings*, vol. 127. AIP, 1985, pp. 875–928. [Online]. Available: http://aip.scitation.org/doi/abs/10.1063/1.35182

[22] S. Casalbuoni, E. Knabbe, J. Ktzler, L. Lilje, L. Von Sawilski, P. Schmueser, and B. Steffen, "Surface superconductivity in niobium for superconducting RF cavities," *Nuclear Instruments and Methods in Physics Research Section A: Accelerators, Spectrometers, Detectors and Associated Equipment*, vol. 538, no. 1-3, pp. 45–64, 2005.

[23] A. Gurevich, "Enhancement of rf breakdown field of superconductors by multilayer coating," *Applied Physics Letters*, vol. 88, no. 1, p. 012511, 2006.

[24] C. Zener, "A theory of the electrical breakdown of solid dielectrics," *Proceedings of the Royal Society of London. Series A, Containing Papers of a Mathematical and Physical Character*, vol. 145, no. 855, pp. 523–529, 1934.

[25] M. C. Thompson, H. Badakov, A. M. Cook, J. B. Rosenzweig, R. Tikhoplav, G. Travish, I. Blumenfeld, M. J. Hogan, R. Ischebeck, N. Kirby, R. Siemann, D. Walz, P. Muggli, A. Scott, and R. B. Yoder, "Breakdown Limits on Gigavolt-per-Meter Electron-Beam-Driven Wakefields in Dielectric Structures," *Phys. Rev. Lett.*, vol. 100, no. 21, p. 214801, May 2008. [Online]. Available: https://link.aps.org/doi/10.1103/PhysRevLett.100.214801

[26] B. D. O'Shea, "Gigavolt-per-Meter Wakefields in Annular Dielectric Structures," Ph.D. dissertation, UCLA, 2014. [Online]. Available: https://escholarship.org/uc/item/6th460cr

[27] J. Rosenzweig, G. Andonian, P. Bucksbaum, M. Ferrario, S. Full, A. Fukusawa, E. Hemsing, B. Hidding, M. Hogan, P. Krejcik, P. Muggli, G. Marcus, A. Marinelli, P. Musumeci, B. O'Shea, C. Pellegrini, D. Schiller, and G. Travish, "Teravolt-per-meter beam and plasma fields from low-charge femtosecond electron beams," *Nuclear Instruments and Methods in Physics Research Section A: Accelerators, Spectrometers, Detectors and Associated Equipment*, p. S0168900211001513, Feb. 2011. [Online]. Available: https://linkinghub.elsevier.com/retrieve/pii/S0168900211001513

[28] I. Blumenfeld, C. E. Clayton, F.-J. Decker, M. J. Hogan, C. Huang, R. Ischebeck, R. Iverson, C. Joshi, T. Katsouleas, N. Kirby, W. Lu, K. A. Marsh, W. B. Mori, P. Muggli, E. Oz, R. H. Siemann, D. Walz, and M. Zhou, "Energy doubling of 42 GeV electrons in a metre-scale plasma wakefield accelerator," *Nature*, vol. 445, no. 7129, pp. 741–744, Feb. 2007. [Online]. Available: https://www.nature.com/articles/nature05538

[29] P. San Miguel Claveria, E. Adli, L. Amorim, W. An, C. Clayton, S. Corde, S. Gessner, M. Hogan, C. Joshi, O. Kononenko, and others, "Betatron radiation and emittance growth in plasma wakefield accelerators," *Philosophical Transactions of the Royal Society A*, vol. 377, no. 2151, p. 20180173, 2019.

[30] M. Litos, E. Adli, W. An, C. I. Clarke, C. E. Clayton, S. Corde, J. P. Delahaye, R. J. England, A. S. Fisher, J. Frederico, S. Gessner, S. Z. Green, M. J. Hogan, C. Joshi, W. Lu, K. A. Marsh, W. B. Mori, P. Muggli, N. Vafaei-Najafabadi, D. Walz, G. White, Z. Wu, V. Yakimenko, and G. Yocky, "High-efficiency acceleration of an electron beam in a plasma wakefield accelerator," *Nature*, vol. 515, no. 7525, pp. 92–95, Nov. 2014. [Online]. Available: https://www.nature.com/articles/nature13882

[31] A. Seryi, M. Hogan, S. Pei, T. Raubenheimer, P. Tenenbaum, T. Katsouleas, U. Duke, C. Huang, C. Joshi, W. Mori, and others, "A concept of plasma wake field acceleration linear collider (PWFA-LC)," Stanford Linear Accelerator Center (SLAC), Tech. Rep., 2009.

[32] K. L. F. Bane, P. Chen, and P. B. Wilson, "On Collinear Wake Field Acceleration," *IEEE Transactions on Nuclear Science*, vol. 32, no. 5, pp. 3524–3526, Oct. 1985.

[33] R. J. England, J. B. Rosenzweig, and G. Travish, "Generation and Measurement of Relativistic Electron Bunches Characterized by a Linearly Ramped Current Profile," *Phys. Rev. Lett.*, vol. 100, no. 21, p. 214802, May 2008. [Online]. Available: https://link.aps.org/doi/10.1103/PhysRevLett.100.214802

[34] G. Andonian, S. Barber, F. H. OShea, M. Fedurin, K. Kusche, C. Swinson, and J. B. Rosenzweig, "Generation of Ramped Current Profiles in Relativistic Electron Beams Using Wakefields in Dielectric Structures," *Phys. Rev. Lett.*, vol. 118, no. 5, p. 054802, Feb. 2017. [Online]. Available: https://link.aps.org/doi/10.1103/PhysRevLett.118.054802

[35] G. Loisch, J. Good, M. Gross, H. Huck, I. Isaev, M. Krasilnikov, O. Lishilin, A. Oppelt, Y. Renier, F. Stephan, R. Brinkmann, F. Grner, and I. Will, "Photocathode laser based bunch shaping for high transformer ratio plasma wakefield acceleration," *Nuclear Instruments and Methods in Physics Research Section A: Accelerators, Spectrometers, Detectors and Associated Equipment*, vol. 909, pp. 107–110, Nov. 2018. [Online]. Available: http://www.sciencedirect.com/science/article/pii/S0168900218301979

[36] C. E. Nielsen and A. Sessler, "Longitudinal space charge effects in particle accelerators," *Review of Scientific Instruments*, vol. 30, no. 2, pp. 80–89, 1959.

[37] P. Piot, Y.-E. Sun, J. G. Power, and M. Rihaoui, "Generation of relativistic electron bunches with arbitrary current distribution via transverse-to-longitudinal phase space exchange," *Phys. Rev. ST Accel. Beams*, vol. 14, no. 2, p. 022801, Feb. 2011. [Online]. Available: https://link.aps.org/doi/10.1103/PhysRevSTAB.14.022801

[38] Q. Gao, J. Shi, H. Chen, G. Ha, J. G. Power, M. Conde, and W. Gai, "Single-shot wakefield measurement system," *Phys. Rev. Accel. Beams*, vol. 21, no. 6, p. 062801, Jun. 2018. [Online]. Available: https://link.aps.org/doi/10.1103/PhysRevAccelBeams.21.062801

[39] J. B. Rosenzweig, D. B. Cline, B. Cole, H. Figueroa, W. Gai, R. Konecny, J. Norem, P. Schoessow, and J. Simpson, "Experimental Observation of Plasma Wake-Field Acceleration," *Phys. Rev. Lett.*, vol. 61, no. 1, pp. 98–101, Jul. 1988. [Online]. Available: https://link.aps.org/doi/10.1103/PhysRevLett.61.98

[40] Q. Gao, G. Ha, C. Jing, S. Antipov, J. Power, M. Conde, W. Gai, H. Chen, J. Shi, E. Wisniewski, D. Doran, W. Liu, C. Whiteford, A. Zholents, P. Piot, and S. Baturin, "Observation of High Transformer Ratio of Shaped Bunch Generated by an Emittance-Exchange Beam Line," *Phys. Rev. Lett.*, vol. 120, no. 11, p. 114801, Mar. 2018. [Online]. Available: https://link.aps.org/doi/10.1103/PhysRevLett.120.114801

[41] G. Loisch, G. Asova, P. Boonpornprasert, R. Brinkmann, Y. Chen, J. Engel, J. Good, M. Gross, F. Grner, H. Huck, D. Kalantaryan, M. Krasilnikov, O. Lishilin, A. M. de la Ossa, T. J. Mehrling, D. Melkumyan, A. Oppelt, J. Osterhoff, H. Qian, Y. Renier, F. Stephan, C. Tenholt, V. Wohlfarth, and Q. Zhao, "Observation of High Transformer Ratio Plasma Wakefield Acceleration," *Phys. Rev. Lett.*, vol. 121, no. 6, p. 064801, Aug. 2018. [Online]. Available: https://link.aps.org/doi/10.1103/PhysRevLett.121.064801

[42] M. Conde, E. Wisniewski, W. Liu, Z. Yusof, S. Antipov, C. Jing, W. Gai, R. Konecny, D. Doran, and J. Power, "The Upgraded Argonne Wakefield Accelerator Facility (AWA): a Test-Bed for the Development of High Gradient Accelerating Structures and Wakefield Measurements," 2013.

[43] A. Halavanau, G. Qiang, G. Ha, E. Wisniewski, P. Piot, J. Power, and W. Gai, "Spatial control of photoemitted electron beams using a microlens-array transverse-shaping technique," *Phys. Rev. Accel. Beams*, vol. 20, no. 10, p. 103404, Oct. 2017. [Online]. Available: https://link.aps.org/doi/10.1103/PhysRevAccelBeams.20.103404

[44] G. Caryotakis, "High power klystrons: Theory and practice at the stanford linear accelerator center."

[45] S. Baturin and A. Zholents, "Upper limit for the accelerating gradient in the collinear wakefield accelerator as a function of the transformer ratio," *Phys. Rev. Accel. Beams*, vol. 20, no. 6, p. 061302, Jun. 2017. [Online]. Available: https://link.aps.org/doi/10.1103/PhysRevAccelBeams.20.061302

[46] T. Katsouleas, "Physical mechanisms in the plasma wake-field accelerator," *Phys. Rev. A*, vol. 33, no. 3, pp. 2056–2064, Mar. 1986. [Online]. Available: https://link.aps.org/doi/10.1103/PhysRevA.33.2056

[47] F. Lemery and P. Piot, "Tailored electron bunches with smooth current profiles for enhanced transformer ratios in beam-driven acceleration," *Physical Review Special Topics - Accelerators and Beams*, vol. 18, no. 8, p. 081301, Aug. 2015. [Online]. Available: https://link.aps.org/doi/10.1103/PhysRevSTAB.18.081301

[48] R. Roussel, G. Andonian, M. Conde, D. Doran, G. Ha, W. Lynn, J. Power, J. Rosenzweig, J. Seok, C. Whiteford, and E. Wisniewski, "Transformer Ratio Measurements from Ramped Beams in the Plasma Blowout Regime using Emittance Exchange." JACOW Publishing, Geneva, Switzerland, Jun. 2019, pp. 3778–3781. [Online]. Available: http://accelconf.web.cern.ch/AccelConf/ipac2019/doi/JACoW-IPAC2019-THPGW088.html

[49] R. Ruth, A. W. Chao, R. L. Morton, and P. B. Wilson, "A Plasma Wake Field Accelerator," *Part. Accel.*, vol. 17, p. 171, 1985.

[50] J. D. Jackson, *Classical electrodynamics*. AAPT, 1999.

[51] J. B. Rosenzweig, B. Breizman, T. Katsouleas, and J. J. Su, "Acceleration and focusing of electrons in two-dimensional nonlinear plasma wake fields," *Physical Review A*, vol. 44, no. 10, pp. R6189–R6192, Nov. 1991. [Online]. Available: https://link.aps.org/doi/10.1103/PhysRevA.44.R6189

[52] J. M. Dawson, "Nonlinear Electron Oscillations in a Cold Plasma," *Phys. Rev.*, vol. 113, no. 2, pp. 383–387, Jan. 1959. [Online]. Available: https://link.aps.org/doi/10.1103/PhysRev.113.383

[53] A. I. Akhiezer and R. Polovin, "Theory of wave motion of an electron plasma," *Soviet Phys. JETP*, vol. 3, 1956.

[54] J. Rosenzweig, "Nonlinear Plasma Dynanics in the Plasma Wakefield Accelerator," *IEEE Transactions on Plasma Science*, vol. 15, no. 2, pp. 186–191, Apr. 1987.

[55] W. Lu, C. Huang, M. Zhou, W. B. Mori, and T. Katsouleas, "Nonlinear Theory for Relativistic Plasma Wakefields in the Blowout Regime," *Phys. Rev. Lett.*, vol. 96, no. 16, p. 165002, Apr. 2006. [Online]. Available: https://link.aps.org/doi/10.1103/PhysRevLett.96.165002

[56] P. Mora and T. M. Antonsen, Jr, "Kinetic modeling of intense, short laser pulses propagating in tenuous plasmas," *Physics of Plasmas*, vol. 4, no. 1, pp. 217–229, 1997.

[57] W. Lu, C. Huang, M. M. Zhou, W. B. Mori, and T. Katsouleas, "Limits of linear plasma wakefield theory for electron or positron beams," *Physics of Plasmas*, vol. 12, no. 6, p. 063101, May 2005. [Online]. Available: https://aip.scitation.org/doi/abs/10.1063/1.1905587

[58] W. Lu, W. An, C. Huang, C. Joshi, W. Mori, M. Hogan, T. Raubenheimer, A. Seryi, and M. Park, "High Transformer Ratio PWFA for Application on XFELs," p. 3.

[59] H. Weideman, *Particle Accelerator Physics-I: Basic Principles and Linear Beam Dynamics*. Springer-Verlag, New York, 1999.

[60] N. Barov, M. E. Conde, W. Gai, and J. B. Rosenzweig, "Propagation of Short Electron Pulses in a Plasma Channel," *Phys. Rev. Lett.*, vol. 80, no. 1, pp. 81–84, Jan. 1998. [Online]. Available: https://link.aps.org/doi/10.1103/PhysRevLett.80.81

[61] N. Barov and J. B. Rosenzweig, "Propagation of short electron pulses in underdense plasmas," *Phys. Rev. E*, vol. 49, no. 5, pp. 4407–4416, May 1994. [Online]. Available: https://link.aps.org/doi/10.1103/PhysRevE.49.4407

[62] X. Xu, J. Hua, Y. Wu, C. Zhang, F. Li, Y. Wan, C.-H. Pai, W. Lu, W. An, P. Yu, M. Hogan, C. Joshi, and W. Mori, "Physics of Phase Space Matching for Staging Plasma and Traditional Accelerator Components Using Longitudinally Tailored Plasma Profiles," *Phys. Rev. Lett.*, vol. 116, no. 12, p. 124801, Mar. 2016. [Online]. Available: https://link.aps.org/doi/10.1103/PhysRevLett.116.124801

[63] K. A. Marsh, C. E. Clayton, D. K. Johnson, C. Huang, C. Joshi, W. Lu, W. B. Mori, M. Zhou, C. D. Barnes, F. Decker, M. J. Hogan, R. Iverson, P. Krejcik, C. L. O'Connell, R. Siemann, D. Walz, S. Deng, T. C. Katsouleas, P. Muggli, and E. Oz, "Beam Matching to a Plasma Wake Field Accelerator using a Ramped Density Profile at the Plasma Boundary," in *Proceedings of the 2005 Particle Accelerator Conference*, May 2005, pp. 2702–2704.

[64] J. Krall, K. Nguyen, and G. Joyce, "Numerical simulations of axisymmetric erosion processes in ionfocused regimetransported beams," *Physics of Fluids B: Plasma Physics*, vol. 1, no. 10, pp. 2099–2105, Oct. 1989. [Online]. Available: https://aip.scitation.org/doi/abs/10.1063/1.859074

[65] C. Huang, W. Lu, M. Zhou, C. E. Clayton, C. Joshi, W. B. Mori, P. Muggli, S. Deng, E. Oz, T. Katsouleas, M. J. Hogan, I. Blumenfeld, F. J. Decker, R. Ischebeck, R. H. Iverson, N. A. Kirby, and D. Walz, "Hosing Instability in the Blow-Out Regime for Plasma-Wakefield Acceleration," *Phys. Rev. Lett.*, vol. 99, no. 25, p. 255001, Dec. 2007. [Online]. Available: https://link.aps.org/doi/10.1103/PhysRevLett.99.255001

[66] D. P. Grote, A. Friedman, J. Vay, and I. Haber, "The WARP Code: Modeling High Intensity Ion Beams," *AIP Conference Proceedings*, vol. 749, no. 1, pp. 55–58, Mar. 2005. [Online]. Available: https://aip.scitation.org/doi/abs/10.1063/1.1893366

[67] P. Piot, "Overview of Alternative Bunching and Current-shaping Techniques for Low-Energy Electron Beams," *Proceedings of the 37th International Free Electron Laser Conference*, vol. FEL2015, pp. 6 pages, 1.271 MB, 2015. [Online]. Available: http://accelconf.web.cern.ch/AccelConf/DOI/FEL2015/JACoW-FEL2015-MOD02.html

[68] P. Emma, Z. Huang, K.-J. Kim, and P. Piot, "Transverse-to-longitudinal emittance exchange to improve performance of high-gain free-electron lasers," *Phys. Rev. ST Accel. Beams*, vol. 9, no. 10, p. 100702, Oct. 2006. [Online]. Available: https://link.aps.org/doi/10.1103/PhysRevSTAB.9.100702

[69] K. Floettmann and V. V. Paramonov, "Beam dynamics in transverse deflecting rf structures," *Phys. Rev. ST Accel. Beams*, vol. 17, no. 2, p. 024001, Feb. 2014. [Online]. Available: https://link.aps.org/doi/10.1103/PhysRevSTAB.17.024001

[70] G. Ha, M. Cho, W. Gai, K.-J. Kim, W. Namkung, and J. Power, "Perturbation-minimized triangular bunch for high-transformer ratio using a double dogleg emittance exchange beam line," *Phys. Rev. Accel. Beams*, vol. 19, no. 12, p. 121301, Dec. 2016. [Online]. Available: https://link.aps.org/doi/10.1103/PhysRevAccelBeams.19.121301

[71] G. Ha, M. Conde, W. Gai, D. Doran, and J. Power, "Preparations for installation of the double emittance-exchange beamline at the Argonne Wakefield Accelerator facility," 2018.

[72] G. Ha, M. Cho, W. Namkung, J. Power, D. Doran, E. Wisniewski, M. Conde, W. Gai, W. Liu, C. Whiteford, Q. Gao, K.-J. Kim, A. Zholents, Y.-E. Sun, C. Jing, and P. Piot, "Precision Control of the Electron Longitudinal Bunch Shape Using an Emittance-Exchange Beam Line," *Phys. Rev. Lett.*, vol. 118, no. 10, p. 104801, Mar. 2017. [Online]. Available: https://link.aps.org/doi/10.1103/PhysRevLett.118.104801

[73] M. Reiser and P. O'Shea, *Theory and design of charged particle beams*. Wiley Online Library, 1994, vol. 312.

[74] H. H. Braun, R. Corsini, L. Groening, F. Zhou, A. Kabel, T. O. Raubenheimer, R. Li, and T. Limberg, "Emittance growth and energy loss due to coherent synchrotron radiation in a bunch compressor," *Phys. Rev. ST Accel. Beams*, vol. 3, no. 12, p. 124402, Dec. 2000. [Online]. Available: https://link.aps.org/doi/10.1103/PhysRevSTAB.3.124402

[75] A. Adelmann, C. Kraus, Y. Ineichen, S. Russell, Y. Bi, and J. Yang, "The object oriented parallel accelerator library (OPAL), design, implementation and application," in *Proceedings of the 2009 Particle Accelerator Conference*, 2009.

[76] S. Z. Green, E. Adli, C. I. Clarke, S. Corde, S. A. Edstrom, A. S. Fisher, J. Frederico, J. C. Frisch, S. Gessner, S. Gilevich, P. Hering, M. J. Hogan, R. K. Jobe, M. Litos, J. E. May, D. R. Walz, V. Yakimenko, C. E. Clayton, C. Joshi, K. A. Marsh, N. Vafaei-Najafabadi, and P. Muggli, "Laser ionized preformed plasma at FACET," *Plasma Phys. Control. Fusion*, vol. 56, no. 8, p. 084011, Jul. 2014. [Online]. Available: https://doi.org/10.1088%2F0741-3335%2F56%2F8%2F084011

[77] I. Blumenfeld, F. Decker, M. Hogan, R. Ischebeck, R. Iverson, N. Kirby, R. Siemann, and D. Walz, "BEAM HEAD EROSION IN SELF-IONIZED PLASMA WAKEFIELD ACCELERATORS."

[78] S. Gessner, E. Adli, J. M. Allen, W. An, C. I. Clarke, C. E. Clayton, S. Corde, J. P. Delahaye, J. Frederico, S. Z. Green, C. Hast, M. J. Hogan, C. Joshi, C. A. Lindstrm, N. Lipkowitz, M. Litos, W. Lu, K. A. Marsh, W. B. Mori, B. OShea, N. Vafaei-Najafabadi, D. Walz, V. Yakimenko, and G. Yocky, "Demonstration of a positron beam-driven hollow channel plasma wakefield accelerator," *Nat Commun*, vol. 7, no. 1, pp. 1–6, Jun. 2016. [Online]. Available: https://www.nature.com/articles/ncomms11785

[79] B. Hidding, A. Beaton, A. F. Habib, T. Heinemann, G. G. Manahan, P. Scherkl, A. Sutherland, and D. Ullmann, "First Measurements of Trojan Horse Injection in a Plasma Wakefield Accelerator," p. 6, 2017.

[80] F. Paschen, "Ueber die zum Funkenbergang in Luft, Wasserstoff und Kohlensure bei verschiedenen Drucken erforderliche Potentialdifferenz," *Annalen der Physik*, vol. 273, no. 5, pp. 69–96, 1889. [Online]. Available: https://onlinelibrary.wiley.com/doi/abs/10.1002/andp.18892730505

[81] O. W. Richardson, *Thermionic Emission from Hot Bodies*. Watchmaker Publishing, Mar. 2003, google-Books-ID: PrbOIoMnxnwC.

[82] J. A. Bittencourt, *Fundamentals of plasma physics*. Springer Science & Business Media, 2013.

[83] A. Piel, *Plasma physics: an introduction to laboratory, space, and fusion plasmas*. Springer, 2017.

[84] P. C. Stangeby, "The BohmChodura plasma sheath criterion," *Physics of Plasmas*, vol. 2, no. 3, pp. 702–706, Mar. 1995. [Online]. Available: https://aip.scitation.org/doi/abs/10.1063/1.871483

[85] V. H. Chaplin and P. M. Bellan, "Emission and afterglow properties of an expanding RF plasma with nonuniform neutral gas density," *Physics of Plasmas*, vol. 23, no. 8, p. 083506, Aug. 2016. [Online]. Available: https://aip.scitation.org/doi/10.1063/1.4960326

[86] M. Borland, *elegant: A Flexible SDDS-Compliant Code for Accelerator Simulation*, 2000.

[87] G. R. Lynch and O. I. Dahl, "Approximations to multiple Coulomb scattering," *Nuclear Instruments and Methods in Physics Research Section B: Beam Interactions with Materials and Atoms*, vol. 58, no. 1, pp. 6–10, May 1991. [Online]. Available: http://www.sciencedirect.com/science/article/pii/0168583X9195671Y

[88] M. B. Reid, "Electron beam emittance growth in thin foils: A betatron function analysis," *Journal of Applied Physics*, vol. 70, no. 11, pp. 7185–7187, Dec. 1991. [Online]. Available: https://aip.scitation.org/doi/abs/10.1063/1.349761

[89] L. Wartski, S. Roland, J. Lasalle, M. Bolore, and G. Filippi, "Interference phenomenon in optical transition radiation and its application to particle beam diagnostics and multiplescattering measurements," *Journal of Applied Physics*, vol. 46, no. 8, pp. 3644–3653, Aug. 1975. [Online]. Available: http://aip.scitation.org/doi/10.1063/1.322092

[90] J. B. Rosenzweig, N. Barov, M. C. Thompson, and R. B. Yoder, "Energy loss of a high charge bunched electron beam in plasma: Simulations, scaling, and accelerating wakefields," *Phys. Rev. ST Accel. Beams*, vol. 7, no. 6, p. 061302, Jun. 2004. [Online]. Available: https://link.aps.org/doi/10.1103/PhysRevSTAB.7.061302

[91] M. J. Hogan, T. O. Raubenheimer, A. Seryi, P. Muggli, T. Katsouleas, C. Huang, W. Lu, W. An, K. A. Marsh, W. B. Mori, C. E. Clayton, and C. Joshi, "Plasma wakefield acceleration experiments at FACET," *New J. Phys.*, vol. 12, no. 5, p. 055030, May 2010. [Online]. Available: https://doi.org/10.1088%2F1367-2630%2F12%2F5%2F055030

[92] H. Griem, *Spectral line broadening by plasmas*. Elsevier, 2012.

[93] M. Tzoufras, W. Lu, F. S. Tsung, C. Huang, W. B. Mori, T. Katsouleas, J. Vieira, R. A. Fonseca, and L. O. Silva, "Beam Loading in the Nonlinear Regime of Plasma-Based Acceleration," *Phys. Rev. Lett.*, vol. 101, no. 14, p. 145002, Sep. 2008. [Online]. Available: https://link.aps.org/doi/10.1103/PhysRevLett.101.145002

[94] T. Xu, C. Jing, A. Kanareykin, P. Piot, and J. Power, "Spatio-Temporal Shaping of the Photocathode Laser Pulse for Low-Emittance Shaped Electron Bunches," in *10th Int. Partile Accelerator Conf.(IPAC'19), Melbourne, Australia, 19-24 May 2019*. JACOW Publishing, Geneva, Switzerland, 2019, pp. 2163–2166.

[95] T. Xu, M. Conde, G. Ha, M. Kuriki, P. Piot, J. Power, and E. Wisniewski, "Generation High-Charge of Flat Beams at the Argonne Wakefield Accelerator," Fermi National Accelerator Lab.(FNAL), Batavia, IL (United States), Tech. Rep., 2019.

[96] W. Leemans, A. Gonsalves, H.-S. Mao, K. Nakamura, C. Benedetti, C. Schroeder, C. Tth, J. Daniels, D. Mittelberger, S. Bulanov, and others, "Multi-GeV electron beams from capillary-discharge-guided subpetawatt laser pulses in the self-trapping regime," *Physical review letters*, vol. 113, no. 24, p. 245002, 2014.

[97] J. Rosenzweig, F. Filippi, A. Zigler, M. Anania, G. Andonian, A. Biagioni, E. Chiadroni, A. Cianchi, A. Deng, M. Ferrario, and others, "Adiabatic plasma lens experiments at SPARC," *Nuclear Instruments and Methods in Physics Research Section A: Accelerators, Spectrometers, Detectors and Associated Equipment*, vol. 909, pp. 471–475, 2018.